


<b>Title</b>	Computational study of the growth of copper thin films by atomic layer deposition
<b>Author(s)</b>	Maimaiti, Yasheng
<b>Publication date</b>	2015
<b>Original citation</b>	Maimaiti, Y. 2015. Computational study of the growth of copper thin films by atomic layer deposition. PhD Thesis, University College Cork.
<b>Type of publication</b>	Doctoral thesis
<b>Rights</b>	© 2015, Yasheng Maimaiti. <a href="http://creativecommons.org/licenses/by-nc-nd/3.0/">http://creativecommons.org/licenses/by-nc-nd/3.0/</a> 
<b>Item downloaded from</b>	<a href="http://hdl.handle.net/10468/2122">http://hdl.handle.net/10468/2122</a>

Downloaded on 2017-02-12T08:17:46Z

# COMPUTATIONAL STUDY OF THE GROWTH OF COPPER THIN FILMS BY ATOMIC LAYER DEPOSITION



by

**Yasheng Maimaiti**

**April, 2015**

**Supervisor: Dr. Simon Elliott**

**Head of Department: Prof. John McInerney**

**A thesis presented to The National University of Ireland, Cork  
For the degree of 'Doctor of Philosophy' (Ph.D.) In Physics**



**Tyndall National Institute, University College Cork, Cork, Ireland**

*To My Dear Parents!*

# DECLARATION

I hereby declare that this dissertation is entirely my own work and that it has not been previously submitted, in part or whole, to any other university for the award of any degree or any qualification.

Signed: \_\_\_\_\_

Date: \_\_\_\_\_

# ACKNOWLEDGEMENTS

My first and foremost thanks go to my supervisor, Dr. Simon Elliott, for his support, understanding, and guidance during my PhD study. Through numerous inspiring discussions with him, I learned the knowledge and skills to complete this work. I am thankful for giving me insightful feedbacks and for his corrections of my papers and this thesis with great patience. In addition, I am grateful for my co-supervisor Professor Stephen Fahy and my advisor Professor Eoin O'Reilly for their timely evaluation of my progress and guide me to proceed in the right track. I am indebted to Dr. Michael Nolan for his help on performing calculations with VASP.

I wish to thank 'ALDesign' project members Gangotri Dey and Dr. Ciaran Murray for their helpful discussions. I also thank people in postgrad rooms: Gangotri, Merid, Sylwia, Mahdi, Lin Jun, Thomas, Glen, Katya, Anna, Sara and Hadi for their friendship. I would like to thank industrial partners Scott B. Clendenning, Harsono Simka and Roger Nagle from Intel Corporation and James Connolly from Applied Materials for collaboration and fruitful discussions. I would like to extend my thanks to supercomputer support teams in Tyndall and ICHEC.

This work is supported by the Science Foundation Ireland (SFI) through the project 'ALDesign'.

My wife, Hayrensa, deserves very special thanks for her patience and continuous support during the completion of this work.

# ABSTRACT

Copper is the main interconnect material in microelectronic devices, and a 2 nm-thick continuous Cu film seed layer needs to be deposited to produce microelectronic devices with the smallest features and more functionality. Atomic layer deposition (ALD) is the most suitable method to deposit such thin films. However, the reaction mechanism and the surface chemistry of copper ALD remain unclear, which is deterring the development of better precursors and design of new ALD processes. In this thesis, we study the surface chemistries during ALD of copper by means of density functional theory (DFT).

To understand the effect of temperature and pressure on the composition of copper with substrates, we used ab initio atomistic thermodynamics to obtain phase diagram of the Cu(111)/SiO<sub>2</sub>(0001) interface. We found that the interfacial oxide Cu<sub>2</sub>O phases prefer high oxygen pressure and low temperature while the silicide phases are stable at low oxygen pressure and high temperature for Cu/SiO<sub>2</sub> interface, which is in good agreement with experimental observations.

Understanding the precursor adsorption on surfaces is important for understanding the surface chemistry and reaction mechanism of the Cu ALD process. Focusing on two common Cu ALD precursors, Cu(dmap)<sub>2</sub> and Cu(acac)<sub>2</sub>, we studied the precursor adsorption on Cu surfaces by means of van der Waals (vdW) inclusive DFT methods. We found that the adsorption energies and adsorption geometries are dependent on the adsorption sites and on the method used to include vdW in the DFT calculation. Both precursor molecules are partially decomposed and the Cu cations are partially reduced in their chemisorbed structure. It is found that clean cleavage of the ligand–metal bond is one of the requirements for selecting precursors for ALD of metals. Bonding

between surface and an atom in the ligand which is not coordinated with the Cu may result in impurities in the thin film.

To have insight into the reaction mechanism of a full ALD cycle of Cu ALD, we proposed reaction pathways based on activation energies and reaction energies for a range of surface reactions between  $\text{Cu}(\text{dmap})_2$  and  $\text{Et}_2\text{Zn}$ . The butane formation and desorption steps are found to be extremely exothermic, explaining the ALD reaction scheme of original experimental work. Endothermic ligand diffusion and re-ordering steps may result in residual dmap ligands blocking surface sites at the end of the  $\text{Et}_2\text{Zn}$  pulse, and in residual Zn being reduced and incorporated as an impurity. This may lead to very slow growth rate, as was the case in the experimental work.

By investigating the reduction of CuO to metallic Cu, we elucidated the role of the reducing agent in indirect ALD of Cu. We found that CuO bulk is protected from reduction during vacuum annealing by the CuO surface and that  $\text{H}_2$  is required in order to reduce that surface, which shows that the strength of reducing agent is important to obtain fully reduced metal thin films during indirect ALD processes.

Overall, in this thesis, we studied the surface chemistries and reaction mechanisms of Cu ALD processes and the nucleation of Cu to form a thin film.

# CONTENTS

<b>1</b>	<b>Introduction and Overview .....</b>	<b>1</b>
1.1	<i>Atomic layer deposition (ALD) .....</i>	<i>1</i>
1.2	<i>ALD of Copper .....</i>	<i>3</i>
1.3	<i>Challenges of Cu ALD .....</i>	<i>7</i>
1.4	<i>Thesis overview and scope .....</i>	<i>10</i>
<b>2</b>	<b>Theoretical Background .....</b>	<b>12</b>
2.1	<i>Density Functional theory.....</i>	<i>12</i>
2.1.1	<i>The Many-Body Problem.....</i>	<i>12</i>
2.1.2	<i>The Hohenberg-Kohn theorems.....</i>	<i>13</i>
2.1.3	<i>The Kohn-Sham equation .....</i>	<i>14</i>
2.2	<i>Approximation of exchange-correlation energy .....</i>	<i>16</i>
2.3	<i>Van der Waals (vdW) force .....</i>	<i>17</i>
2.4	<i>Bader Charge.....</i>	<i>19</i>
2.5	<i>Ab initio Atomistic Thermodynamics .....</i>	<i>20</i>
<b>3</b>	<b>Interface Composition of Cu/SiO<sub>2</sub> Interface.....</b>	<b>22</b>
3.1	<i>Introduction.....</i>	<i>22</i>
3.2	<i>Computational methods .....</i>	<i>23</i>
3.3	<i>Results and discussion .....</i>	<i>26</i>
3.4	<i>Conclusion .....</i>	<i>29</i>
<b>4</b>	<b>Precursor Adsorption on Copper Surfaces.....</b>	<b>30</b>
4.1	<i>Introduction.....</i>	<i>30</i>
4.2	<i>Cu(dmap)<sub>2</sub> adsorption on Cu surface. ....</i>	<i>32</i>
4.2.1	<i>Theoretical Method .....</i>	<i>33</i>
4.2.2	<i>Results .....</i>	<i>38</i>
4.2.3	<i>Discussion .....</i>	<i>52</i>



4.3	<i>Cu(acac)<sub>2</sub> adsorption on Cu(111) surface</i>	57
4.4	<i>Conclusions</i>	63
<b>5</b>	<b>Surface Chemistry of Cu ALD by Transmetallation</b>	<b>65</b>
5.1	<i>Computational Method</i>	66
5.2	<i>Results</i>	67
5.2.1	First half reaction: adsorption and decomposition of Cu(dmap) <sub>2</sub> on Cu(111) surface.	67
5.2.2	Second half reaction: Et <sub>2</sub> Zn adsorption, butane formation and Zn(dmap) <sub>2</sub> formation.	72
5.3	<i>Discussion</i>	81
5.3.1	The reaction mechanism of Cu ALD	81
5.4	<i>Conclusion</i>	83
<b>6</b>	<b>The Reduction Of CuO To Metallic Copper</b>	<b>85</b>
6.1	<i>Introduction</i>	85
6.2	<i>Computational Methods</i>	87
6.2.1	CuO surface.	91
6.2.2	Oxygen vacancies on CuO(111) surface.	94
6.2.3	H <sub>2</sub> adsorption on CuO(111) surfaces	107
6.2.4	Ab initio atomistic thermodynamics of H <sub>2</sub> adsorption on CuO(111) surface	111
6.3	<i>Conclusion</i>	114
<b>7</b>	<b>Conclusions</b>	<b>116</b>
7.1	<i>Summary</i>	116
7.2	<i>Future work and outlook</i>	119
	<b>Bibliography</b>	<b>120</b>

# 1 Introduction and Overview

## 1.1 Atomic layer deposition (ALD)

Atomic layer deposition (ALD, previously called Atomic Layer Epitaxy) is a modified version of chemical vapour deposition (CVD) technique to grow ultrathin continuous and uniform thin films through alternate self-limiting surface reactions.[1] ALD has attracted wide interest in recent years as a powerful thin film deposition method for various applications in many fields, most notably in microelectronics. No other thin film technique can approach the conformality achieved by ALD on high aspect structures.[2] Unlike CVD, ALD relies on sequential and saturating surface reactions of the alternately applied precursors. The precursor pulses are separated by inert gas purging or evacuation of the reaction chamber to avoid gas-phase reactions between the precursors.[1]

As ALD is most common only used to deposit metal oxides, we illustrate the process using a simple metal oxide deposition cycle. The basic principle of ALD is schematically illustrated in Figure 1.1, where one ALD cycle of a metal oxide (M=metal, O=oxygen) deposition process is presented. In the first step, the substrate surface is exposed to a “precursor” of gaseous  $ML_n$  (L represents a ligand) which chemisorbed onto the OH covered surface, leaves the surface saturated with a monolayer of the precursor fragments. The proton transfer from the surface to the chemisorbed  $ML_n$  yields intermediate OML at the surface and by-product HL. After purging the HL by-product with inert gas, a “co-reagent” (in this example,  $H_2O$ ) is introduced for further transformation of OML into the  $-O-M-$  bonds. The  $H_2O$

## 1. Introduction and Overview

---

molecules react with the OML at the surface and produce a second by product, HL, leaving the MO layer covered with OH groups. After inert gas purging the next ALD cycle continues. Because there are only a finite number of surface sites, the surface reactions self-limit at a finite coverage of surface species. If each of the two surface reactions is self-limiting, then the two reactions may proceed in a sequential fashion to deposit a thin film with atomic level control.[2]

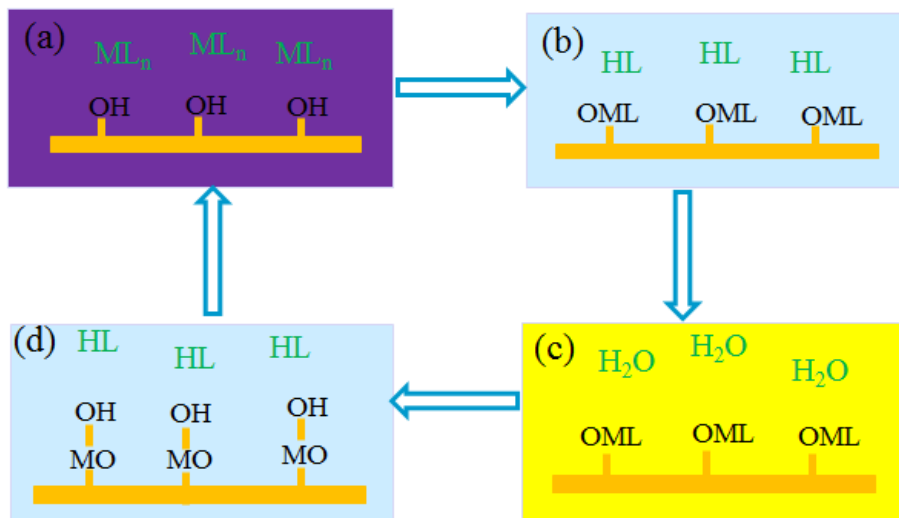


Figure 1.1. Schematic illustration of a metal oxide (MO) ALD cycle where precursors (ML<sub>n</sub> and H<sub>2</sub>O) are alternately pulsed and separated by inert gas purging.

It is the self-limiting nature of ALD reactions that give rise to a uniform and conformal growth behaviour and control over thickness and composition of the film.[3] Therefore, the alternate exposure of the precursors alone does not qualify the process as ALD. A successful ALD process relies on suitable chemical precursors being used under reaction conditions that are appropriate for them. The requirements for ALD precursors include sufficient volatility, thermal stability, and self-limited reactivity with substrates and with the films being deposited. The precursor vapour should not etch or corrode the substrate or deposited film.[4]

## 1. Introduction and Overview

---

Thanks to its superior capabilities, ALD has become an important tool in nano-, energy, bio- and environmental technologies and has bright future applications in other newly emerging fields.[5] The various materials deposited with ALD include oxides, nitrides, sulfides and metals.[6] However, many challenges have also emerged as ALD becomes increasingly popular. One such challenge is ALD of metals, and more specifically ALD of copper.

### 1.2 ALD of copper

The interest in depositing uniform and island-free ultrathin films of copper originated from its application as the interconnect material in microelectronic devices. Copper has superior properties such as lower resistivity and higher current density for electromigration than aluminium and these are critical for improved device performance and reliability. Figure 1.2 shows a typical cross-section of Hierarchical Scaling for a microprocessor unit (MPU) from the International Technology Roadmap for Semiconductors (ITRS).[7] We can see from the cross-section that the MPU utilizes a high number of metal layers (orange colours) with a hierarchical wiring approach of steadily increasing pitch and thickness at each conductor level. These complex copper interconnects are currently fabricated using the electrodeposition technique and CVD. Important processing steps prior to electroplating involve the deposition of a thin copper layer in order to provide a conductive substrate for electroplating and to prevent copper diffusion into dielectric substrates. Ideally, the thickness of this seed layer should be less than 2 nm and should be uniform and continuous in order to meet the future demands of current trends in integrated circuit technology.

## 1. Introduction and Overview

---

Deposition techniques including physical vapour deposition (PVD),[8] electrodeposition,[9] and CVD[10] have been applied with the aim of obtaining such a thin film of Cu. However, voids are formed when these techniques are used to fill the high aspect ratio features structures, which cause an open circuit and degrades the device quality. It is extremely difficult to deposit continuous thin films of Cu at this thickness and instead islands of Cu tend to be more favourable.[11] Of these deposition approaches, ALD shows the most promise in surmounting the island growth problem as well as meeting future demands of device scaling. [12]

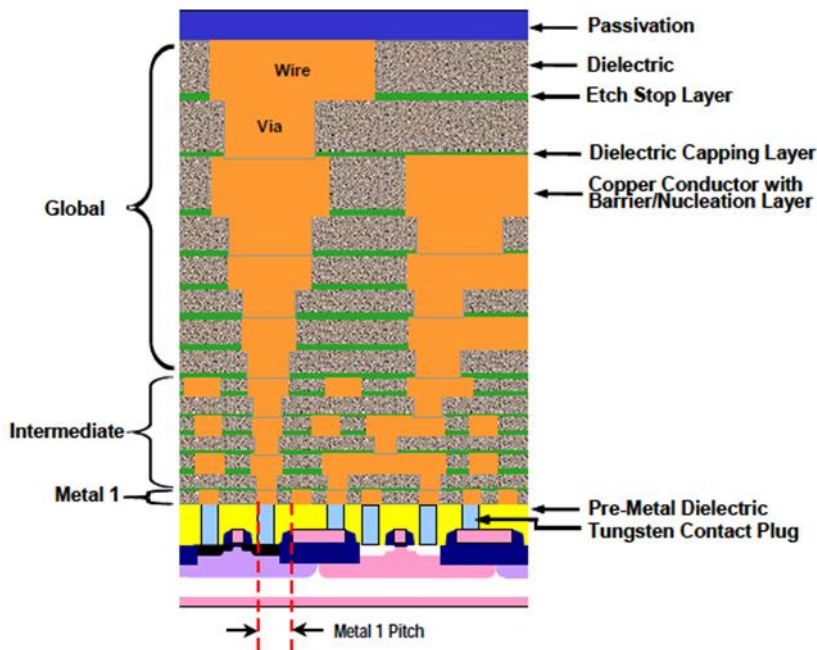


Figure 1.2. Typical Cross-sections of Hierarchical Scaling for microprocessor unit (MPU). (image from ITRS 2009 edition).[7]

Table 1.1 lists research articles dedicated to copper ALD. One of the first studies to deposit copper thin film involve using copper (I) chloride [CuCl] with H<sub>2</sub> as the precursor at a temperature of 350–500 °C.[13,14] Later, a three step ALD process was reported based on the reaction of CuCl and H<sub>2</sub>O and further reduction of Cu<sub>2</sub>O to metallic copper by H<sub>2</sub>. [15] The reactions of various copper (I) and copper (II)

## 1. Introduction and Overview

---

organometallic compounds, as the structures are shown in Figure 1.3, with molecular or plasma  $H_2$  have been reported as a way to achieve copper metal ALD. These include ALD of copper based on the reaction of  $Cu(acac)_2$  (copper acetylacetonate) with molecular  $H_2$  at 250 °C,  $[Cu(iPr-amd)]_2$  (copper propylamidinate) with  $H_2$  at 280 °C and  $Cu(tmhd)_2$  ( $tmhd = 2,2,6,6$ -tetramethyl-3,5- heptanedionate) and  $H_2$  plasma at 180 °C.[16–20] Unfortunately, the typical temperature requirement for these reactions (200–400 °C) causes dewetting which leads to discontinuous copper films. Significant progress was made by Sung *et al.* with low temperature ALD of copper metal using the reaction of copper dimethylamino-2-propoxide  $[Cu(dmap)_2]$  and diethylzinc  $[ZnEt_2]$  at 100–120 °C.[12] Although subsequent work reported that the parasitic chemical vapour deposition reaction of  $ZnEt_2$  may lead to Zn incorporation into the copper thin film,[11] the work by Sung *et al.* has important implications on the co-reagent strategy which was traditionally limited to the use of molecular or plasma  $H_2$ . Vidjayacoumar *et al.* investigated ALD reactions of the eight different copper (II) complexes separately with  $AlMe_3$ ,  $Bet_3$  and  $ZnEt_2$  in order to identify the most promising combination of the copper precursor and co-reagent.[11,21] Knisley *et al.* reported a low temperature ALD which involves a three-step process using  $Cu(dmap)_2$ , formic acid ( $HCO_2H$ ) and hydrazine ( $N_2H_4$ ) at 120 °C and indicated that their method can avoid undesired elements in the precursors, and affords high purity, low resistivity copper metal.[22] Kalutarage *et al.* compared two-step and three-step processes using the ALD reaction of the  $Cu(dmap)_2$  with  $BH_3(NHMe_2)$  and separately with  $BH_3(NHMe_2)$  and  $HCO_2H$ . [23] They showed that the two-step process requires a Cu seed layer, and affords a growth rate of about 0.13 Å/cycle within the 130–160 °C ALD window. The three-step process does not need a Cu seed layer for growth, and affords a growth rate of 0.20 Å/cycle within the 135–165 °C ALD window. Our

## 1. Introduction and Overview

experimental colleagues in Tyndall reported plasma enhanced ALD using two different precursors AbaCus and CTA-1 with H<sub>2</sub> plasma at temperature of 30–60 °C[24] and using NHC-Cu(hmds) with H<sub>2</sub> plasma on different substrates at 190–250 °C.[25] They found that the film structure is extremely dependent on the substrate material and that Cu agglomerates into islands on many materials including TaN, Si and CDO (carbon-doped SiO<sub>2</sub>) even at temperatures as low as 30 °C, while on Ru and Pd very thin conductive films could be grown.

Table 1.1. Literature review of copper atomic layer deposition.

Year, Ref.	Precursor	Reducing agent	Temp. (°C)	Substrate	Growth rate
1992, [13]	CuCl	H <sub>2</sub>	500	Si, SiO <sub>2</sub>	
1997, [14]	CuCl	H <sub>2</sub>	360–400	Ta	8 Å/min
2000, [16]	Cu(acac) <sub>2</sub>	H <sub>2</sub>	250	Ti	
2003, [17]	[Cu(iPr-amd)] <sub>2</sub>	H <sub>2</sub>	280	Si	0.5 Å/cycle
2004, [15]	CuCl	H <sub>2</sub> O, H <sub>2</sub>	375–475	Al <sub>2</sub> O <sub>3</sub>	1.6 Å/cycle
2005, [18]	Cu(tmhd) <sub>2</sub>	H <sub>2</sub> plasma	180	SiO <sub>2</sub> , Au	0.12 Å/cycle
2005, [19]	Cu(acac) <sub>2</sub>	H <sub>2</sub> plasma	140	Si	0.18 Å/cycle
2006, [20]	[Cu( <sup>t</sup> Bu-amd)] <sub>2</sub>	NH <sub>3</sub> , H <sub>2</sub>	160	Ru/TaN	
2008, [26]	Cu(acac) <sub>2</sub>	H <sub>2</sub> plasma	165	Ru	
2009, [12]	Cu(dmap) <sub>2</sub>	Et <sub>2</sub> Zn	100–120	Si	0.2 Å/cycle
2010, [11]	CuL <sub>2</sub> <sup>a</sup>	AlMe <sub>3</sub> , BEt <sub>3</sub> , ZnEt <sub>2</sub>	130–150	SiO <sub>2</sub>	
2010, [27]	[Cu( <sup>t</sup> Bu-amd)] <sub>2</sub>	H <sub>2</sub>	220	SiO <sub>2</sub>	
2011, [28]	Cu(dmamb) <sub>2</sub>	H <sub>2</sub> plasma	150	Ta	0.65 Å/cycle
2011, [22]	Cu(dmap) <sub>2</sub>	HCO <sub>2</sub> H, N <sub>2</sub> H <sub>4</sub>	120	Si	0.5 Å/cycle
2013, [24]	AbaCus, CTA-1	H <sub>2</sub> plasma	30–60	Ru, TaN CDO	0.2 Å/cycle, 0.3 Å/cycle
2013, [29]	Cu(nhc)(hmds)	H <sub>2</sub> plasma	225	Si	0.2 Å/cycle
2014, [23]	Cu(dmap) <sub>2</sub>	BH <sub>3</sub> (NHMe <sub>2</sub> ), BH <sub>3</sub> (NHMe <sub>2</sub> ) & HCO <sub>2</sub> H	130–160 135–165	Pd, Pt	0.13 Å/cycle 0.2 Å/cycle
2014, [25]	NHC-Cu(hmds)	H <sub>2</sub> plasma	190–250	Ru, Pd	0.4 Å/cycle

<sup>a</sup>in ref [11], eight different copper (II) complexes are used with AlMe<sub>3</sub>, BEt<sub>3</sub>. “L” in precursor CuL<sub>2</sub> separately represents acetylacetonate (acac), hexafluoroacetylacetonate (hfac), N-isopropyl-β-ketiminate (acnac), N,N-dimethyl-β-diketiminate (nacnac), 2-pyrrolylaldehyde (PyrAld), N-isopropyl-2-pyrrolyl-aldiminate (PyrImiPr), N-ethyl-2-pyrrolylaldiminate (PyrImEt), and N-isopropyl-2-salicylaldehyde (IPSA).

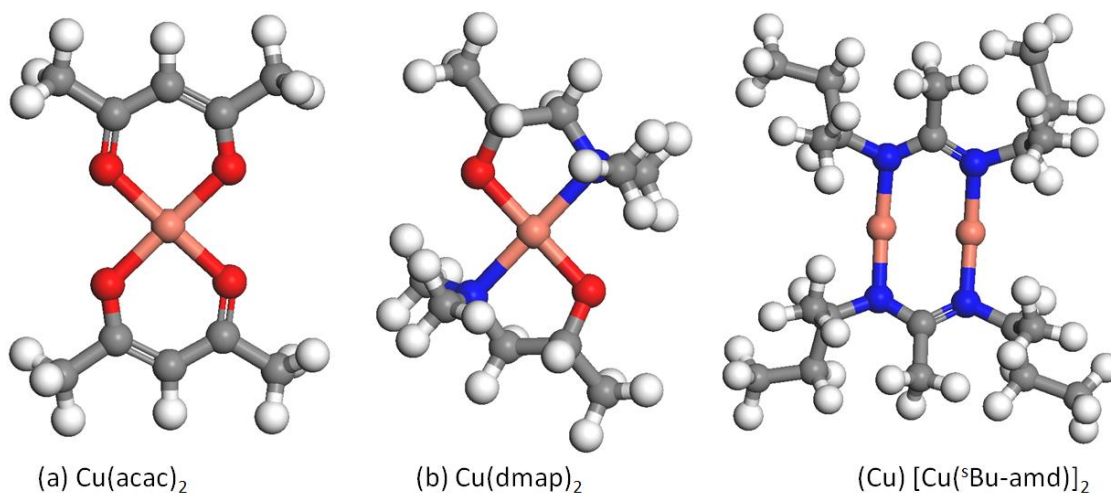


Figure 1.3. Examples of copper ALD precursor molecules. Colour scheme: red=O, salmon pink=Cu, blue=N, grey=C and white=H.

ALD has also been successfully applied to deposit transition metals (e.g. nickel, ruthenium, iridium, platinum, and palladium) and their alloys (e.g. RuPt,[30] PdPt[31,32]) because thin films and nanostructures of these transition metals and alloys have a wide range of current and future applications in many technologies such as plasmonic devices[33] spintronics[34] and catalysis[35]. We believe that careful investigation of Cu ALD as the model system for metal ALD could explain the reaction mechanisms and surface chemistry of other metals.

### 1.3 Challenges of Cu ALD

Despite the substantial progress towards achieving uniform and continuous ultrathin film of copper, the following problems are hindering its widespread applications.

First, island formation during ALD of copper. The growth mode of copper on a substrate is dependent on the adhesion energies between copper island and the substrate, the surface energies of copper and substrate, and stress between islands or film and the substrate caused by lattice mismatch and grain boundaries (GB). In general, copper thin films can grow during ALD through three different growth modes



## 1. Introduction and Overview

---

(Figure 1.4): layer by layer (Frank–van der Merwe growth), 3D island formation (Volmer–Weber growth), and 2D layer deposition followed by the growth of 3D islands (Stranski–Krastanov growth).[36] Many scanning electron microscope (SEM) images of ALD deposited copper show island formation on different substrates.[24,25,29] This indicates that deposition of copper on a substrate follows 3D island growth mechanisms (Volmer–Weber growth). These 3D islands finally transform into a thin film through Ostwald ripening and coalescence as the growth cycles increase. The critical thickness for transformation from 3D islands to thin film is strongly dependent on the thermodynamics of copper/substrate and on the composition of the substrate, e.g. defects, dopants, and chemical groups at the surface.

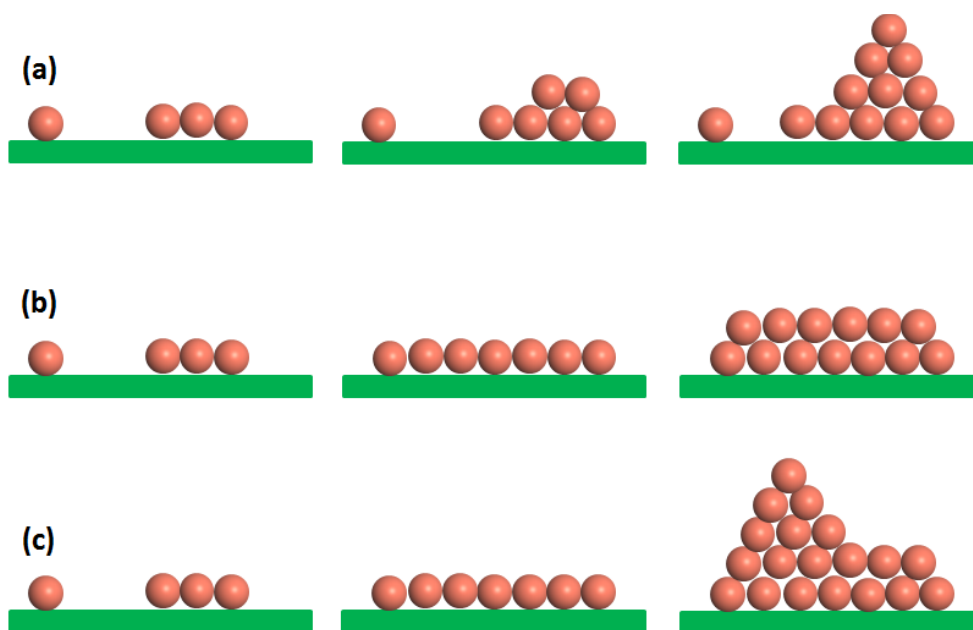


Figure 1.4. Three different thin film growth modes (a) Volmer–Weber mode (3D island growth), (b) Frank–van der Merwe (layer by layer growth), (c) Stranski – Krastanov (mixed growth).

Second, lack of understanding of the reaction mechanisms and surface chemistry during ALD of copper. Many theoretical and computational works were dedicated to the understanding of the reaction mechanisms of metal oxide ALD.[37–40] However,

## 1. Introduction and Overview

---

the reaction mechanisms and surface chemistries of copper ALD process remain largely unclear. Experimental works on copper ALD have mainly focused on the growth rate and characterization of copper thin films and not on the chemical mechanisms.

Third, scarcity of suitable precursors. As we discussed earlier, a successful ALD process requires suitable chemical precursors. The organometallic copper complexes which satisfy all the requirements of a good ALD precursor are rare. Thus, the development of new precursors and co-reagents is necessary for further progress in copper ALD.

Last but not least, identifying effective co-reagents. Co-reagents that reduce the chemisorbed copper precursor to metallic copper are far less available compared to the copper precursor itself. Chemisorption of the first precursor on the substrate yields a monolayer of precursor molecules bound to or dissociated on the surface. As we discuss later, van der Waals (vdW) interactions play important role in correctly describing the energetics and geometries of precursor adsorption on the surface. However, this monolayer is not the target material that we want to achieve and we need to reduce the metal cations to the desired thin film. To this end, it is necessary to identify effective reducing agents to react with the chemisorbed precursors at the surface without producing any impurities and with higher growth rate. The  $H_2$  molecule or plasma is used frequently (Table 1.1). If more than one co-reagent is used during ALD, the process becomes a three-step process, namely, chemisorption of the first precursor, conversion to reducible compounds and reduction of the compound to the target metal. Thus it is called indirect ALD if multiple reducing agents are used.

Understanding the role of co-reagents and how they reduce the chemisorbed copper precursor is crucial for designing improved ALD process for copper and other metals.

### 1.4 Thesis overview and scope

The theoretical approach behind our entire computational work is Density Functional Theory (DFT). In Chapter 2, I will briefly review its fundamentals and the most relevant parts for the modelling of surface chemistry during ALD of copper.

Despite the success of Cu ALD in recent years, the islanding and nucleation of Cu on the substrate remains a main challenge. In Chapter **Error! Reference source not found.**, we build a model to describe the nucleation process based on our *ab-initio* calculations. We apply this model to explain copper islanding on the Ru(0001) and SiO<sub>2</sub>(111) surface. In particular, relative stability of islands with different contact angle and critical thickness of transforming from islands to thin film will be studied.

The first step of an ALD process is the adsorption of precursor molecules. Understanding how precursor molecules adsorb on the substrate has a crucial role in unravelling the full reaction mechanism of an ALD process. In Chapter 4, we study the adsorption of a popular Cu precursor, copper dimethylamino-2-propoxide [Cu(dmap)<sub>2</sub>], on the Cu surfaces and compare the adsorption behaviour of Cu(acac)<sub>2</sub>. We show that the precursor adsorption geometries are crucial to understand the reaction mechanism.

Based on the results from Chapter 4, we investigate the surface chemistry for Cu ALD reaction from [Cu(dmap)<sub>2</sub>] and via the co-reagent Et<sub>2</sub>Zn in Chapter 5. We calculate

## 1. Introduction and Overview

---

activation barriers and reaction energies for a series of surface reactions to propose reaction mechanism for depositing Cu through the ALD process.

Since the two-step ALD reaction has encountered some challenges, such as the lack of suitable precursor molecule and efficient reducing agent, three-step ALD processes are considered as a promising method to deposit Cu thin film at low temperature. The third step is reduction of a copper compound (e.g. CuO) to metallic copper. To better understand this reducing step, in Chapter 6 we investigate the reduction of CuO surface using oxygen vacancy formation and H<sub>2</sub> adsorption, which can be experimentally achieved through vacuum annealing and reducing with H<sub>2</sub>, respectively.

In the last chapter, I summarize the important results of the thesis and describe the potential future work.

## 2 Theoretical Background

Density functional theory (DFT) is an extremely powerful tool for studying various problems in physics, chemistry and material science. It is a computational scheme to efficiently solve the Schrödinger equation for complex many-body systems from *first principles*. This chapter outlines the basic concepts of DFT as the entire work in this thesis is based on calculations using DFT. First I describe the many-body problem as the target to be solved with DFT and introduce the Hohenberg-Kohn theorem and the Kohn-Sham equation. Second, I will briefly mention GGA+U and hybrid DFT methods as I used them in some cases. Third, I will summarize the methods for including van der Waals (vdW) interactions in DFT calculations. Last, I introduce *ab initio* atomistic thermodynamics, a method to combine DFT with thermodynamics.

### 2.1 Density functional theory

#### 2.1.1 The Many-body problem

The basis for all quantum mechanical calculations of the electronic structure of a material is the time-independent Schrödinger equation,

$$H\psi(r, R) = E\psi(r, R) \tag{2.1}$$

where  $H$  is the Hamiltonian operator,  $E$  is the energy eigenvalue and  $\psi$  is the wave function.  $r$  and  $R$  list all the coordinates of the electrons and nuclei, respectively. Using atomic units (i.e.  $m_e = \hbar = e = 1$ ), a nonrelativistic system of electrons and nuclei can be described with a Hamiltonian[41],

## 2. Theoretical Background

---

$$H = -\frac{1}{2} \sum_i \nabla_i^2 - \sum_I \frac{\hbar^2}{2M_I} \nabla_I^2 + \frac{1}{2} \sum_{i \neq j} \frac{e^2}{|\mathbf{r}_i - \mathbf{r}_j|} + \frac{1}{2} \sum_{I \neq J} \frac{Z_I Z_J e^2}{|\mathbf{R}_I - \mathbf{R}_J|} - \sum_{i,I} \frac{Z_I e^2}{|\mathbf{r}_i - \mathbf{R}_I|} \quad (2.2)$$

where electrons are denoted by lower case subscripts and where nuclei, with charge  $Z_I$  and mass  $M_I$ , are denoted by upper case subscripts. The first and second terms denote the kinetic energies of electrons ( $T_e$ ) and nuclei ( $T_n$ ), respectively. The last three terms depict the electron–electron ( $V_{ee}$ ), nuclei–nuclei ( $V_{nn}$ ) and electron–nuclei ( $V_{en}$ ) interactions, respectively. For convenience, Equation (2.2) can be rewritten,

$$H = T_e + T_n + V_{ee} + V_{nn} + V_{en} \quad (2.3)$$

Solving the Schrödinger equation analytically for more than a few particles is not feasible, but it can be solved with approximate methods. The first approximation to reduce the complexity is to assume independence of the nuclear and electron wave functions and then treat the slow-moving nuclei as classical particles. This is the Born-Oppenheimer approximation.[42] In the following section we introduce the theoretical basis of DFT.

### 2.1.2 The Hohenberg-Kohn theorems

The theorems initially formulated by Hohenberg and Kohn[43] constitute the theoretical basis of DFT. The first Hohenberg-Kohn theorem legitimizes the use of electron density  $n(\mathbf{r})$  as the basic variable. It states:

*Theorem 1 (Uniqueness):* For any system of interacting particles in an external potential  $V_{\text{ext}}(\mathbf{r})$ , the potential  $V_{\text{ext}}(\mathbf{r})$  is determined uniquely, except for a constant, by the ground state particle density  $n_0(\mathbf{r})$ .

## 2. Theoretical Background

---

An alternative explanation of this theorem: all the properties of the system are completely determined given only the ground state density  $n_0(\mathbf{r})$ . For example, the kinetic energy of the electrons  $T_e$ , etc, is uniquely determined if  $n(\mathbf{r})$  is specified.

*Theorem II (Universality):* A universal functional for the energy  $E[n]$  in terms of the density  $n(\mathbf{r})$  can be defined, valid for any external potential  $V_{\text{ext}}(\mathbf{r})$ . For any particular  $V_{\text{ext}}(\mathbf{r})$ , the exact ground state energy of the system is the global minimum value of this functional, and the density  $n(\mathbf{r})$  that minimizes the functional is the exact ground state density  $n_0(\mathbf{r})$ .

According to theorem II, all the properties including the total energy can be viewed as functionals of the density,

$$\begin{aligned} E_{HK}[n] &= T[n] + E_{\text{int}}[n] + \int d^3r V_{\text{ext}}(\mathbf{r})n(\mathbf{r}) + E_{II} \\ &= F_{HK}[n(\mathbf{r})] + \int d^3r V_{\text{ext}}(\mathbf{r})n(\mathbf{r}) + E_{II} \end{aligned} \quad (2.4)$$

where  $E_{II}$  is the interaction energy of the nuclei. The functional  $F_{HK}[n]$  includes all internal energies and kinetic energies of the interacting electron system,

$$F_{HK}[n(\mathbf{r})] = T[n] + E_{\text{int}}[n] \quad (2.5)$$

If the functional  $F_{HK}[n(\mathbf{r})]$  was known, then it would be possible to find the exact ground state density and energy by minimizing the total energy of the system in equation (2.4).

### 2.1.3 The Kohn-Sham equation

The basic idea of the Kohn–Sham approach is to replace the many-particle problem with a system of non-interacting particles which has the same ground state density  $n(\mathbf{r})$

## 2. Theoretical Background

---

as the original many-particle system.[44] According to the Kohn–Sham approach, the Hohenberg-Kohn expression for the ground state energy functional (2.4) can be rewritten as

$$E_{KS} = T_s[n] + \int dr V_{ext}(r)n(r) + \frac{1}{2} \int d^3r d^3r' \frac{n(r)n(r')}{|\mathbf{r} - \mathbf{r}'|} + E_{II} + E_{xc}[n] \quad (2.6)$$

where  $T_s[n]$  is non-interacting particle kinetic energy. The third term is the Hartree energy and  $E_{xc}[n]$  is the exchange and correlation energy.

Performing variation of the energy in (2.6),

$$\delta E[n] = 0 \quad (2.7)$$

gives,

$$\frac{\delta E_{KS}}{\delta n(r)} = V_{ext} + \frac{1}{2} \int d^3r' \frac{n(r')}{|\mathbf{r} - \mathbf{r}'|} + \frac{\delta T_s[n]}{\delta n(r)} + \frac{\delta E_{xc}[n]}{\delta n(r)} \quad (2.8)$$

Defining the effective potential  $V_{eff}$  in the above equation,

$$V_{eff} = V_{ext} + \frac{1}{2} \int d^3r' \frac{n(r')}{|\mathbf{r} - \mathbf{r}'|} + \frac{\delta E_{xc}[n]}{\delta n(r)} \quad (2.9)$$

yields a set of Schrödinger-like equations, also called the Kohn-Sham equation.

$$H_{eff}\psi_i(r) = \left[ -\frac{1}{2}\nabla^2 + V_{eff} \right] \psi_i(r) = \epsilon_i\psi_i(r) \quad (2.10)$$

The ground state density is given by,

$$n(\mathbf{r}) = \sum_{i=1}^N |\psi_i(\mathbf{r})|^2 \quad (2.11)$$

where the sum is over the  $N$  lowest eigenstates of  $H_{eff}$  given in (2.10).



### 2.2 Approximation of exchange-correlation energy

One of the great challenges in electronic structure calculations is determining the exchange correlation energy  $E_{xc}$  because it needs to be approximated.[41] One such approach is the local density approximation (LDA),[45] in which  $E_{xc}$  is simply an integral over all space with  $E_{xc}$  assumed to be the same as in a homogeneous electron gas. The generalized gradient approximation (GGA)[46] considers functions that modify the behaviour at large gradients in such a way as to preserve desired properties. These methods have been widely used to describe many systems.

However, LDA or GGA methods fail to correctly describe systems like transition metal oxides and rare earth systems, where the electrons are strongly interacting. Introducing a strong intra-atomic interaction in a (screened) Hartree-Fock like manner, or as an on-site adjustment to the LDA or GGA can alleviate this problem. This may be done by including an orbital dependent Hubbard U term that is fitted so as to match a known property.[47]

In Figure 2.1, we draw the calculated lattice parameter of bulk Cu as the function of total energy. The calculated lattice parameter for Cu is 3.631 Å and bulk modulus is 134.3 GPa, which are in good agreement with the experimental values of 3.615 Å and 138 GPa.[48] Thus we use the generalized gradient approximation (GGA) and Perdew–Burke–Ernzerhof (PBE) functional[46,49] to calculate the adsorption and reactions on Cu surfaces.

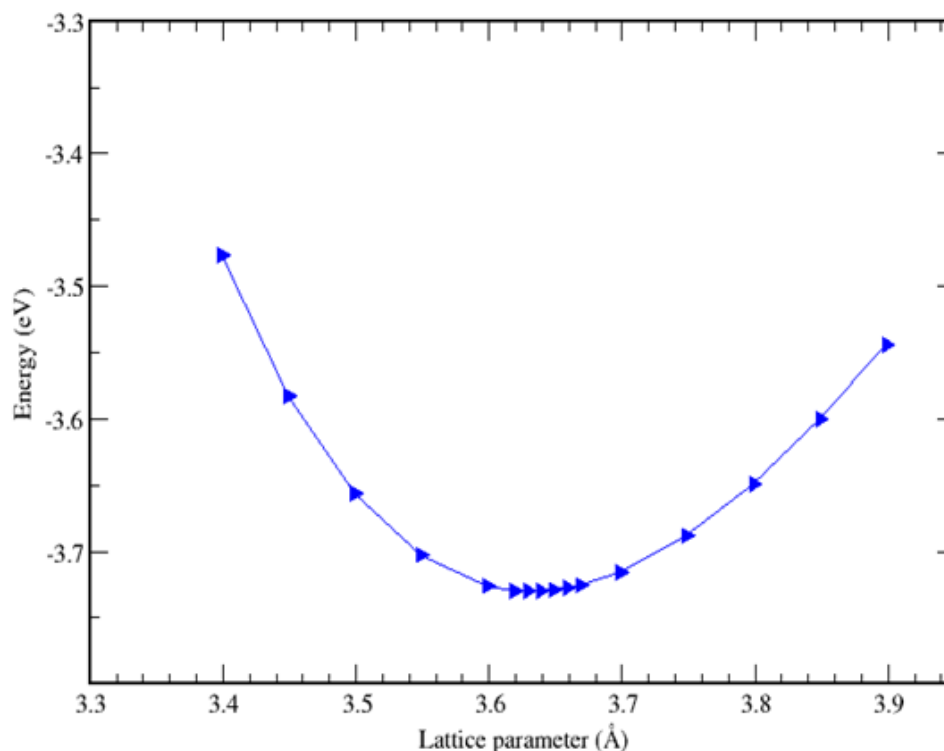


Figure 2.1. The calculated lattice parameter as a function of total energy using PBE functional.

### 2.3 Van der Waals (vdW) force

The vdW force is found to be crucial to accurately describe non-bonded interactions such as between molecules or at interfaces. In ALD modelling, we study the reactions of precursors, usually organometallic compounds, with solid surfaces, and thus vdW forces must be treated carefully. Unfortunately, the standard DFT with exchange-correlation functionals (local density approximation [LDA], Perdew-Burke-Ernzerhof [PBE]) does not include nonlocal vdW interactions, and thus different approaches have been proposed in order to incorporate vdW forces in DFT calculation.[50]

One of the approaches is the addition of empirical, pairwise inter-atomic dispersion corrections of the form  $-C_6r^{-6}$ , commonly referred to as DFT plus dispersion (DFT-D).[51,52] In the DFT-D3 method, the total energy is given by[53]

## 2. Theoretical Background

---

$$E_{DFT-D3} = E_{KS-DFT} - E_{disp} \quad (2.12)$$

where  $E_{KS-DFT}$  is the usual self-consistent Kohn–Sham energy as obtained from the chosen DF and  $E_{disp}$  is the dispersion correction as a sum of two- and three-body energies

$$E_{disp} = E^{(2)} + E^{(3)} \quad (2.13)$$

The most important two-body term is given by,

$$E^{(2)} = \sum_{AB} \sum_{n=6,8,10,\dots} s_n \frac{C_n^{AB}}{r_{AB}^n} f_{d,n}(r_{AB}) \quad (2.14)$$

here the first sum is over all atom pairs in the system,  $C_n^{AB}$  denotes the averaged (isotropic)  $n^{\text{th}}$ -order dispersion coefficient (orders  $n=6,8,10,\dots$ ) for atom pair AB, and  $r_{AB}^n$  is their inter-nuclear distance. Damping functions  $f_{d,n}$  are used to determine the range of the dispersion correction.

$$f_{d,n}(r_{AB}) = \frac{1}{1 + 6 \left( r_{AB} / (s_{r,n} R_n^{AB}) \right)^{-\alpha_n}} \quad (2.15)$$

where  $s_{r,n}$  is the order-dependent scaling factor of the cutoff radii  $R_n^{AB}$ . [54]

The long-range part of the interaction between three ground-state atoms can be obtained by applying the concept of short-range damping analogously as for the pairwise term,

$$E^{(3)} = \sum_{ABC} f_{d,3}(\bar{r}_{ABC}) E^{ABC} \quad (2.16)$$

where the sum is over all atom triples ABC in the system and geometrically averaged radii  $\bar{r}_{ABC}$  is used as a damping function. The triple-dipole dispersion term  $E^{ABC}$  is

## 2. Theoretical Background

---

$$E^{ABC} = \frac{C_9^{ABC} (3\cos\theta_\alpha \cos\theta_b \cos\theta_c + 1)}{(r_{AB}r_{BC}r_{CA})^3} \quad (2.17)$$

Where  $\theta_\alpha$ ,  $\theta_b$  and  $\theta_c$  are the internal angles of the triangle formed by  $r_{AB}$ ,  $r_{BC}$  and  $r_{CA}$  and  $C_9^{ABC}$  is the triple-dipole constant which can be found in ref [53].

Another promising method to include the vdW interaction in DFT is the nonlocal vdW density functional (vdW-DF) by Langreth and Lundqvist and co-workers[55] which is implemented in the VASP code.[56,57] In vdW-DF the non-local correlation is calculated in that the exchange–correlation energy takes the form

$$E_{xc} = E_x^{GGA} + E_c^{LDA} + E_c^{nl} \quad (2.18)$$

where  $E_x^{GGA}$  is the GGA exchange energy.  $E_c^{LDA}$  accounts for the local correlation energy obtained within the local density approximation (LDA) and  $E_c^{nl}$  is the non-local correlation energy.  $E_c^{nl}$  is exact at long distances between separated fragments,

$$E_c^{nl} = \int_0^\infty \frac{du}{2\pi} \text{tr}[\ln(1 - V\tilde{\chi}) - \ln \epsilon] \quad (2.19)$$

where  $\tilde{\chi}$  is the density response to a fully self-consistent potential with long-range, inter-fragment spectator contributions omitted.  $V$  is the inter-electronic Coulomb interaction,  $\epsilon$  is an appropriately approximated dielectric function, and  $u$  is the imaginary frequency.

We use these and similar methods for treating the vdW interaction along with the pure DFT method to identify the role of vdW forces on precursor adsorption on substrate during ALD of Cu, which will be explained in more detail in Chapter 4.

### 2.4 Bader charge

Electronic charges in molecules and solids are not observables and, therefore, not defined by quantum chemical theory. Many different schemes to assign electronic

## 2. Theoretical Background

---

charge distributed in space to a certain ion. An approach that focused on charge density has been proposed by Bader.[58] In this approach, space is divided into regions by surfaces that run through minima in the charge density. More precisely, at a point on a dividing surface the gradient of the electron density has no component normal to the surface, which is called *Bader regions*.[59] Henkelman *et al.* proposed an algorithm to calculate the charges on atoms based on Bader's theory.[59,60] In their algorithm, each point on a regular (x,y,z) grid is assigned to one of the regions by following a steepest ascent path on the grid.

### 2.5 *Ab initio* atomistic thermodynamics

Ground state DFT is a zero-temperature and zero-pressure technique. As such, the results of total energy calculations at surfaces have to be connected with the ambient experimental conditions. *Ab initio* atomistic thermodynamics (also known as first principles thermodynamics) enable us to connect density functional calculations with external conditions by considering appropriate thermodynamic potentials, *e. g.* Gibbs free energy.[61–63] The surface free energy of a surface in contact with gases can be defined as following

$$\gamma(T, P_i) = \frac{1}{A} \left[ G - \sum_i N_i \mu_i(T, P_i) \right] \quad (2.20)$$

where  $G$  is the Gibbs free energy of the surface that we would like to study.  $\mu_i(T, P_i)$  is the chemical potential of the  $i$ th species under the external conditions and  $N_i$  is the number of atoms (or molecules) of the  $i$ th species in the considered reservoir.  $T$  and  $P_i$  are the temperature and partial pressures of the  $i$ th species. The most stable structures are characterized by the lowest surface free energy. In equation (2.20), not all the chemical potentials in the system are independent, and therefore we can reduce

## 2. Theoretical Background

---

the number of unknown  $\mu_i(T, P_i)$ . For example, the chemical potential of metal oxide MO (M=metal),

$$\mu_{MO} = \mu_M + \mu_O \quad (2.21)$$

where,  $\mu_{MO}$  and  $\mu_M$  can be approximated with the DFT energies of corresponding metal oxide (MO) and metal (M). in this way only one independent variable  $\mu_O$  remains in the left side of equation (2.20). For a surface in contact with certain gases (e. g. oxygen),

$$\mu_{\text{gas}}(T, P_i) = E_{\text{gas}}^{\text{tot}} + E_{\text{gas}}^{\text{ZPE}} + \Delta\mu_{\text{gas}}(T, P^0) + k_B T \ln\left(\frac{P}{P^0}\right) \quad (2.22)$$

where  $E_{\text{gas}}^{\text{tot}}$  is the total DFT energy of the gas,  $E_{\text{gas}}^{\text{ZPE}}$  is the zero point energy,  $\Delta\mu_{\text{gas}}(T, P^0)$  is the chemical potential of the gas at ambient pressure at  $T$ , which can be obtained from JANAF Thermochemical Tables.[64]

$$G = E^{\text{tot}} + F^{\text{vib}} + F^{\text{conf}} + PV \quad (2.23)$$

where  $E^{\text{tot}}$  is the total energy,  $F^{\text{vib}}$  is the vibrational free energy,  $F^{\text{conf}}$  is the configurational free energy. If we choose a reference system, e.g. a clean surface, we only have to calculate the difference in Gibbs free energy.

We employ *ab initio* atomistic thermodynamics in different occasions in this work, namely, the surface in contact with the precursors, the metal/substrate interface and the surface with the reducing agent.

## 3 Interface Composition of Cu/SiO<sub>2</sub> Interface

### 3.1 Introduction

Metal/dielectric interfaces are of great interest because of their widespread occurrence in microelectronic devices.[65] The Cu/SiO<sub>2</sub> interface, in particular, is crucial for metal-oxide-semiconductor (MOS) capacitors because copper is the main interconnect material and SiO<sub>2</sub> or C-doped SiO<sub>2</sub> is widely used as the low-k dielectric substrate. Willis *et al.* reported that Cu is stable on SiO<sub>2</sub> in an oxygen-free environment under thermal and electrical stress.[66] However, they measured significant Cu transport through SiO<sub>2</sub> as the sample was exposed to ambient gases or pure oxygen. This suggests that the oxidized copper is a source of copper ions that are transported through the SiO<sub>2</sub> via diffusion and drift, leading to the failure of the devices. For this reason, a diffusion barrier between the copper interconnect and the SiO<sub>2</sub> is necessary to prevent Cu migration into the dielectrics. At the Cu/SiO<sub>2</sub> interface, the formation of interface oxides and silicides depends on the ambient temperature and the partial pressure of oxygen gas. Understanding how the structure of these metal/dielectric interfaces depends on oxygen pressure and temperature thus has crucial importance for the reliability of electronic devices.

In this section, we determine the phase diagrams of Cu/SiO<sub>2</sub> interfaces as a function of oxygen pressure and temperature using *ab initio* atomistic thermodynamics, i. e. by combining the results of density functional theory (DFT) based calculations with the thermodynamics of the grand canonical ensemble. Our work offers an explanation for

### 3. Interface Composition of Cu/SiO<sub>2</sub> Interface

---

the impact of the oxygen environment on formation of the interfacial oxides and silicides at Cu/SiO<sub>2</sub> interfaces.

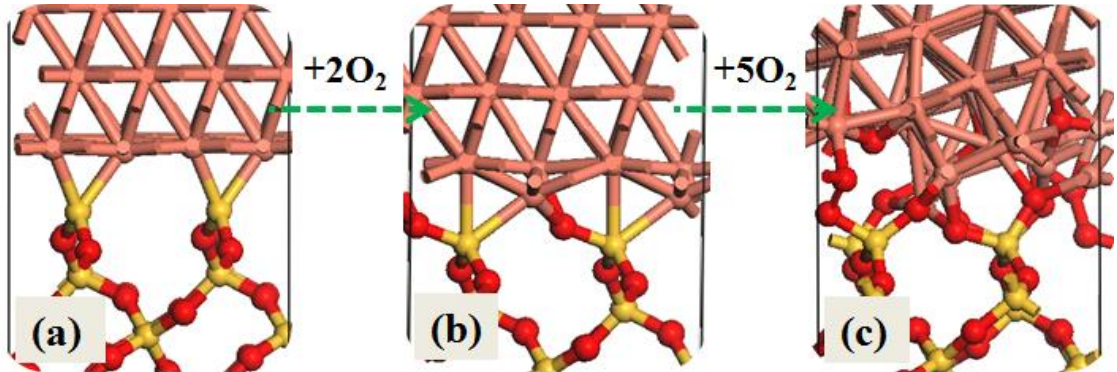


Figure 3.1. Optimized M:  $\theta$  SiO<sub>2</sub> interface structures with different interfacial O concentration ( $\theta_0$ ). (a)  $\theta = 0$ , (b) clean interfaces at  $\theta = 0.5$  and (c) Oxidized interfaces at  $\theta = 1.75$ . (red=O, yellow=Si, salmon-pink = Cu). Green dashed arrows represent a process that one oxygen atom at a time is added to the interface structures.

### 3.2 Computational methods

The Cu/SiO<sub>2</sub> interface model was constructed by positioning a (4 × 4) Cu(111) slab on top of the (2 × 2) SiO<sub>2</sub>(0001) slab and adding 12 Å thickness of vacuum. Half of the O atoms from the O-terminated SiO<sub>2</sub>(0001) surface were moved to the Si-terminated surface of the SiO<sub>2</sub> slab in order to eliminate the instability due to the dipole moment. The dangling O atoms at the bottom of the SiO<sub>2</sub> slabs were passivated with H atoms. The lattice parameters of the interface areas of the metal slabs were adjusted to those of SiO<sub>2</sub> in the plane of the interface and the resulting misfit of Cu/SiO<sub>2</sub> interfaces was about 2%.

The interfacial O concentration ( $\theta$ ) varies between  $0 \leq \theta \leq 1.75$  in units of 0.125 for Cu/SiO<sub>2</sub> interfaces, which can be represented by Cu:  $\theta$ : SiO<sub>2</sub>, where  $\theta$  is defined as the



### 3. Interface Composition of Cu/SiO<sub>2</sub> Interface

---

ratio of O atoms to the total number of Si and O atoms at the interface. Three representative interface structures, where  $\theta = 0, 0.5$  and  $1.75$ , are shown in Figure 3.1. When  $\theta = 0$ , the interface structures contain only Cu – Si bonds (Figure 3.1a), which corresponds to the formation of silicide structures in an oxygen lean environment. For  $\theta = 0.5$ , the number of O atoms equals the initial number of O in the initial SiO<sub>2</sub> slab, and equal numbers of Si and O atoms from the SiO<sub>2</sub> side of the interface form bonding with metal slabs, as shown in Figure 3.1b. When  $\theta = 1.75$ , the interfaces have excess amount of O atoms which results in significant interface reconstructions. These interfaces with  $\theta = 0, 0.5, 1.75$  are referred to as “silicide”, “clean” and “oxidized” interfaces, respectively. Later we will see from the phase diagrams that these interfaces with different  $\theta$  correspond to different oxygen pressure and temperature.

In order to obtain the interface phase diagrams, we employ *ab initio* atomistic thermodynamics,[67] which has been successfully applied to various systems including adsorption,[63] co-adsorption on surfaces[68–70] and interfaces.[71,72] For the Cu:  $\theta$ : SiO<sub>2</sub> interface structure in thermodynamic equilibrium, the interface free energy ( $\gamma_\theta$ ) can be obtained by

$$\gamma_{\theta_0} = \frac{1}{A} (G_{\theta_0} - n_{\text{Si}}\mu_{\text{Si}} - n_{\text{O}}\mu_{\text{O}} - n_{\text{Cu}}\mu_{\text{Cu}}) - \sigma_{\text{SiOH}} - \sigma_{\text{Cu}} \quad (3.1)$$

where  $G_\theta$  is the Gibbs free energy for Cu:  $\theta$ : SiO<sub>2</sub> interface,  $A$  is the interface area, and  $n_{\text{Si}}, n_{\text{O}}$  and  $n_{\text{Cu}}$  are the number of Si, O and Cu atoms in the system, respectively.  $\mu_{\text{Si}}$  and  $\mu_{\text{O}}$  are the chemical potential of Si and O in  $\alpha$ -quartz structure.  $\sigma_{\text{SiOH}}$  and  $\sigma_{\text{Cu}}$  are the surface energies of the non-interacting surfaces of the slab. Equation (3.1) can be written,

### 3. Interface Composition of Cu/SiO<sub>2</sub> Interface

---

$$\gamma_\theta = \frac{1}{A} (G_{\theta_0} - n_{\text{Si}} G_{\text{SiO}_2} - (n_{\text{O}} - 2n_{\text{Si}}) \mu_{\text{O}} - n_{\text{Cu}} G_{\text{Cu}}) - \sigma_{\text{SiOH}} - \sigma_{\text{Cu}} \quad (3.2)$$

where,

$$\mu_{\text{Si}} + 2\mu_{\text{O}} = G_{\text{SiO}_2}, \quad \mu_{\text{Cu}} = G_{\text{Cu}} \quad (3.3)$$

and here  $G_{\text{SiO}_2}$  and  $G_{\text{Cu}}$  are the Gibbs free energies of bulk quartz SiO<sub>2</sub> and bulk Cu, respectively. We further define the relative interface free energy ( $\Delta\gamma_\theta$ ) by using  $\gamma_{0.5}$  as a reference and replacing  $n_{\text{O}} - 2n_{\text{Si}}$  by  $4(2\theta - 1)$  in equation (3.2).

$$\Delta\gamma_\theta = \gamma_\theta - \gamma_{0.5} = \frac{1}{A} [E_{\theta_0} - E_{0.5} - 4(2\theta - 1) \Delta\mu_{\text{O}}(T, P_{\text{O}_2})] \quad (3.4)$$

Using the interface free energy relative to that of a reference system reduces the computational cost and determines the stability of various interface structures. Since the interface structures are assumed to be in thermodynamic equilibrium in contact with sources of molecular O<sub>2</sub>, the  $\mu_{\text{O}}$  is equal to half of  $\mu_{\text{O}_2}$ , which is a function of temperature ( $T$ ) and oxygen pressure ( $P_{\text{O}_2}$ ),

$$\mu_{\text{O}_2}(T, P_{\text{O}_2}) = E_{\text{O}_2}^{\text{DFT}} + \Delta\mu_{\text{O}_2}(T, P_{\text{O}_2}) \quad (3.5)$$

where  $E_{\text{O}_2}^{\text{DFT}}$  is the DFT energy of an O<sub>2</sub> molecule in gas phase. For the ideal gas,

$$\Delta\mu_{\text{O}_2}(T, P_{\text{O}_2}) = \Delta\mu_{\text{O}_2}(T, P^0) + k_B T \ln(P_{\text{O}_2}/P^0), \quad (3.6)$$

where  $k_B$  is the Boltzmann constant and  $\Delta\mu_{\text{O}_2}(T, P^0)$  can be obtained from JANAF thermodynamics tables.[64] In Equation (3.4), we neglect the configurational and vibrational contributions to the relative interface free energy because these two terms only result in minor changes to the interface phase diagrams.[73]

#### 3.3 Results and discussion

We calculate the relative interface free energy  $\Delta\gamma_\theta$ , which is defined in equation (3.4) as the difference between the interface free energy of Cu:  $\theta$ : SiO<sub>2</sub> and that of clean Cu: 0.5: SiO<sub>2</sub>. The relative interface free energies as a function of oxygen chemical potential are displayed in Figure 3.2. The lower boundary  $\Delta\mu_{O_2} = -5.0$  eV is defined to avoid the decomposition of bulk  $\alpha$ -quartz into silicon and oxygen. The straight lines with different slopes represent Cu:  $\theta$ : SiO<sub>2</sub> interface structures with different interfacial oxygen concentration  $\theta$ . Figure 3.1 shows the optimized structures of Cu:  $\theta$ : SiO<sub>2</sub> heterostructures. The silicide interface with  $\theta = 0$ , which has the line with the largest positive slopes, is the most stable phase between the oxygen chemical potentials of -5.0 and -3.38 eV. As we can see from Figure 3.1a, the Si atoms form bond with two Cu atoms with the bond distances of 2.36 Å. This indicates the formation of stable Cu<sub>2</sub>Si silicide structure at the interface under the oxygen lean condition. The clean interface with  $\theta = 0.5$  becomes stable within a narrow stability region. The three stable regions appear with excess O for the Cu:  $\theta$ : SiO<sub>2</sub> interface:  $0.5 < \theta < 0.875$ ,  $0.875 \leq \theta < 1.25$  and  $1.25 \leq \theta < 1.75$ , which have the borders at  $\Delta\mu_O = 2.91$  and  $1.29$  eV, respectively. The calculated formation energy of Cu<sub>2</sub>O,  $h_{Cu_2O} = 1.24$  eV,[74] approximately equal to the oxygen chemical potential where the lines corresponding to Cu: 1.25: SiO<sub>2</sub> and Cu: 1.75: SiO<sub>2</sub> interfaces. Figure 3.1c shows the significant rearrangement of interface atoms to form Cu – O bonding and the penetration of O atoms to the Cu slab, which is similar to previous computational works.[75,76] The Cu – O bond distance varies between 1.84 - 2.04 Å, which are the similar to the calculated Cu – O distance of 1.87 Å in bulk Cu<sub>2</sub>O. This implies the formation of stable Cu<sub>2</sub>O appears at the interface starting from  $\theta = 1.25$ .

### 3. Interface Composition of Cu/SiO<sub>2</sub> Interface

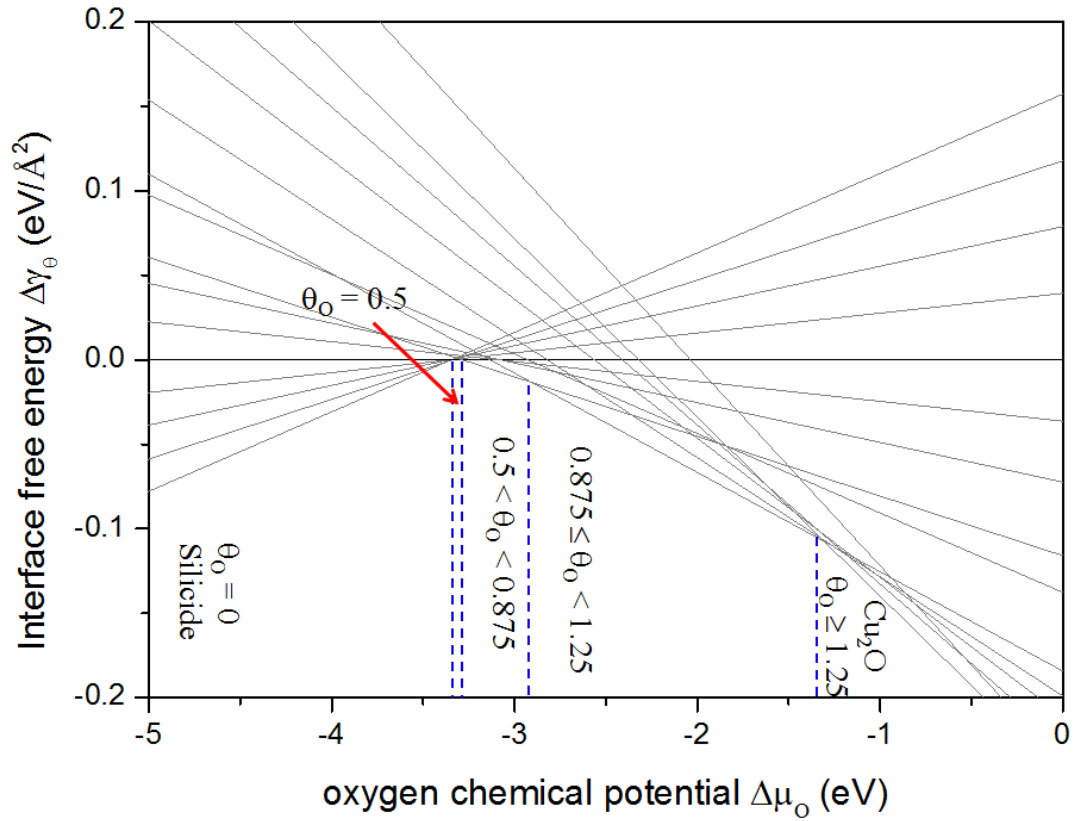


Figure 3.2. The relative interface free energy as a function of  $\Delta\mu(\text{O})$  for the Cu:  $\theta$ : SiO<sub>2</sub> interface. The vertical dashed lines are the boundaries between two different stable interface structures

The intersection points of the lowest lying lines in Figure 3.2 determines the certain values of oxygen chemical potential  $\Delta\mu_{\text{O}}$  as the boundary of two stable interface structures. Substituting these values of  $\Delta\mu_{\text{O}}$  to equation (6) yields phase diagrams as a function of oxygen pressure and temperature, which are shown in Figure 3.3. For the Cu :  $\theta$  : SiO<sub>2</sub> interface structure, the interfacial oxide phases prefer high oxygen pressure and low temperature while the silicide phases are stable at low oxygen pressure and high temperature. Valladares *et al.* obtained Cu<sub>2</sub>O in a Cu/SiO<sub>2</sub>/Si system obtained by thermal oxidation following annealing Cu thin film at 200 °C under atmospheric pressure.[77] They observed the mixture of Cu<sub>2</sub>O and CuO at the

### 3. Interface Composition of Cu/SiO<sub>2</sub> Interface

temperature of 250 – 300 °C. Benouattas et al. observed the silicide formation after annealing the Cu/SiO<sub>x</sub>/Si system at temperature of 600 – 750 °C and under a vacuum of  $6 \times 10^{-10}$  atm.[78] Our results are consistent with these experimental data at different temperature and pressure.

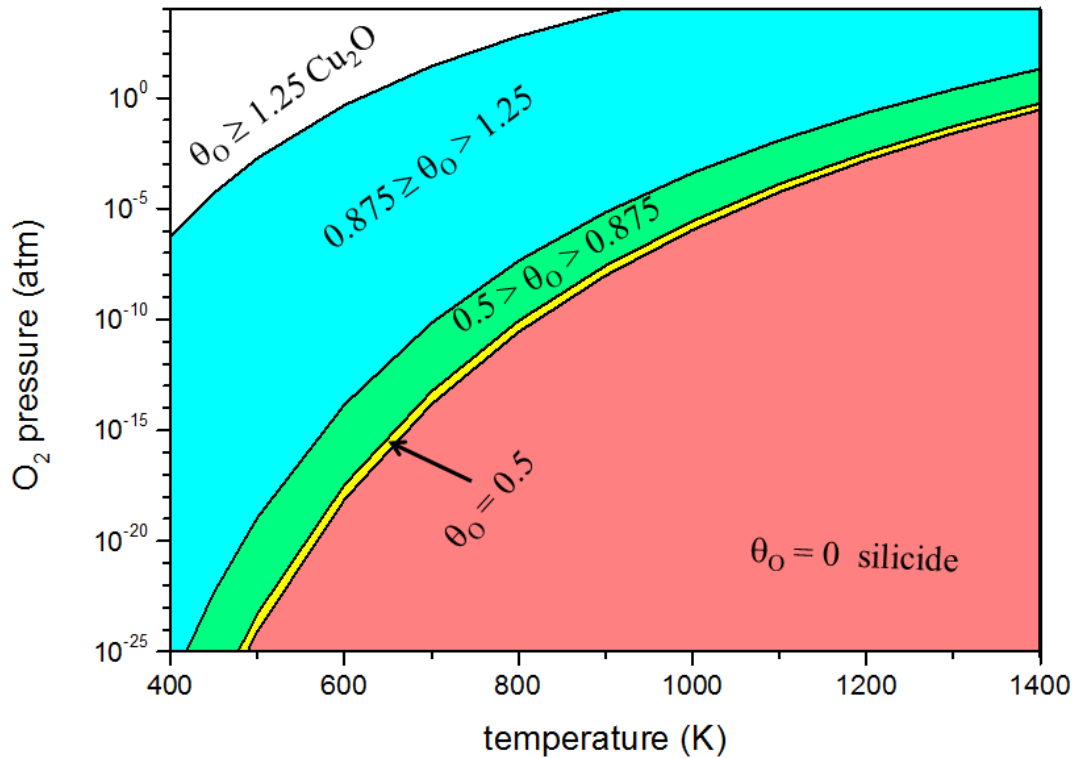


Figure 3.3. The interface phase diagrams of Cu/SiO<sub>2</sub>

In summary, we used ab initio atomistic thermodynamics to investigate the interface stabilities of Cu/SiO<sub>2</sub> interface. We calculated the interface free energies as a function of oxygen chemical potential for interface structures with different amount of interfacial oxygen content, from which the phase diagrams as a function of oxygen pressure and temperature are obtained. We demonstrate that our predicted temperature and oxygen pressure are in agreement with experimental results. Our result offers an

### 3. Interface Composition of Cu/SiO<sub>2</sub> Interface

---

explanation to determine the interface structures of Cu/SiO<sub>2</sub> interface in a range of oxygen pressure and temperature.

#### 3.4 Conclusion

The surface energy of SiO<sub>2</sub> and Cu/SiO<sub>2</sub> interface energy are dependent on the surface composition of SiO<sub>2</sub>, e.g. number of reactive oxygen atoms, and hydroxyl groups. We used *ab initio* atomistic thermodynamics to understand the level of interface oxygen at the Cu/SiO<sub>2</sub> interface as the function of oxygen chemical potential. From this the interface phase diagram as a function of oxygen pressure and temperature is obtained. We found that the interfacial oxide Cu<sub>2</sub>O phases prefer high oxygen pressure and low temperature while the silicide phases are stable at low oxygen pressure and high temperature for Cu/SiO<sub>2</sub> interface, which is in good agreement with experimental observations.

## 4 Precursor Adsorption on Copper Surfaces<sup>1</sup>

### 4.1 Introduction

Thin films of metals have a wide range of current and future applications in many technologies such as microelectronics,[17] plasmonic devices,[33] spintronics[34] and catalysis[35]. Atomic layer deposition (ALD) is one of the most promising techniques to deposit highly uniform and conformal thin films.[2] Metal thin films have been deposited both with thermal and plasma ALD using metalorganic compounds as precursors. In ALD, the first precursor adsorbs on the substrate in one ALD pulse and reacts at the surface with reducing co-reagents during the second pulse.[17,22] In contrast with the ALD of other metals, ALD growth of Cu has been relatively well established because of the availability of Cu precursors and because of the technological demand for Cu as a main interconnect material in electronics. Although several Cu ALD processes that use different Cu(I) and Cu(II) metalorganic compounds and co-reagents have been developed in the past,[19,20,24,25] a notable advance in low temperature Cu ALD processing was made by employing the reaction of copper dimethylamino-2-propoxide [Cu(dmap)<sub>2</sub>] (see Figure 4.1a) with diethylzinc (Et<sub>2</sub>Zn) at temperatures of 100 – 120 °C.[12] The growth mechanism of this process has been investigated using density functional theory (DFT) in a gas-phase model and it is predicted that the surface is probably covered with Cu(I) intermediates.[79] Later, a thin film of very pure Cu has been deposited using a three-step ALD process which entails the sequential reactions of Cu(dmap)<sub>2</sub>, formic acid and hydrazine (N<sub>2</sub>H<sub>4</sub>) at 120 °C.[22] Recently, low temperature Cu ALD has also been demonstrated using a

---

<sup>1</sup> (Some content of this chapter is published in in *The Journal of Physical Chemistry C*. See ref [147]).

#### 4. Precursor Adsorption on Copper Surfaces

---

two-step process of  $\text{Cu}(\text{dmap})_2$  and borane dimethylamine  $[\text{BH}_3(\text{NHMe}_2)]$  and a three-step process using  $\text{Cu}(\text{dmap})_2$ , formic acid and  $\text{BH}_3(\text{NHMe}_2)$ . [23] In these cases, the  $\text{Cu}(\text{dmap})_2$  precursor is successful because of its relatively high vapor pressure and thermal stability. Given these promising developments, the reaction mechanism and surface chemistry of  $\text{Cu}(\text{dmap})_2$  precursor during Cu ALD should be carefully investigated in order to identify better precursors and design new ALD processes for Cu as well as other metals.

In particular, we are interested to find out whether there is selectivity in the adsorption of molecules like  $\text{Cu}(\text{dmap})_2$  onto a growing Cu surface, and whether growth at islands or edges is favoured over layer-by-layer growth of the smooth surface. Island growth is one of the obstacles towards the use of ALD in the semiconductor industry. [24] The first step in a typical ALD process is the chemisorption of the precursor molecule on the surface, which is followed by a series of surface reactions, some of which may be irreversible due to desorption of by-products. The subsequent reactions are not possible in the case of weaker physisorption because the physisorbed precursors tend to desorb first, meaning that no ALD takes place. Thus, it is imperative to carefully investigate the adsorption of the precursors on the substrate. Zaera *et al.* studied the adsorption of metal ALD precursors on a metallic substrate using temperature programmed desorption (TPD) and X-ray photoelectron spectroscopy and showed the usefulness of experimental surface chemistry methods for the development of ALD. [80–82] Computational approaches such as electronic structure theory calculations can also be an efficient way to investigate the surface chemistry and reaction mechanism and thus shorten the process development time in the laboratory. However, very few computational studies on the surface chemistry of metal ALD are available in the literature. [83]



## 4. Precursor Adsorption on Copper Surfaces

---

Accurate description of the interaction between organometallic precursors like  $\text{Cu}(\text{dmap})_2$  and the substrate poses a theoretical challenge because the origin of the precursor/substrate interaction is complex, resulting mainly from a balance between van der Waals (vdW) interactions, charge transfer, Pauli repulsion, covalent and ionocovalent bonds and interaction between the permanent dipole of the adsorbates and image dipoles in the substrate.[84] Of these, the vdW interaction is poorly described in standard DFT functionals. A large supercell is necessary to include the  $\text{Cu}(\text{dmap})_2$  adsorbate (39 atoms, 9 Å in diameter), which makes the system computationally expensive, and thus using a higher level method such as the random phase approximation is not feasible at present.[50] New approaches for the approximate treatment of vdW interactions at the DFT level have recently been implemented, and so we are interested to discover whether they make it possible to quantitatively describe the interaction of the organometallic precursor with the substrate.

### 4.2 $\text{Cu}(\text{dmap})_2$ adsorption on Cu surface.

In the present theoretical work, we study the adsorption of the  $\text{Cu}(\text{dmap})_2$  molecule on Cu surfaces using DFT with various levels of treatment of vdW forces. This work specifically aims (i) to study the energetic, geometric and electronic properties of adsorbed  $\text{Cu}(\text{dmap})_2$  on different adsorption sites on the Cu substrate (both flat and rough bare surfaces); (ii) to investigate the role of vdW interactions between the molecule and surface in the initial stage of Cu ALD using several vdW inclusive DFT schemes; and (iii) to discuss the implications of various adsorption geometries of  $\text{Cu}(\text{dmap})_2$  for understanding the surface chemistry, island growth and reaction mechanism of ALD of copper.

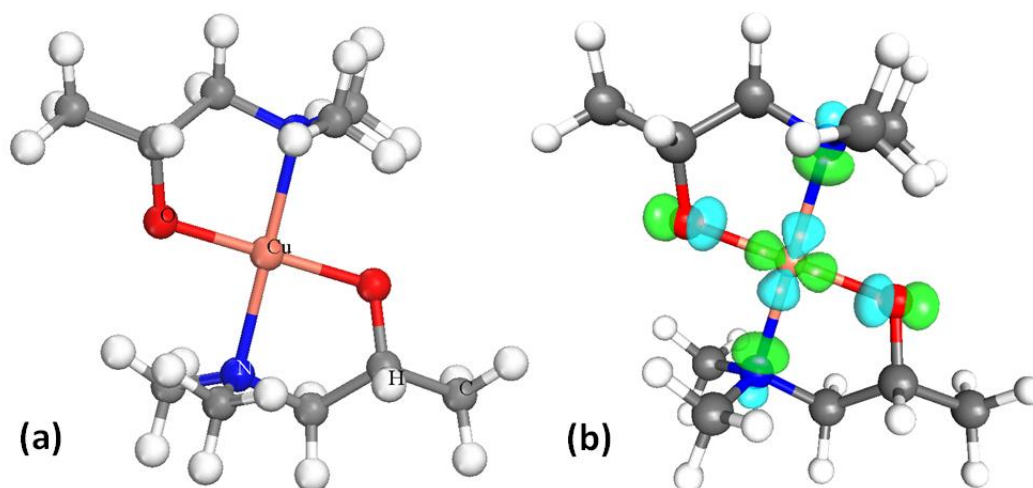


Figure 4.1. Copper dimethylamino-2-propoxide molecule  $[\text{Cu}(\text{dmap})_2]$ . (a) Optimized gas-phase structure; colour scheme: red – O, blue – N, salmon pink – Cu, grey – C and white – H. (b) Lowest unoccupied molecular orbital (LUMO).

### 4.2.1 Theoretical method

**Computational details.** The Vienna ab initio simulation package (VASP 5.3) was used for the periodic DFT calculations.[85] The projector augmented wave (PAW) approach[86] was applied for describing the effective potential of core electrons. The generalized gradient approximation (GGA) was employed with the exchange correlation functional of Perdew, Burke and Ernzerhof (PBE).[46] As Cu has a partially filled d shell, spin polarized calculations were performed throughout. Nevertheless, the resulting total spin moment was zero. The wave functions were expanded in the plane wave basis up to a cutoff energy of 450 eV. Because of the large cell sizes, it was found to be adequate to use only the  $\Gamma$  point to sample the Brillouin zone for both slab and gas phase calculations. The atomic positions of ions were optimized using a conjugate gradient algorithm until the forces on each ion were smaller than  $0.02 \text{ eV}/\text{\AA}$ . The geometry optimization for a single  $\text{Cu}(\text{dmap})_2$  molecule in the gas phase was performed by placing the molecule in a rhombohedral supercell

#### 4. Precursor Adsorption on Copper Surfaces

---

with  $\gamma = 60^\circ$  and a side length of 25 Å. The molecular orbital calculations were performed with the TURBOMOLE 6.4 suite of quantum chemical programs[87] using DFT within the GGA parameterization by PBE,[46] the resolution-of-identity (RI) approximation[88,89] and a split valence polarization basis set (def2-SVP).[90] The climbing-image nudged elastic band (CI-NEB) method was used for calculations of energy barriers between physisorbed and chemisorbed states.[91,92]

**Treatment of VdW Interaction.** Since no experimental data are currently available for the adsorption configuration of  $\text{Cu}(\text{dmap})_2$  on the Cu surface, it is not straightforward to fully validate our calculations and assess the role of vdW interaction for this system. The vdW interactions are found to be crucial for computing reliable geometries and energies for various organic/inorganic interfaces.[50] Thus, we choose several vdW inclusive DFT methods along with pure PBE to assess the role of vdW interactions for the  $\text{Cu}(\text{dmap})_2/\text{Cu}$  interface. Several articles give a detailed review of the development and challenges of vdW inclusive DFT methods.[50,93] The adsorption of a benzene molecule on metals is one of the most popular model systems to assess the performance of vdW inclusive DFT for the organic/solid interface.[94–99] Interatomic pairwise DFT-D methods by Grimme[51,53] are found to systematically overestimate the adsorption energies of benzene and several other molecules on metal surfaces.[99–101] As a result, they are used to represent an upper bound of the adsorption energy.[100,102] Hence, for this purpose we choose the latest version of this semi-empirical dispersion correction (PBE-D3)[53] with Becke-Johnson (BJ) rational damping.[103] The vdW-DF functional[55] and its second version (vdW-DF2)[56] are known to yield even smaller adsorption energies than PBE for various systems.[98,104–106] We therefore use the vdW-DF2 functional to estimate the lower bound of the adsorption energies. Yildirim *et al.* studied the

#### 4. Precursor Adsorption on Copper Surfaces

---

adsorption characteristics of benzene on coinage and transition metals to compare the performance of different vdW functionals.[95] They found that optPBE-vdW and optB88-vdW[56] functionals show systematically good agreement with “averaged” experimental adsorption energies. A comparative study by Carrasco *et al.* on the performance of the two classes of vdW-inclusive methods (the PBE+vdW[107] and the PBE+vdW<sup>surf</sup> methods[108]) for benzene adsorption on transition metals suggests that PBE+vdW<sup>surf</sup> and optB88-vdW predict adsorption energies and equilibrium geometries that are in equally good agreement with experimental data.[98] Keeping these in mind, we also choose the optB88-vdW method which is available in the VASP code. To conclude, the vdW inclusive methods that we have chosen in this paper along with pure PBE are PBE-D3, vdW-DF2 and optB88-vdW.

**Adsorption Models.** The calculated lattice parameters of fcc bulk Cu using the chosen vdW inclusive methods and PBE are 3.63 Å (PBE), 3.57 Å (PBE-D3) 3.74 Å (VDW-DF2) and 3.62 Å (optB88-vdW), compared with the experimental value of  $a_0=3.61$  Å.[109] These lattice parameters are used to build corresponding slab models in each method. The slabs consist of four atomic layers of Cu. All atomic layers are allowed to relax within a fixed cell. A vacuum 18 Å thick was added so as to separate adjacent slabs with adsorbate.

Three different Cu surfaces were used as substrates: flat Cu(111) surface, stepped Cu(332), and Cu(643) with a kink (see Figure 4.2). To accommodate the adsorbed precursor, a (6 × 6) surface expansion of Cu(111) is used, which gives the shortest H – H distance of 8.1 Å between adsorbate images in neighbouring cells and a precursor coverage of one Cu(dmap)<sub>2</sub> per 2 nm<sup>2</sup>. As schematically illustrated in Figure 4.2a, we take four different adsorption configurations into account on the Cu(111) surface:

#### 4. Precursor Adsorption on Copper Surfaces

---

these adsorption configurations are denoted as Cu(111)-T, Cu(111)-D, Cu(111)-M and Cu(111)-B according to the alignment of O – Cu – O bonds in the molecule relative to the surface. In the Cu(dmap)-T configuration, the adsorbate Cu atom aligns with the top of a Cu surface atom and the O atoms are slightly off the top of Cu atoms of one surface row. In Cu(111)-D, the O – Cu – O bond aligns with the long diagonal of four neighbouring Cu atoms. In this configuration, the two O atoms align on the top of two Cu surface atoms and the adsorbate Cu atom is at a bridge site. In the Cu(111)-M configuration, two O atoms are on the bridge sites and the adsorbate Cu atom is on the hollow site between rows. In the Cu(111)-B configuration, the adsorbate Cu atom is on a bridge site and the O atoms are slightly off bridge sites of the same row. As we will show in the following sections, these adsorption configurations give completely different descriptions of Cu(dmap)<sub>2</sub> adsorption on the Cu(111) surface.

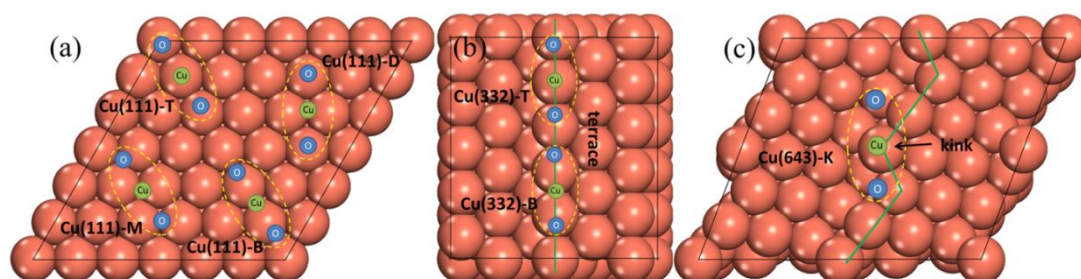


Figure 4.2. Adsorption models of Cu(dmap)<sub>2</sub> on different Cu surfaces. The initial position of O – Cu – O bonds of Cu(dmap)<sub>2</sub> on the surface are shown schematically. (a) Four adsorption sites on Cu(111) surface: Cu(111)-T, Cu(111)-D, Cu(111)-M and Cu(111)-B. (b) Two adsorption sites on the upper layer of the Cu(332) step: Cu(332)-T and Cu(332)-B. (c) Cu(643)-K. Abbreviations: T=top; D=diagonal; M=median; B=bridge; K=kink. The green lines on (b) and (c) show the edge atoms of the upper layer.

We use (5 × 1) and (2 × 2) surface expansions for the stepped Cu(332) surface and the Cu(643) surface with a kink, respectively (see Figure 4.2b-c). For the stepped

#### 4. Precursor Adsorption on Copper Surfaces

---

Cu(332) surface, two different adsorption sites are considered: Cu(332)-T and Cu(332)-B. In the Cu(332)-T configuration, the adsorbate Cu atom is aligned on the top of a Cu atom on the edge and the O atoms are slightly off the top of Cu surface atoms on the same edge. In Cu(332)-B, the adsorbate Cu atom is at the bridge site between two Cu atoms on the edge, and the O atoms are slightly off the bridge sites of the same edge (Figure 4.2b). Only one configuration is considered for Cu(643) because the kink only provides an adsorption site to the Cu atom in the molecule, and the ligands remain relatively distant (Figure 4.2c).

The adsorption energy,  $E_{\text{ads}}$ , is defined by

$$E_{\text{ads}} = -(E_{\text{precursor@surf}} - E_{\text{surf}} - E_{\text{precursor}}) \quad (4.1)$$

where  $E_{\text{precursor@surf}}$  and  $E_{\text{surf}}$  are the total energies of the slab with and without  $\text{Cu}(\text{dmap})_2$ , respectively.  $E_{\text{precursor}}$  is the total energy of the  $\text{Cu}(\text{dmap})_2$  molecule in the gas phase. A positive value of  $E_{\text{ads}}$  means that the adsorption is energetically favourable compared to isolated systems. All the calculated adsorption energies  $E_{\text{ads}}$  from PBE and vdW inclusive DFT are obtained starting from the same initial structure for each adsorption configuration as shown in Figure 4.2.

Examining the electronic charge density allows further analysis of the adsorption of  $\text{Cu}(\text{dmap})_2$  on different Cu surfaces. The charge density difference due to the adsorption of  $\text{Cu}(\text{dmap})_2$  on the surface is calculated as

$$\Delta\rho = \rho_{\text{precursor@surf}} - (\rho_{\text{surf}} + \rho_{\text{precursor}}) \quad (4.2)$$

where  $\rho_{\text{precursor@surf}}$  is the electronic charge density of  $\text{Cu}(\text{dmap})_2$  adsorbed on Cu surface,  $\rho_{\text{surf}}$  is the charge density of the relaxed Cu slab in the adsorption configuration without the presence of  $\text{Cu}(\text{dmap})_2$ , and  $\rho_{\text{precursor}}$  is the charge density of

the molecule fixed in the adsorption geometry in vacuum. Bader charge analysis was performed to examine charge transfer between the molecule and the surface.[59] The theoretical scanning tunnelling microscopy (STM) images were visualized using the Hive software,[110] which implements the Tersoff-Hamann formalism.[111]

### 4.2.2 Results

Below, we present the results of  $\text{Cu}(\text{dmap})_2$  adsorption on different adsorption sites on the flat and rough surfaces of Cu using DFT with different levels of vdW treatment. In the first section, we summarize and compare the energetics and adsorption geometries for the precursor adsorbed on different adsorption sites. In the second section, through the charge density difference, we analyse how the electronic structure of the precursor/surface interface changes upon the adsorption.

#### 4.2.2.1 Adsorption Structure and Energy

**Gas Phase  $\text{Cu}(\text{dmap})_2$ .** Figure 4.1a shows the optimized structure of the precursor molecule  $\text{Cu}(\text{dmap})_2$  with pure PBE. The  $\text{Cu}(\text{dmap})_2$  molecule contains two O and two N atoms, which coordinate to the central copper atom. The Cu atom forms two rings with the ligands, which are approximately co-planar, with angles of  $\angle\text{OCuO} = 179.6^\circ$  and  $\angle\text{NCuN} = 178.3^\circ$ . The PBE computed Cu – O, Cu – N distances in  $\text{Cu}(\text{dmap})_2$  are 1.89 Å and 2.10 Å, respectively, in good agreement with the experimental values of 1.87 Å and 2.07 Å.[112] The calculated geometric parameters from PBE-D3, optB88-vdW and vdW-DF2 are slightly different from those of PBE. Figure 4.1b displays the lowest unoccupied molecular orbital (LUMO), which is of Cu:d, O:p and N:p character, consistent with  $\text{Cu}^{2+}$  as the formal oxidation state, modified by the ionocovalent ligand – Cu bonding that is visible in the occupied orbitals (not shown). As examined below, the reactivity of the molecule mostly involves the interaction of

#### 4. Precursor Adsorption on Copper Surfaces

Cu and O atoms with the surface, and the C, H, and N atoms of the dmap ligands are less reactive. The orientation of O – Cu – O bonding on the surface determines the how the molecule adsorbs (Figure 4.2).

Table 4.1. Adsorption energies ( $E_{\text{ads}}$ ) and structural parameters of  $\text{Cu}(\text{dmap})_2$  adsorbed on different adsorption sites on bare Cu(111) surface including the adsorption height  $Z_{\text{ads}}$  (Å)<sup>a</sup>, the distortion angle  $\alpha$  (°)<sup>b</sup> and the Cu – N distance in the molecule  $d_{\text{Cu-N}}$  (Å) obtained using PBE, PBE-D3, optB88-vdW and vdW-DF2 for different adsorption sites.

method	Properties	adsorption sites			
		Cu(111)-T	Cu(111)-D	Cu(111)-M	Cu(111)-B
PBE	$E_{\text{ads}}$ (eV)	0.39	1.47	0.39	0.37
	$Z_{\text{ads}}$ (Å)	3.96	2.27	4.02	4.12
	$\alpha$ (°)	8.3	39.7	7.6	5.1
	$d_{\text{Cu-N}}$ (Å)	2.05	2.55	2.04	2.04
	structure	Figure 4.3	Figure 4.4b	Figure 4.3	Figure 4.3
PBE-D3	$E_{\text{ads}}$ (eV)	3.49	3.57	3.58	3.17
	$Z_{\text{ads}}$ (Å)	2.40	2.22	2.24	2.22
	$\alpha$ (°)	36.1	36.7	37.5	35.6
	$d_{\text{Cu-N}}$ (Å)	2.34	2.33	2.40	2.27
	structure	Figure 4.4a	Figure 4.4b	Figure 4.4c	Figure 4.4d
optB88-vdW	$E_{\text{ads}}$ (eV)	2.91	3.16	3.12	1.59
	$Z_{\text{ads}}$ (Å)	2.41	2.23	2.18	3.69
	$\alpha$ (°)	38.8	38.6	39.6	8.3
	$d_{\text{Cu-N}}$ (Å)	2.45	2.44	2.58	2.04
	structure	Figure 4.4a	Figure 4.4b	Figure 4.4c	Figure 4.3
vdW-DF2	$E_{\text{ads}}$ (eV)	1.00	2.04	1.01	0.99
	$Z_{\text{ads}}$ (Å)	3.88	2.30	3.93	3.98
	$\alpha$ (°)	9.9	39.5	8.8	4.3
	$d_{\text{Cu-N}}$ (Å)	2.12	2.58	2.10	2.09
	structure	Figure 4.3	Figure 4.4b	Figure 4.3	Figure 4.3

<sup>a</sup>The adsorption height  $Z_{\text{ads}}$  is defined as the perpendicular distance between the adsorbate Cu atom and the surface Cu atoms averaged over the flat (111) surface or over the edge Cu atoms for the Cu(332) step. For Cu(643)-K,  $Z_{\text{ads}}$  is the distance between the adsorbate Cu atom and the outer kink atom on the Cu(643).

<sup>b</sup>The distortion angle  $\alpha$  is defined as  $\alpha = \frac{1}{2}(\angle \text{NCuN}(\text{gas}) - \angle \text{NCuN}(\text{adsorbed}))$ , where  $\angle \text{NCuN}(\text{gas})$  and  $\angle \text{NCuN}(\text{adsorbed})$  are the N – Cu – N angles in gas phase and adsorbed  $\text{Cu}(\text{dmap})_2$ , respectively.

**Adsorption on Flat Surface.** We investigate the adsorption of  $\text{Cu}(\text{dmap})_2$  on the Cu(111) surface for flat lying orientation. We choose four different adsorption sites, as



#### 4. Precursor Adsorption on Copper Surfaces

---

shown in Figure 4.2a. Table 4.1 displays the adsorption energies ( $E_{\text{ads}}$ ) and selected geometric parameters including adsorption height  $Z_{\text{ads}}$ , distortion angle  $\alpha$  and Cu – N bond distance  $d_{\text{Cu-N}}$  of each configuration. Figure 4.3 and Figure 4.4 show the different types of optimized geometries of  $\text{Cu}(\text{dmap})_2$  adsorption on these four sites on the Cu(111) using PBE, PBE-D3, optB88-vdW and vdW-DF2 methods.

As shown in Table 4.1, adsorption energies computed with PBE corresponding to Cu(111)-T, Cu(111)-M and Cu(111)-B vary slightly between 0.37 ~ 0.39 eV. The  $\text{Cu}(\text{dmap})_2$  molecule pushed away from the initial position on the surface after the optimization on these three adsorption sites, as shown in Figure 4.3. The distances between the adsorbate Cu atom and the surface ( $Z_{\text{ads}}$ ) are around 3.9 – 4.1 Å. The distortion angle  $\alpha$  is the change of the  $\angle \text{NCuN}$  angle after the adsorption and describes the degree of deformation of ligands around the Cu center. The distortion angles  $\alpha$  for these adsorption sites are between 5° and 8°. No chemical bonds are formed between the molecule and the surface and the gas phase structure of  $\text{Cu}(\text{dmap})_2$  is not significantly changed after the adsorption, which is indicative of physisorption.

Surprisingly, the adsorption energy computed from PBE is 1.47 eV for the Cu(111)-D, which is significantly greater than that computed for the other adsorption sites. This implies that the nature of the  $\text{Cu}(\text{dmap})_2$  adsorption is fundamentally different on the Cu(111)-D site. The optimized structure of  $\text{Cu}(\text{dmap})_2$  on Cu(111)-D (Figure 4.4b) shows that the molecule undergoes significant change relative to the gas phase in this configuration. The O atoms and Cu atom in the adsorbate bond to the surface Cu atoms and the adsorption height  $Z_{\text{ads}}$  is 2.27 Å. The bond lengths between adsorbate Cu and bonding surface Cu atoms are 2.62 Å, which is close to the computed Cu – Cu

#### 4. Precursor Adsorption on Copper Surfaces

---

bulk distance (2.56 Å). The O atom – surface distances are 2.01 Å and close to the computed Cu – O distance in bulk CuO (1.95 Å).[74] The Cu – O distance in adsorbed Cu(dmap)<sub>2</sub> is 1.91 Å which is slightly bigger than the initial gas phase distance. The bond distances and adsorption energy at Cu(111)-D are thus characteristic of chemisorption. In order to release the stress between the molecule and the surface, the Cu – N distance has significantly elongated to become 0.44 Å longer than its gas phase distance. One CH<sub>3</sub> group on each N in the dmap ligands has changed its position to the upper side of the ligands. The distortion angle of Cu(dmap)<sub>2</sub> on the Cu(111)-D is around 40°, showing that the Cu(dmap)<sub>2</sub> molecule is strongly distorted and half-decomposed upon the adsorption.

We now describe the impact of vdW forces on Cu(dmap)<sub>2</sub> adsorption on the Cu(111) surface. As listed in Table 4.1, PBE-D3 produces adsorption energies of 3.1 – 3.6 eV for all the four adsorption configurations, which are considerably greater than those of pure PBE. In the Cu(111)-T configuration (Figure 4.4a), the O – Cu – O motif of the adsorbate forms bonds with three adjacent Cu surface atoms in a row. The Cu surface atom under the adsorbate Cu atom is pushed slightly downward by 0.2 Å, while the Cu atoms that form bonds with the O atoms move slightly upward by 0.1 Å. The adsorption structure of Cu(dmap)<sub>2</sub> on Cu(111)-D obtained from PBE-D3 is similar to the structure found by pure PBE, which is shown in Figure 4.4b. The Cu(111)-M configuration (Figure 4.4c) yields a similar structure to Cu(111)-D, but the O atoms form bonds with Cu surface atoms in two neighbouring rows. In the Cu(111)-B configuration as shown in Figure 4.4d, the Cu and O atoms in the adsorbate each locate on the bridge site of the three consecutive surface Cu atoms with the Cu – Cu bond length of 2.56 Å and the O – Cu bond length of 2.06 Å. Notice the formation of triangular Cu<sub>3</sub> with the distance of 2.56–2.62 Å in all configurations. The adsorbate

#### 4. Precursor Adsorption on Copper Surfaces

---

O atoms bond with the surface Cu atoms with the distance of 2.06 Å. For all the adsorption configurations on Cu(111) from PBE-D3, the adsorption height  $Z_{\text{ads}}$  varies between 2.2 and 2.4 Å and the distortion angle  $\alpha$  is 36° – 38°. The Cu – N distance ( $d_{\text{Cu-N}}$ ) in the adsorbate is stretched by 0.16 – 0.30 Å compared to the gas phase Cu – N distance. These results show that PBE-D3 describes the Cu(dmap)<sub>2</sub> adsorption on Cu(111) surface as strong chemisorption regardless of the adsorption site.

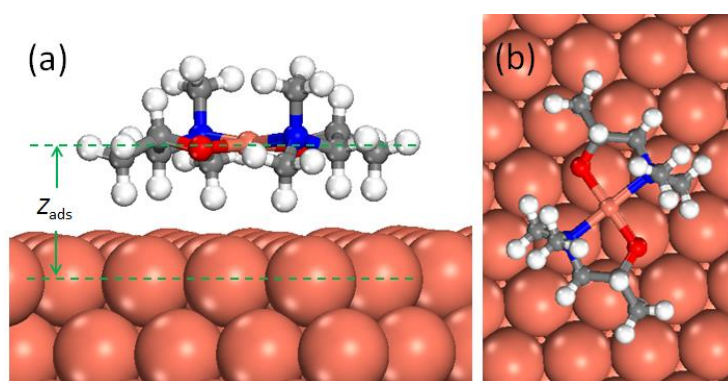


Figure 4.3. Physisorption structure of Cu(dmap)<sub>2</sub> on Cu(111) surface. (a) side view (b) top view.

As listed in Table 4.1, using optB88-vdW yields the adsorption energies  $E_{\text{ads}}$  in the range of 2.9–3.1 eV for Cu(111)-T, Cu(111)-D, Cu(111)-M configurations, which are lower than those calculated from PBE-D3, but higher than those from pure PBE. The optimized structures of Cu(111)-T, Cu(111)-D and Cu(111)-M configurations using optB88-vdW are represented in Figure 4.4a–c, respectively. The adsorption heights  $Z_{\text{ads}}$  are in the range of 2.2 – 2.4 Å, the distortion angle  $\alpha$  varies between 38°– 39° and the Cu – N distance ( $d_{\text{Cu-N}}$ ) is 0.2 – 0.4 Å longer than its gas phase distance. Thus Cu(111)-T, Cu(111)-D and Cu(111)-M configurations calculated with optB-vdW represent chemisorption. By contrast, the Cu(111)-B configuration has much lower adsorption energy of 1.59 eV with the same functional. Although this energy is higher than the adsorption energy which is calculated using pure PBE for the Cu(111)-D

#### 4. Precursor Adsorption on Copper Surfaces

configuration, no chemical bonds are formed between the adsorbate and the surface. The adsorption height of 3.69 Å and the distortion angle of 8.3° implies that optB88-vdW predicts a physisorbed structure for Cu(111)-B, but with vdW interactions contributing an extra 1.2 eV to  $E_{\text{ads}}$  relative to PBE.

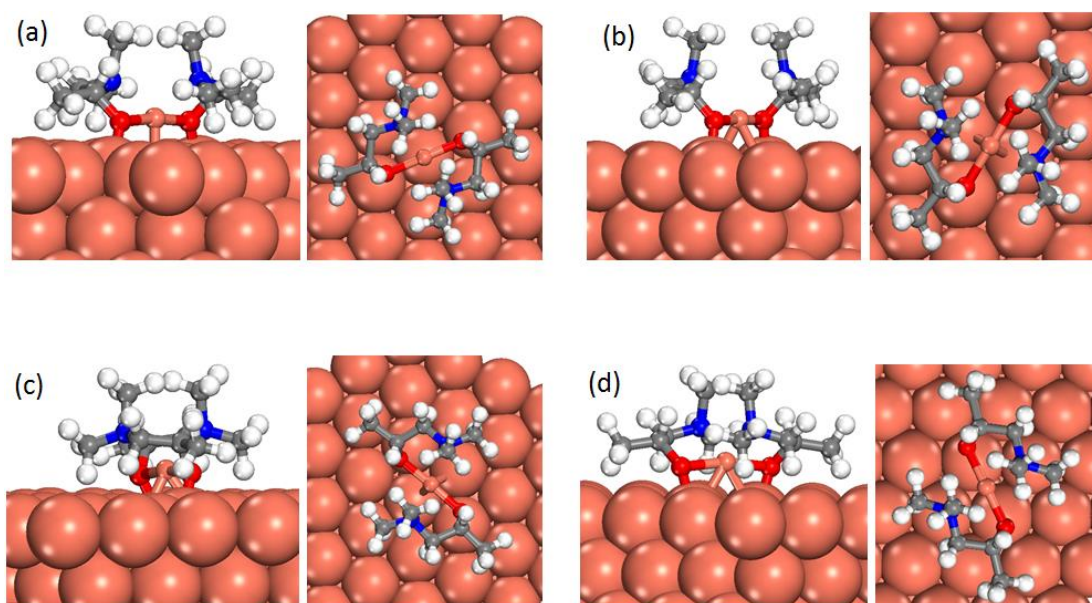


Figure 4.4. Side and top views of different adsorption structures of the  $\text{Cu}(\text{dmap})_2$  on the Cu(111) surface using DFT with and without vdW corrections (See Table 4.1 for thorough explanation). (a) Cu(111)-T. (b) Cu(111)-B (c) Cu(111)-M (d) Cu(111)-B. Only the top two Cu layers of the slab are shown for clarity.

The calculations with the vdW-DF2 functional show  $E_{\text{ads}}$  of 2.04 eV for Cu(111)-D, which is twice as great as  $E_{\text{ads}}$  of Cu(111)-T, Cu(111)-M and Cu(111)-B (Table 4.1). The optimized structures for Cu(111)-D predicted with vdW-DF2 functional are shown in Figure 4.4b. The Cu – N distances have elongated to 2.58 Å and the distortion angle  $\alpha$  is 39.5°. The vdW-DF2 functional thus predicts an additional 0.6 eV contribution from vdW attraction to the physisorption energy relative to pure PBE. The optimized structures of Cu(111)-T, Cu(111)-M and Cu(111)-B are represented in Figure 4.3. No chemical bonds are formed as the adsorption heights ( $Z_{\text{ads}}$ ) are 3.9-4.0

#### 4. Precursor Adsorption on Copper Surfaces

---

Å and the distortion angles are small ( $4^\circ - 10^\circ$ ) for these configurations. These data indicate that the adsorption mode of these structures is physisorption. It can be noticed that the PBE and vdW-DF2 both predict a chemisorbed structure on Cu(111)-D and physisorbed structures at the other three adsorption sites, although the adsorption heights of the latter are slightly shorter than those predicted with pure PBE.

The above results show that two types of adsorption mode, namely physisorption and chemisorption, exist for Cu(dmap)<sub>2</sub> on the Cu(111) surface depending on the adsorption sites and the treatment of vdW interaction. It is interesting to ask whether these adsorption modes can interconvert. We therefore investigate the transition between physisorbed and chemisorbed states and assess the potential-energy surface (PES) by performing CI-NEB calculations.[91,92] Figure 4.5 shows the pure PBE energy as a function of reaction coordinate, which is the collective change in the coordination of all the atoms in the molecule. We see that the PES is very flat near the physisorbed geometry and the transition from Cu(111)-T to Cu(111)-D proceeds with a very small energy barrier ( $E_a = 0.17$  eV for PBE), which is likely to be overcome at ALD temperatures, *e.g.* 100°C. As the vdW-DF2 functional also predicts a physisorbed structure on the Cu(111)-T site, we calculated the PES for the transition from Cu(111)-T to Cu(111)-D using the vdW-DF2 functional. We found that the vdW-DF2 method predicts that no appreciable energy barrier exists for the transition from physisorption (T) to chemisorption (D). However, here too the PES is very flat around the physisorption structure, so that such structures may exist for short lifetimes. Note that no minimum is obtained for physisorption using PBE-D3 and optB88-vdW.

## 4. Precursor Adsorption on Copper Surfaces

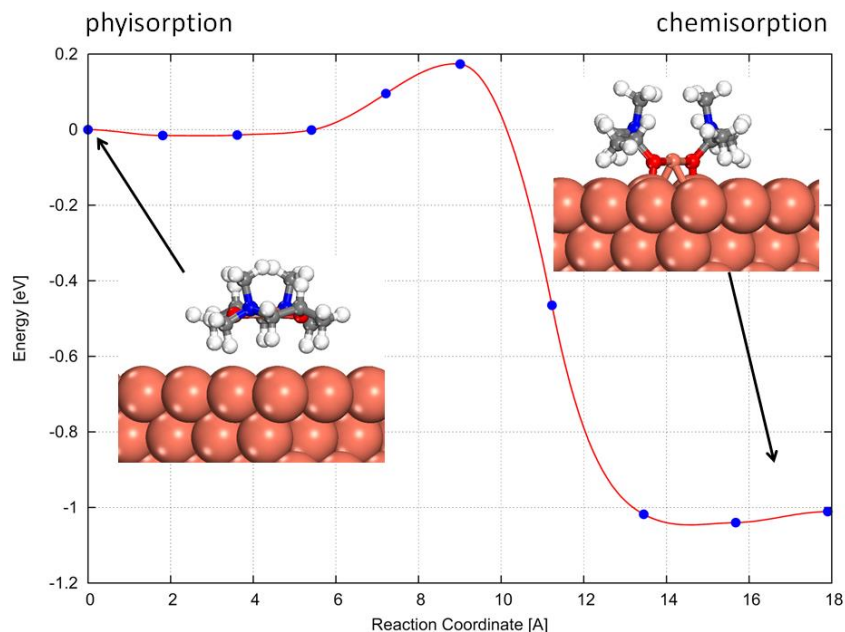


Figure 4.5. PBE reaction energy profile of transformation of  $\text{Cu}(\text{dmap})_2$  from physisorption at  $\text{Cu}(111)\text{-T}$  to chemisorption at  $\text{Cu}(111)\text{-D}$ .

**Adsorption on rough surfaces.** During the ALD growth of copper, steps and kinks are likely to form on the surfaces with various geometries. Steps and kinks are considered to be more reactive compared to flat surfaces like  $\text{Cu}(111)$  because of the under-coordinated edge and corner atoms.[113] We therefore calculate the adsorption of  $\text{Cu}(\text{dmap})_2$  on steps and kinks so as to understand the role of rough surfaces during ALD of copper. The  $\text{Cu}(332)$  step and the  $\text{Cu}(643)$  kink are chosen as the models for a rough surface in this study because they are the common steps and kinks that can be observed experimentally.[114,115] The optimized structures of adsorption on  $\text{Cu}(332)\text{-T}$  and  $\text{Cu}(643)$  are the structures from PBE calculations in Figure 4.6c-d, respectively. The adsorption energies and selected geometric parameters of those structures are displayed in Table 4.2. For the  $\text{Cu}(332)\text{-B}$  configuration, PBE, optB88 and vdW-DF2 yield a structure with adsorbate  $\text{Cu} - \text{N}$  bond elongation as shown in Figure 4.6a, while PBE-D3 predicts a structure with adsorbate  $\text{Cu} - \text{O}$  distance

#### 4. Precursor Adsorption on Copper Surfaces

---

elongated as shown in Figure 4.6b. For Cu(332)-T and Cu(643)-K configurations, all the methods with and without vdW interactions produce similar structure.

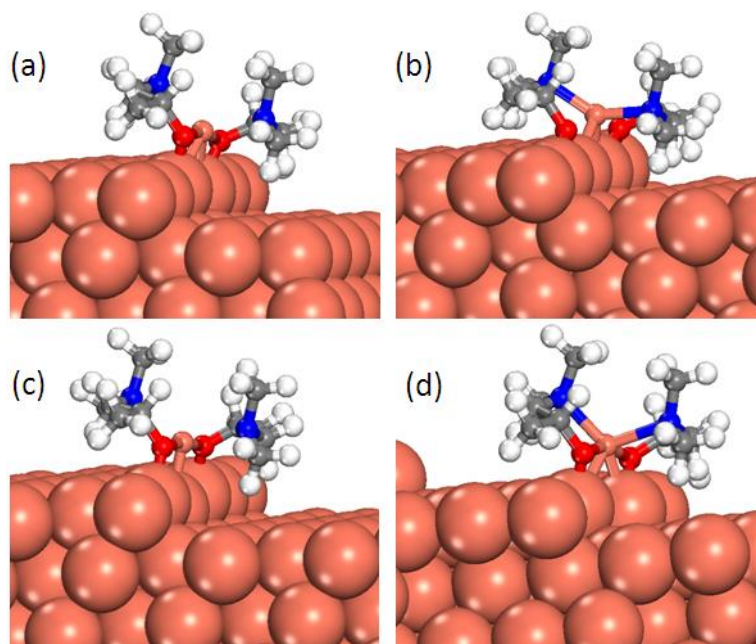


Figure 4.6. Adsorption geometry of  $\text{Cu}(\text{dmap})_2$  on rough Cu surfaces. (a) Cu(332)-B configuration obtained from PBE, optB88-vdW and vdW-DF2. (b) Cu(111)-B configuration obtained from PBE-D3. (c) Cu(332)-T and (d) Cu(643)-K from all the calculations.

PBE predicts an adsorption energy of 1.50 eV for the Cu(332)-B, which is slightly less than that of Cu(332)-T. In both structures (Figure 4.6a and c), the adsorbate O – Cu – O atoms in the  $\text{Cu}(\text{dmap})_2$  molecule form bonds with the three adjacent Cu atoms on the edge Cu atoms of the Cu(332) step. The adsorption height  $Z_{\text{ads}}$  is 2.2 Å for Cu(332)-B and 2.3 Å for Cu(332)-T. The distortion angles on Cu(332) steps are smaller than those of chemisorbed structures on Cu(111) surface by  $5^\circ - 10^\circ$ . These smaller distortion angles indicate that the molecule is less distorted at the Cu(332) steps because of the less steric hindrance between the terraces and the molecule. The bond length between adsorbate O atoms and the surface Cu atoms are around 1.99 Å ~ 2.01 Å and the bonding Cu edge atoms shift slightly upward by 0.2-0.3 Å relative to

#### 4. Precursor Adsorption on Copper Surfaces

the clean Cu(332) step. The ligands move toward the terraces and the Cu – N bonds elongate slightly to 2.27 Å.

Table 4.2. Adsorption energies ( $E_{\text{ads}}$ ) and structural parameters of  $\text{Cu}(\text{dmap})_2$  adsorbed on rough Cu surfaces including the adsorption height  $Z_{\text{ad}}$  (Å), the distortion angle  $\alpha$  ( $^\circ$ ) of  $\text{Cu}(\text{dmap})_2$  on the Cu surfaces and the Cu – N distance in the molecule  $d_{\text{Cu-N}}$  (Å) obtained using PBE, PBE-D3, optB88-vdW and vdW-DF2.

method	Property	adsorption sites		
		Cu(332)-B	Cu(332)-T	Cu(643)-K
PBE	$E_{\text{ads}}$ (eV)	1.50	1.53	1.78
	$Z_{\text{ads}}$ (Å)	2.22	2.39	2.45
	$\alpha$ ( $^\circ$ )	28.8	26.3	32.6
	$d_{\text{Cu-N}}$ (Å)	2.26	2.40	2.36
PBE-D3	$E_{\text{ads}}$ (eV)	3.63	3.44	3.59
	$Z_{\text{ads}}$ (Å)	2.09	2.37	2.40
	$\alpha$ ( $^\circ$ )	19.3	22.1	29.3
	$d_{\text{Cu-N}}$ (Å)	2.01	2.17	2.26
optB88-vdW	$E_{\text{ads}}$ (eV)	2.99	3.12	3.29
	$Z_{\text{ads}}$ (Å)	2.25	2.36	2.31
	$\alpha$ ( $^\circ$ )	26.5	27.1	31.4
	$d_{\text{Cu-N}}$ (Å)	2.20	2.23	2.32
VDW-DF2	$E_{\text{ads}}$ (eV)	2.06	2.34	2.15
	$Z_{\text{ads}}$ (Å)	2.26	2.43	2.48
	$\alpha$ ( $^\circ$ )	27.4	29.9	32.2
	$d_{\text{Cu-N}}$ (Å)	2.33	2.38	2.75

PBE-D3 calculations predict an adsorption energy of 3.6 eV for Cu(332)-B and 3.4 eV for Cu(332)-T. For the Cu(332)-B adsorption site, PBE-D3 predicts a structure with significant elongation of the adsorbate Cu – O bond, as shown in Figure 4.6b. The angle  $\alpha$  is 19°. Unlike the other structures, the Cu – N bond length has shortened by 0.1 Å from its gas phase distance and the Cu – O bonds in the adsorbate have increased significantly by 0.9 Å, with these O atoms bonding to edge Cu atoms. However, for the Cu(332)-T configuration, PBE-D3 gives a structure with Cu – N



#### 4. Precursor Adsorption on Copper Surfaces

---

bond elongation, which is similar to the Cu(332)-T structure predicted by the other methods.

We obtained  $E_{\text{ads}}$  of 3.0 eV and 2.0 eV at the Cu(332)-B step site using optB88-vdW and vdW-DF2 functionals, respectively. The optimized structures of Cu(332)-B with optB88-vdW and vdW-DF2 are again similar to the one predicted by PBE (Figure 4.6a), but with different adsorption heights and distortion angles as listed in Table 4.2. The Cu edge atom that bonds with the Cu atom in  $\text{Cu}(\text{dmap})_2$  is pushed downward by 0.2 – 0.4 Å and the Cu edge atoms that form Cu – O bonds are slightly pulled upward. The distortion angles  $\alpha$  for these structures vary between 22° and 30°, smaller than those of the configurations on the Cu(111) surface because of less steric hindrance on the vicinal surfaces. Adsorption energies obtained with optB88-vdW and vdW-DF2 for the Cu(332)-T configuration are slightly greater than that of Cu(332)-B with these methods. The adsorbate O-Cu-O atoms bond to three adjacent edge atoms with the adsorption height of 2.3-2.4 Å and distortion angle of between 22° and 30°.

In the Cu(643)-K structure, the molecule is initially located on the outer kink atom on the Cu(643) surface at an initial Cu – O distance greater than 3 Å before optimization. All the methods with and without vdW correction produce a similar optimized structure for Cu(643)-K, and thus we only show the structure from PBE calculation in Figure 4.6d. As listed in Table 4.2, the calculated  $E_{\text{ads}}$  are 1.8 eV (PBE), 2.2 eV (vdW-DF2), 3.3 eV (optB88-vdW) and 3.6 eV (PBE-D3). In this structure, the adsorption height ranges from 2.4 to 2.5 Å, depending on the functional, which is close to the Cu - Cu bulk distance. One of the O atoms bonds with the inner Cu kink atom and the other O atom bonds with the edge Cu atom neighbouring the outer kink Cu atom. The distortion angle ranges 29° ~ 33°, and the Cu – N distance  $d_{\text{Cu-N}}$  varies

#### 4. Precursor Adsorption on Copper Surfaces

---

between 2.3 and 2.6 Å. It is noteworthy that the outer Cu kink atom is significantly displaced (0.4 Å) from its bulk position in the vdW-DF2 calculations.

##### *4.2.2.2 Electronic Structure*

To further examine the interaction of  $\text{Cu}(\text{dmap})_2$  with the Cu surfaces, we analyse the electronic structure via the charge density difference (Equation 2), Bader charge and simulated STM images. We found that the 3D charge density difference plots and simulated STM images from DFT with and without additional vdW interactions are very similar for any given structure and we therefore only show the results for the Cu(111)-D, Cu(332)-T and Cu(643)-K configurations calculated with PBE.

The yellow and cyan regions in Figure 4.7 represent the electronic charge accumulations and depletions respectively between the molecule and the surface. It can be observed that the charge accumulation and depletion are mainly confined to the area between the adsorbate O – Cu – O bonds and the surface. The electron accumulation (yellow) is mainly located on the bonds between the adsorbate and surface, while the electron depletion (cyan) is located on top of the O – Cu – O atoms and the two Cu surface atoms that are attached to the O atoms. However, there is little change in the charge on C and H atoms in the ligands. This indicates that the interaction between  $\text{Cu}(\text{dmap})_2$  and the Cu surface is well localized and that the adsorption of the molecule mainly involves charge redistribution between the Cu and O atoms in the molecule and the surface. All the yellow regions are located on the molecule, indicating that the molecule gains electrons upon adsorption. The accumulation of electrons between the O atoms and the Cu surface atoms suggest that covalent bonds are formed between the O atoms and the Cu surface. The large buildup of electrons around the bonds between the adsorbate Cu and the two Cu surface atoms

#### 4. Precursor Adsorption on Copper Surfaces

---

is indicative of metallic bonding. This Cu<sub>3</sub> trimer shows a Cu-Cu(adsorbate)-Cu angle of 60.3° in the Cu(111)-D configuration. Yellow regions on the front and back of the N atoms can be observed, which indicates restoration of the N lone pair. The cyan regions and lack of yellow regions on the surface indicate that the surface donates electrons to the molecule from those surface Cu atoms that bond to the adsorbate O – Cu – O atoms.

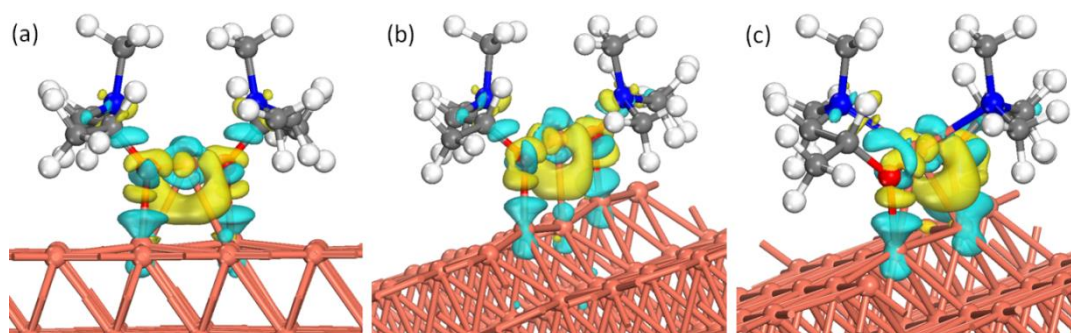


Figure 4.7. 3D isosurface of charge density differences obtained with an isovalue of  $\pm 0.001 \text{ e}/\text{\AA}^3$  of Cu(dmap)<sub>2</sub> on (a) Cu(111)-D (b) Cu(332)-B (c) Cu(643)-K obtained using PBE. Yellow and cyan regions represent the accumulation and depletion of electronic charge, respectively.

In order to quantitatively analyse the charge redistribution, we calculated the net Bader charges on the adsorbate Cu atom ( $\Delta q_{\text{Cu}}$ ) and on the molecule ( $\Delta Q$ ) relative to the Bader charge of the gas phase Cu(dmap)<sub>2</sub> molecule, as listed in Table 4.3. From Table 4.3, we can see that all the methods with and without additional vdW interaction produce the same order of  $\Delta q_{\text{Cu}}$  and  $\Delta Q$  for a given structure. This indicates that the vdW interaction has little direct effect on the electronic structures of the adsorbed Cu(dmap)<sub>2</sub> molecule on Cu surfaces. The adsorbate Cu atom gains negligible electrons ( $\Delta q_{\text{Cu}} < 0.1 \text{ e}^-$ ) in all the physisorption structures and gains  $0.2 \sim 0.4 \text{ e}^-$  in the chemisorption structures depending on the adsorption sites and calculation method. The Bader charge analysis of the physisorbed structures reveals that a fraction of an

#### 4. Precursor Adsorption on Copper Surfaces

---

electron is transferred from the molecule to the slab, where it is highly delocalised. By comparing the net charge differences for the various structures, we notice that the molecule gains electrons in all the chemisorbed structures.  $\Delta Q$  of the whole molecule in the Cu(111)-D structure is slightly greater than  $\Delta Q$  for other adsorption sites on the Cu(111) surface, which is in line with the stronger adsorption of Cu(111)-D. The electron gain of the molecule in the chemisorbed structure is consistent with what was observed in electron density difference plots (Figure 4.7) and probably originates from electron transfer to the LUMO (Figure 4.1b). Notice that  $\Delta q_{\text{Cu}}$  and  $\Delta Q$  of the Cu(332)-B structure predicted by PBE-D3 is significantly greater than those of other structures because of the breaking of the Cu – O bonds.

Table 4.3. Calculated change in Bader electronic charge (units of  $e^-$ ) of adsorbate Cu atom ( $\Delta q_{\text{Cu}}$ ) and Cu(dmap)<sub>2</sub> molecule ( $\Delta Q$ ) upon the adsorption of Cu(dmap)<sub>2</sub> on Cu surfaces relative to the Bader charge of the gas phase molecule.

	PBE		PBE-D3		optB88-vdw		VDW-DF2	
	$\Delta q_{\text{Cu}}$	$\Delta Q$	$\Delta q_{\text{Cu}}$	$\Delta Q$	$\Delta q_{\text{Cu}}$	$\Delta Q$	$\Delta q_{\text{Cu}}$	$\Delta Q$
Cu(111)-T	-0.08	-0.28	0.21	0.30	0.20	0.32	-0.02	0.20
Cu(111)-D	0.25	0.34	0.23	0.31	0.24	0.32	0.26	0.39
Cu(111)-M	-0.07	-0.29	0.26	0.36	0.23	0.35	-0.04	-0.18
Cu(111)-B	-0.07	-0.31	0.23	0.31	-0.06	-0.29	-0.03	-0.18
Cu(332)-B	0.22	0.32	0.45	0.58	0.22	0.34	0.23	0.36
Cu(332)-T	0.20	0.33	0.18	0.28	0.19	0.32	0.23	0.39
Cu(643)-K	0.22	0.31	0.26	0.36	0.22	0.34	0.24	0.37

The methods we used in this work produce a range of adsorption energies and different adsorption structures. No experimental data exist at present against which the calculations can be validated in order to determine the best method. We therefore simulate theoretical STM images of the chemisorbed structures as a route towards validation in future experimental work. Figure 4.8 depicts the simulated STM images of Cu(111)-D, Cu(332)-B and Cu(643)-K configurations calculated with PBE. In these

## 4. Precursor Adsorption on Copper Surfaces

---

STM images, the adsorbate Cu and O atoms are located in the darker part, which indicates that Cu and O atoms are close to the surface and far from the STM tip. We showed the atomic positions of adsorbate Cu (green) and O (red) in the right half of the STM images. The brightest regions of the STM images of the Cu(111)-D structure correspond to the methyl groups in the ligand, which face upward. Since the two ligands of the molecule are inclined at the rough surfaces, the brightness of upper parts of the STM images of Cu(332)-B and Cu(643)-K differ slightly.

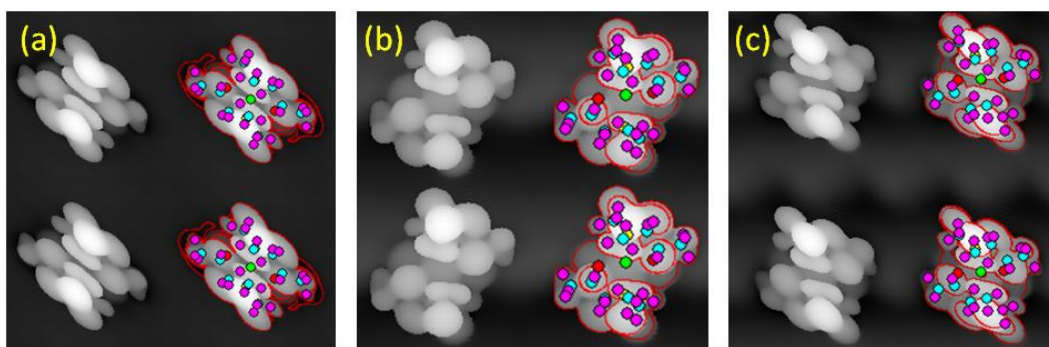


Figure 4.8. Simulated STM images of  $\text{Cu}(\text{dmap})_2$  adsorbed on (a) Cu(111)-D (b) Cu(332)-B (c) Cu(643)-K with bias voltage  $V = 1.5$  eV and tip distance  $d = 1.5$  Å. Contours are added on the right to guide the eye. The circles inside the contours show the positions of atoms in  $\text{Cu}(\text{dmap})_2$ : green, Cu; yellow, N; red, O; aqua, C; pink, H.

### 4.2.3 Discussion

Now we discuss the results of the  $\text{Cu}(\text{dmap})_2$  adsorption on different adsorption sites. First we analyse the geometric and electronic features of physisorption and chemisorption structures obtained by DFT with different levels of vdW treatment. Then we compare and assess the performance of these vdW treatments. Finally we discuss how the Cu atom in the  $\text{Cu}(\text{dmap})_2$  molecule is reduced during adsorption and the implications for Cu ALD processes.

**Physisorption vs. chemisorption structure.** The results show that the  $\text{Cu}(\text{dmap})_2$  molecule chemisorbs or physisorbs depending on the stereoselective environment on the  $\text{Cu}(111)$  surface. From the adsorption energy and structural changes in  $\text{Cu}(\text{dmap})_2$  calculated with PBE, we can see that  $\text{Cu}(\text{dmap})_2$  chemisorbs on the  $\text{Cu}(111)\text{-D}$  site and physisorbs on the other sites including  $\text{Cu}(111)\text{-T}$ ,  $\text{Cu}(111)\text{-M}$  and  $\text{Cu}(111)\text{-B}$ . In order to explain this site-selective chemisorption on  $\text{Cu}(111)\text{-D}$ , one needs to look at its adsorption structure. The  $\text{Cu}(111)\text{-D}$  configuration allows the molecule to approach the surface with the shortest O–surface distance and with less steric hindrance between the ligands and the surface, which is not the case in the other structures. From the charge density difference plot, we can see that the strong ionocovalent bonds between O and surface Cu atoms hold the molecule attached to the surface and apparently overcome the Pauli repulsion forces and energetic cost of breaking Cu–N bonds. However, on the other three configurations on  $\text{Cu}(111)$ , Cu–N bonds are not broken and Cu–O bonds are not formed because the O-surface distance is not short enough in the starting configurations. For the rough surfaces, it is predicted that the molecule chemisorbed onto the  $\text{Cu}(332)$  step and  $\text{Cu}(643)$  kink in all our calculations.

The geometric features of physisorbed  $\text{Cu}(\text{dmap})_2$  (Figure 4.3) include the long adsorbate-surface distance (approximately 4.0 Å) and the small distortion angle ( $\alpha < 9^\circ$ ). The molecule undergoes only slight distortion and the Cu atom keeps its position in the planar coordination. Physisorption is characterized by a smaller adsorption energy ( $E_{\text{ads}} = 0.4$  eV) for PBE, but of the order of 1.0 eV for the vdW-DF2 calculation.

On the other hand, chemisorption involves relatively high adsorption energy both with and without additional vdW interactions in DFT. These high adsorption energies

#### 4. Precursor Adsorption on Copper Surfaces

---

are the net result of bond formation between the adsorbate O – Cu – O motif and the surface Cu atoms tempered by distortion. The new bonding causes an accumulation of stress between the precursor and surface that is generally released in the form of Cu – N breaking and the distortion of the rest of the ligands. The distortion of Cu(dmap)<sub>2</sub> can be characterized in the following ways. (i) The adsorbate Cu atom loses its position in the planar structure and obtains a linear structure in the O – Cu – O motif bonded with the surface. (ii) The Cu – N distances are elongated significantly by 0.2 to 0.5 Å (except for the Cu(332)-B structure with PBE-D3), but N remains oriented towards the Cu center. (iii) The Cu adsorption height  $Z_{\text{ads}}$  is comparable to the Cu – Cu bulk distance and the accumulation of charge between multiple Cu atoms is consistent with metallic bonding. (iv) The distortion angle  $\alpha$  is greater than 26° (flat surface) and 19° (rough surface) and correlated with the Cu – N distance. The chemisorbed Cu(dmap)<sub>2</sub> molecule accepts electron density from the surface and the charge transfer mainly occurs in the region between adsorbate O – Cu – O bonds and the surface.

**The impact of different levels of vdW treatment.** The calculations with different levels of vdW treatment give different adsorption energies and optimized structures. Pure PBE predicts that Cu(dmap)<sub>2</sub> chemisorbs on Cu(111)-D and physisorbs on Cu(111)-T, Cu(111)-B, Cu(111)-M. The vdW-DF2 functional also predicts chemisorption at Cu(111)-D and physisorption at Cu(111)-T, Cu(111)-B and Cu(111)-M, but with  $E_{\text{ads}}$  nearly 0.6 eV greater. PBE–D3 predicts chemisorption for all configurations, with the higher adsorption energies that are 2 eV greater than those obtained from pure PBE. The optB88-vdW method yields chemisorption on the three sites Cu(111)-T, Cu(111)-B and Cu(111)-M sites and physisorption on Cu(111)-B. This indicates that the vdW interactions act not only to increase the adsorption energies, but also to fundamentally change the nature of the adsorption.

#### 4. Precursor Adsorption on Copper Surfaces

---

It is reported that semi-empirical dispersion corrections (PBE-D) overestimate the adsorption energies for other organic/metal interactions.[116] This overestimation comes from the neglect of screening of dispersive interactions by the subsurface copper atoms. The adsorption energies of 3.2-3.5 eV predicted here by PBE-D3 are therefore most probably overestimated and thus represent the maximum limit. Although optB88-vdW predicts chemisorbed structures on three out of four configurations, the optB88-vdW energies for chemisorption are smaller than those of PBE-D3. The adsorption energy of chemisorbed Cu(111)-D from vdW-DF2 is less than that of PBE-D3 and optB88-vdW by 2.0 eV. The relative order of adsorption energies for Cu(dmap)<sub>2</sub> on Cu surfaces is  $E_{\text{ads}}(\text{PBE-D3}) > E_{\text{ads}}(\text{optB88-vdW}) > E_{\text{ads}}(\text{vdW-DF2}) > E_{\text{ads}}(\text{PBE})$ . This is the same order as was obtained for benzene/metal interactions.[98,100] The difference between adsorption energy on rough surfaces are less dramatic, but they are in the same order as those of Cu(111). Thus we believe that optB88-vdW is the most suitable one of these methods for describing Cu(dmap)<sub>2</sub> adsorption on the Cu surfaces.

Our results from the charge density difference and Bader charge analysis show that the choice of vdW inclusive method has no significant impact on the electronic structure of the Cu(dmap)<sub>2</sub> adsorbate on Cu surfaces. For chemisorbed Cu(dmap)<sub>2</sub> on a certain adsorption site, all the methods predict similar electronic structures. Experimental STM study of Cu(dmap)<sub>2</sub> adsorption on the Cu surface could complement this study and validate the methods we used. If very ordered Cu(dmap)<sub>2</sub> molecules oriented solely at 120° to each other were observed on the Cu(111) surface, the vdW-DF2 or pure PBE methods could be correct, as shown in Figure 4.8a. In the same manner, more disordered Cu(dmap)<sub>2</sub> structures on this Cu surface could indicate



#### 4. Precursor Adsorption on Copper Surfaces

---

that the PBE-D3 or optB88-vdW methods correctly describe  $\text{Cu}(\text{dmap})_2$  chemisorption in almost any orientation.

**Implication for Cu ALD.** In a Cu ALD experiment, the substrate was saturated with  $\text{Cu}(\text{dmap})_2$  when the pulse time exceeded 2.0 s and this gave a growth rate of 0.2 Å/cycle.[12] An indirect ALD experiment with  $\text{Cu}(\text{dmap})_2$  pulse time longer than 3.0 s afforded a growth rate of 0.50 Å/cycle.[22] In ALD, the precursor molecules should chemisorb strongly on the substrate and react with the co-reagent through surface diffusion. If however the precursor is merely physisorbed on the substrate, reaction of the Cu center with the co-reagent may not be possible because distortion in the structure of physisorbed precursors is very slight and the Cu center is not accessible. The adsorption sites of chemisorbed precursors thus determine the initial position of ALD reactions within the desired monolayer of adsorbates. Regardless of vdW functional, we find that the precursors chemisorb easily with less steric hindrance on rough surfaces such as Cu(332) steps and Cu(643) kinks. Nevertheless, the chemisorption energies on the smooth Cu(111) surface are of the same magnitude (with any given method) and thus, the ALD reactions may take place on both smooth and rough parts of the growing Cu surface simultaneously.

The significant elongation of Cu – N during adsorption indicates that the Cu – N bond breaks in the early stage of ALD reaction cycle as the Cu centre gains electrons and is reduced. As a result, the ligands become unstable and the precursor becomes more reactive to the co-reagent. The breaking of the Cu – O bond in the Cu(332)-B configuration of the PBE-D3 calculation illustrates that the Cu – O bond may also break. These indications show that breaking ligand – Cu bonds is energetically more favourable than the breaking of C – C, C – N, C – O and C – H bonds in the ligand

#### 4. Precursor Adsorption on Copper Surfaces

---

that might lead to C or N impurities, or to deposition of copper oxide. This indicates that the dmap ligand acts as a unit during the ALD of Cu and is an “innocent” ligand that does not participate in the redox reaction. The tendency toward ligand – Cu bond breaking in  $\text{Cu}(\text{dmap})_2$  may partially explain the success of low temperature ALD of Cu with this molecule. Clean cleavage of the ligand – metal bond is one of the requirements for selecting precursors for ALD of metals.

The Bader charge analysis shows that the Cu atom in the molecule gains 0.2 to 0.4 electrons from the surface on chemisorption, which indicates that the adsorbate Cu atom is partially reduced. We recognise that DFT has systematic errors in the distribution of charge in metal d states. Nevertheless, some reduction of the adsorbate Cu atom should accompany metallic bonding to the surface. This leads to the loss of the precursor’s square planar structure and to the linear O – Cu – O motif that attaches to the surface. In order to deposit the Cu metal atom from  $\text{Cu}(\text{dmap})_2$ , the adsorbed Cu atom should eventually be reduced to  $\text{Cu}^0$  and the ligands should be removed from the surface to pave the way for the next ALD cycle. This is achieved with the reducing agent  $\text{Et}_2\text{Zn}$  in direct ALD[12] and with formic acid and hydrazine in 3-step ALD.[22] Understanding the adsorption of  $\text{Cu}(\text{dmap})_2$  on the surface provides a base to study the full reaction mechanisms between the reducing agent and the adsorbed precursor, which we will address in chapter 5.

### **4.3 $\text{Cu}(\text{acac})_2$ adsorption on Cu(111) surface**

Metal acetylacetonates are frequently used as the precursor for metal ALD and CVD processes.[117–120] Copper(II) acetylacetonate [ $\text{Cu}(\text{acac})_2$ ] has been mainly used in plasma assisted ALD processes to deposit metallic copper and copper oxide, as shown in Table 1.1 (page 6). For instance, Wu et al. deposited copper thin film on Ru

#### 4. Precursor Adsorption on Copper Surfaces

---

substrate using  $\text{Cu}(\text{acac})_2$  and  $\text{H}_2$  plasma.[121] Thermal ALD of copper using  $\text{Cu}(\text{acac})_2$  has also been reported with a three-step process which involves the deposition of the corresponding metal oxide and its reduction to a metal.[16]  $\text{Cu}(\text{II})$  oxide has also been deposited with  $\text{Cu}(\text{acac})_2$  and ozone ( $\text{O}_3$ ) in a temperature window of 150 °C to 230 °C with a growth rate of 0.38 Å/cycle.[122]

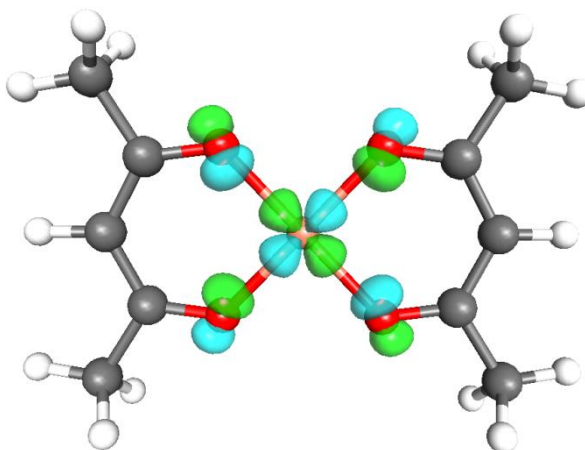


Figure 4.9. Optimized structure of copper(II) acetylacetonate [ $\text{Cu}(\text{acac})_2$ ] with the lowest unoccupied molecular orbital (LUMO) displayed. Color scheme: red=O, salmon pink=Cu, grey=C, and white=H.

In this section, we study the adsorption of  $\text{Cu}(\text{acac})_2$  on a  $\text{Cu}(111)$  surface. First we present and discuss the energetics and geometric structures of  $\text{Cu}(\text{acac})_2$  adsorbed on several adsorption sites on the  $\text{Cu}(111)$  surface. Second, we shed light on the factors that explain the deposition of copper oxide or metallic copper from  $\text{Cu}(\text{acac})_2$  by analysing the adsorption geometry and charge distribution. Third, we compare the adsorption behaviour of  $\text{Cu}(\text{acac})_2$  with that of  $\text{Cu}(\text{dmap})_2$  which is studied in detail in section 4.2. We briefly discuss what makes a good Cu ALD precursor from the initial adsorption of the precursors. In the top site configuration, the adsorbate Cu atom of  $\text{Cu}(\text{acac})_2$  aligns with the top of a Cu surface atom and the O atoms are slightly off the top of Cu atoms of one surface row.

#### 4. Precursor Adsorption on Copper Surfaces

---

In the previous section, we studied the adsorption of  $\text{Cu}(\text{dmap})_2$  on flat and rough Cu surfaces using pure PBE, PBE-D3, vdW-optB88 and vdW-DF2 methods. We concluded that the vdW-optB88 functional is one of the most suitable methods for describing the vdW interactions at a precursor/substrate interface. Therefore we use pure PBE and vdW-optB88 method to study the adsorption of  $\text{Cu}(\text{acac})_2$  on a Cu(111) surface. We use the same computational setups that were used for  $\text{Cu}(\text{dmap})_2$  adsorption on Cu(111) surface.

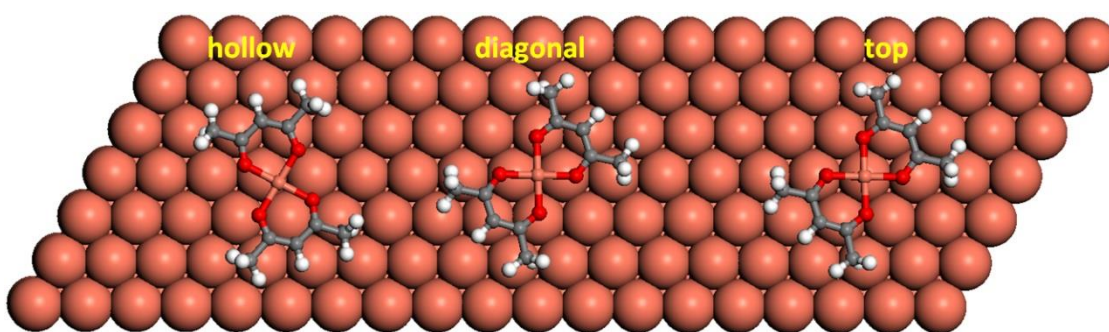


Figure 4.10. Models for the  $\text{Cu}(\text{acac})_2$  adsorption on a Cu(111) surface. Three different adsorption sites, namely hollow, diagonal and top sites, are considered. Salmon pink, red, grey and white spheres represent Cu, O, C and H atoms, respectively.

As we understand from the previous section, adsorption energy and adsorption geometry are site-selective. Therefore we choose three adsorption sites for  $\text{Cu}(\text{acac})_2$  adsorption on the Cu(111) surface: hollow, diagonal and top sites, as shown in Figure 4.10. In the hollow configuration, the adsorbate Cu atom is located on the hollow site of the surface, and the two O atoms are located in bridge sites. In the diagonal configuration, one of the O – Cu – O bonds aligns with the long diagonal of four neighbouring Cu atoms. In the top configuration, two O atoms align on the top of two Cu surface atoms and the adsorbate Cu atom is at a bridge site.

#### 4. Precursor Adsorption on Copper Surfaces

---

The adsorption energies ( $E_{\text{ads}}$ ), the adsorption height ( $Z_{\text{ads}}$ ), the Cu – O distance ( $d_{\text{Cu-O}}$ ) and the distance between C, the surface ( $d_{\text{C-surf}}$ ) and the net Bader charge on the adsorbate Cu ( $\Delta q_{\text{Cu}}$ ) are given in

Table 4.4. With pure PBE, the adsorption energy of -0.48 eV is obtained for the diagonal configuration, which is greater than the adsorption energies of hollow and top configurations by 0.12 eV. The adsorption height in the diagonal configuration is 2.22 Å, which is significantly smaller than the adsorption heights in the hollow and top configurations. The net Bader charge change ( $\Delta q_{\text{Cu}}$ ) on the adsorbate Cu atom in the diagonal configuration is also 0.26 e<sup>-</sup>, while  $\Delta q_{\text{Cu}}$  is about zero in the hollow and top configurations. It is obvious from these findings and the optimized structures in Figure 4.11a-c and the 3D charge density plots in Figure 4.12a-c that the Cu(acac)<sub>2</sub> molecule is chemisorbed in the diagonal configurations and physisorbed in the hollow and top configurations for PBE.

Table 4.4. Calculated adsorption energies and selected structural parameters of Cu(acac)<sub>2</sub> adsorption on Cu(111) surface using PBE and optB88-vdW methods.

	$E_{\text{ads}}$ (eV)	$Z_{\text{ads}}$ (Å)	$d_{\text{C-surf}}$ (Å)	$\Delta q_{\text{Cu}}$ (e <sup>-</sup> )
PBE				
diagonal	-0.48	2.22	2.24	0.26
hollow	-0.36	3.20	3.52	0.00
top	-0.36	3.17	3.56	0.01
OptB88-vdW				
diagonal	-2.12	2.21	2.26	0.28
hollow	-1.77	2.55	3.12	0.20
top	-1.86	2.52	3.11	0.19

<sup>a</sup>The adsorption height  $Z_{\text{ads}}$  is defined as the perpendicular distance between the adsorbate Cu atom and the surface Cu atoms averaged over the flat (111) surface.  $d_{\text{Cu-O}}$  is the bond lengths of adsorbate Cu and O atoms.  $d_{\text{C-surf}}$  (Å) is the distance between adsorbate C and the nearest surface Cu atom.

#### 4. Precursor Adsorption on Copper Surfaces

---

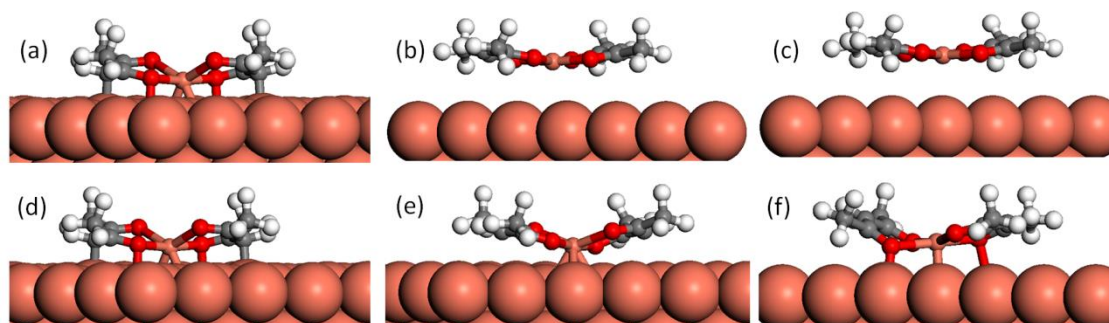


Figure 4.11. Optimized Structures of  $\text{Cu}(\text{acac})_2$  adsorbed on  $\text{Cu}(111)$  surface calculated with PBE (a–c) and vdW-optB88 method (d–f). Structures (a) and (c) are for diagonal, (b) and (e) are for hollow and (c) and (f) are for top configurations.

Contrary to pure PBE, the vdW-optB88 functional predicts chemisorption in all three configurations (Figure 4.11d-f). The adsorption energy of the  $\text{Cu}(\text{acac})_2$  molecule in the diagonal configuration is -2.12 eV, which is about 0.3 eV greater than the adsorption energies of the  $\text{Cu}(\text{acac})_2$  adsorbed in the hollow and top configurations. The adsorption height in the diagonal site is 2.21 Å, very close to that predicted with pure PBE. The adsorption heights  $Z_{\text{ads}}$  in the hollow and top structures are 2.55 and 2.52 Å, which are in line with the weaker adsorption energies. The net adsorbate Cu atom Bader charge in the diagonal site is 0.28 eV, slightly greater than the  $\Delta q_{\text{Cu}}$  values in top and hollow structures, all indicative of partial reduction of Cu on chemisorption.

As we can see from optimized structures of diagonal configurations, which has the highest adsorption energies both from pure PBE and vdW-optB88 functional, two of the adsorbate C atoms form a bond with the surface. The C atom and the surface distances are 2.24 and 2.26 Å with the surface Cu atom pulled up slightly, indicating the Cu – C bond formation. This is also evident from the charge density difference plots in Figure 4.12a and d, the surface Cu and C atoms lose electrons (yellow) to form

#### 4. Precursor Adsorption on Copper Surfaces

---

bonds (green regions) between the Cu and C atoms. As we will see in the next chapter, the breaking of Cu – C bond needs very high activation energies. Thus the chemisorbed  $\text{Cu}(\text{acac})_2$  molecule in the diagonal configuration may decompose through the scission of the C – O bonds and retention of Cu–O bonds. This would lead to the deposition of CuO or  $\text{Cu}_2\text{O}$  rather than Cu metal. Thus, the formation of C and surface bonding when the Cu precursor adsorbs on the surface is detrimental to the Cu ALD, as it leads to the decomposition of the ligands.

In conclusion, we studied the adsorption of the  $\text{Cu}(\text{acac})_2$  molecule on the Cu(111) surface with pure PBE and vdW-optB88. The chemisorbed structure is predicted for the diagonal structure with pure PBE and for all three configurations with vdW-optB88 method. The adsorption energies and net adsorbate Bader charge are slightly greater in the diagonal configurations in both methods. The bonding between the carbon atom and the surface in the diagonal configurations may lead to the reaction pathways for the deposition of copper oxides rather than copper metal.

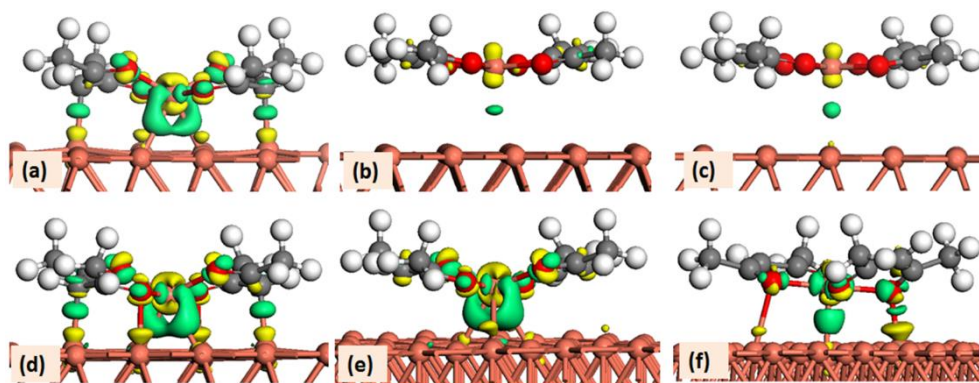


Figure 4.12. 3D isosurface of charge density differences obtained with an isovalue of  $\pm 0.001 \text{ e}/\text{\AA}^3$  of  $\text{Cu}(\text{acac})_2$  on Cu surfaces using PBE (a-c) and vdW-optB88 (d-f). Green and yellow regions represent the accumulation and depletion of electronic charge, respectively.

### 4.4 Conclusions

In conclusion, we studied the adsorption of the  $\text{Cu}(\text{dmap})_2$  molecule on different sites on flat and rough Cu surfaces using DFT with various levels of treatment of vdW forces. It is found that the vdW forces are crucial to describe the precursor – substrate interaction. The relative order of computed adsorption energies for  $\text{Cu}(\text{dmap})_2$  on Cu surfaces is  $E_{\text{ads}}(\text{PBE-D3}) > E_{\text{ads}}(\text{optB88-vdW}) > E_{\text{ads}}(\text{vdW-DF2}) > E_{\text{ads}}(\text{PBE})$ . We find that the pure PBE and the vdW-DF2 methods yield  $\text{Cu}(\text{dmap})_2$  chemisorbed selectively at one Cu(111) surface site, while the PBE-D3 method yields chemisorbed structures on Cu(111) at all adsorption sites. The vdW-optB88 functional predicts a chemisorbed structure for three out of four adsorption sites and physisorption for one site, with a relatively large energy for physisorption. For the rough surfaces, all the methods with and without additional vdW forces predict that the molecule chemisorbs on the Cu(332) step and Cu(643) kink.

The absence of Cu – C bonds and the breaking of Cu – N or Cu – O bonds as  $\text{Cu}(\text{dmap})_2$  chemisorbs shows that metal – ligand bonding is broken cleanly during the early stage of Cu ALD, making the molecule reactive to the co-reagent in Cu ALD reactions without unwanted impurities of C, H, O or N. Charge redistribution occurred between the O – Cu – O unit of the molecule and the Cu surface. Bader charge analysis shows that the molecule gains electrons in the chemisorbed structures, with the Cu centre in particular being partially reduced.

We also studied the adsorption of the  $\text{Cu}(\text{acac})_2$  molecule, which is used for deposition of metallic Cu and copper oxides, on the Cu(111) surface. Through considering several adsorption sites, a chemisorbed structure is predicted for the diagonal site with pure PBE and for all three configurations with vdW-optB88. The bonding between



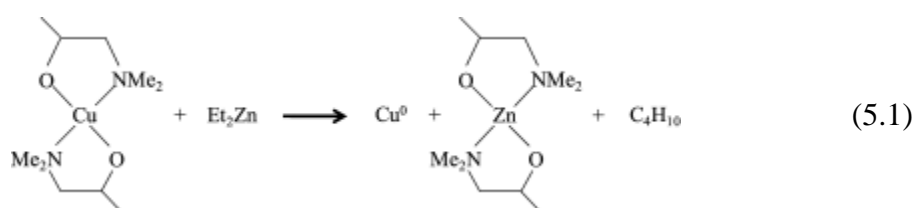
#### 4. Precursor Adsorption on Copper Surfaces

---

carbon atom and the surface in the diagonal configuration may lead to the reaction pathways for the deposition of copper oxides.

## 5 Surface Chemistry of Cu ALD by Transmetalation

In Chapter 4, we studied the adsorption of Copper dimethylamino-2-propoxide [Cu(dmap)<sub>2</sub>] on Cu surfaces. In this chapter, we use periodic DFT method to study the surface reaction of Cu(dmap)<sub>2</sub> and diethylzinc (Et<sub>2</sub>Zn, Et = C<sub>2</sub>H<sub>5</sub>) to understand the reaction mechanism of the low temperature ALD of Cu reported by Lee *et al.* [12], as this experimental work achieved low temperature Cu ALD using a novel precursor and co-reagent concept. In the work done by Lee *et al.*, a uniform, conformal, pure copper metal thin film was deposited through a new ALD process using the reaction of Cu(dmap)<sub>2</sub> and Et<sub>2</sub>Zn,



Lately, low temperature ALD of copper was achieved using Cu(dmap)<sub>2</sub> but with other co-reagents.[22,23] Although the ALD mechanisms of metal oxides are well understood,[37,40,123] very few theoretical works were dedicated to understand the reaction mechanisms of copper and other metals.[79,124] Dey *et al.* used a gas phase model to study the reactions of several common Cu precursors with Et<sub>2</sub>Zn.[79] However, since ALD is based on self-terminating surface reactions, it is necessary to understand the role of the surface. This chapter deal with the reaction pathways and energetics for a full cycle of Cu ALD, including the adsorption/dissociation of Cu(dmap)<sub>2</sub>, adsorption/decomposition of (C<sub>2</sub>H<sub>5</sub>)<sub>2</sub>Zn, ligand diffusion by-product

formation and desorption. Finally we determine the reaction mechanism of Cu ALD based on our calculation.

### 5.1 Computational method

All calculations were performed using the Vienna Ab Initio Simulation Package (VASP).[85,125] Projector augmented wave (PAW)[86] potentials were used to represent the effective cores. Electronic optimization was performed self-consistently using the plane wave basis set with a cutoff energy of 450 eV. The Perdew–Burke–Ernzerhof (PBE)[46] functional was used to describe exchange and correlation effects. The Cu(111) surface was modelled with p (6 × 6) surface unit cells and four–layer slabs separated by 18 Å of vacuum and a precursor coverage of one Cu(dmap)<sub>2</sub> per 2 nm<sup>2</sup> (cell volume = 4.99 nm<sup>3</sup>), following our previous study in Chapter 4. All atoms in the slab were allowed to relax, and the systems were considered to be fully optimized when the forces on each ion were smaller than 0.02 eV/Å.

The minimum energy pathways (MEP) were investigated using the climbing image nudged elastic band method (CI-NEB) to determine the transition state (TS) structure.[91,92] For both reactant and product of a certain reaction, we perform geometry optimization to identify the minimum energy configurations which are used to generate a number of initial images along the MEP using linear interpolation. The atomic structures were relaxed using the quasi-Newton scheme as the CI-NEB method requires a force–based optimizer. Ten images were introduced for each reaction. The reaction was divided into two separate reactions if an intermediate minimum was found. The forward reaction rate can be calculated from,

$$k = \left[ \frac{k_B T}{h} \exp\left(\frac{\Delta S^\ddagger}{R}\right) \right] \exp\left(\frac{-E_a}{RT}\right) \quad (5.2)$$

where  $k_B$  and  $h$  are Boltzmann's and Planck's constants, respectively.  $\Delta S^\ddagger$ , the entropy of activation, is the standard molar change of entropy when the activated complex is formed from reactants and  $E_a$  is the activation energy.  $T$  is the temperature in Kelvin. We consider low activation barriers  $E_a$  of less than 1 eV, which is accessible at ALD temperatures of around 500 K.[40]

## 5.2 Results

This ALD process of Cu consists of pulses of precursor  $\text{Cu}(\text{dmap})_2$  and co-reagent  $\text{Et}_2\text{Zn}$ , separated by purges. Thus, we postulate the reaction pathways based on our calculations and divide the reaction pathways into two sections, namely, (i) adsorption and decomposition of  $\text{Cu}(\text{dmap})_2$  on  $\text{Cu}(111)$  surface and (ii) adsorption and decomposition of  $\text{Et}_2\text{Zn}$  on the  $\text{Cu}(111)$  surface covered with  $\text{Cu}(\text{dmap})_2$  fragments and by-product formation. Table 5.1 lists the calculated activation barrier ( $E_a$ ) and the reaction energy ( $\Delta E$ ) for the possible reactions of  $\text{Cu}(\text{dmap})_2$  and  $\text{Et}_2\text{Zn}$  on the  $\text{Cu}(111)$  surface. The steps in this cyclic process are labelled with capital letters from 'A' to 'G'. In the following sections, we separately present our results on each of these steps and discuss these reactions in order to understand the overall reaction mechanism of Cu ALD.

### 5.2.1 First half reaction: adsorption and decomposition of $\text{Cu}(\text{dmap})_2$ on $\text{Cu}(111)$ surface.

In the previous chapter, we studied the adsorption of  $\text{Cu}(\text{dmap})_2$  on a number of adsorption sites on flat and rough Cu surfaces using different levels of treatment of

## 5. Surface Chemistry of Cu ALD by Transmetalation

vdW interactions. We found that pure PBE predicts that physisorbed and chemisorbed structures exist on Cu(111) surface depending on the adsorption sites. Now we discuss the possible reaction pathways of the decomposition of Cu(dmap)<sub>2</sub> and its reaction with Et<sub>2</sub>Zn molecule on the Cu(111). Figure 5.1 shows the reaction energy pathways of the first half part of the Cu ALD reaction, which consists of adsorption and decomposition of Cu(dmap)<sub>2</sub> represented with step A and step B respectively.

Table 5.1. The calculated activation barrier ( $E_a$ ) and reaction energies ( $\Delta E$ ) for possible reactions for depositing Cu from Cu(dmap)<sub>2</sub> and Et<sub>2</sub>Zn through ALD. Capital letters 'A' to 'G' represent following steps: A is adsorption of Cu(dmap)<sub>2</sub>, B is decomposition of Cu(dmap)<sub>2</sub>, C is adsorption of Et<sub>2</sub>Zn on the dmap-covered surface, D is the ethyl group migration, E is ligand diffusion, F is ligand re-ordering, G is Zn(dmap)<sub>2</sub>/butane formation. The capital letters with numbers represent different configurations. The configurations with  $E_a$  less than 1.0 eV are shown in the following figures.

reactions	$E_a$ (eV)	$\Delta E$ (eV)	explanation
First half reaction			
1. A1→A2	0.17	-1.01	Physisorption to chemisorption transition
2. A2→B1	0.44	-0.11	One Cu–O bond scission (Cudmap+dmap)
3. A2→B2	0.58	-0.01	double Cu–O bond scission (dmap+Cu+dmap)
4. A2→B3	1.56	0.26	The O–C bond scission
5. A2→B4	1.92	0.90	The C–C bond scission
6. A2→B5	2.59	0.73	The C–N bond scission
Second half reaction			
7. B1→C1		-0.03	Et <sub>2</sub> Zn adsorption on Cudmap+dmap
8. B2→C2		0.01	Et <sub>2</sub> Zn adsorption on dmap+ Cu + dmap
9. C1→D1	0.78	-2.03	Butane formation and desorption
10. C2→D1	1.25	-0.52	Butane formation and desorption
11. C1→D2	0.55	-0.65	ZnEt, CuEt, Cudmap, dmap formation
12. C2→D2	0.57	-0.69	ZnEt, CuEt, Cudmap, dmap formation
13. C1→D3	0.61	0.31	Two ethyl group attached to the surface
14. D1→E1	0.34	-0.33	dmap ligand diffusion
15. D1→E2	0.68	0.28	dmap ligand diffusion
16. D2→E3	0.85	-0.68	Butane formation
17. D3→E4	0.33	0.20	dmap ligands diffusion
18. E1→F1	0.44	0.37	dmap ligands diffusion
19. E2→F2	0.62	0.28	dmap ligands diffusion
20. E3→F3	0.71	0.35	Dmap ligands diffusion
21. E4→F4	0.56	0.30	Zn(dmap) <sub>2</sub> formation
22. F1→G1	0.78	0.43	Dmap ligands re-ordering

## 5. Surface Chemistry of Cu ALD by Transmetalation

23. F2→G1	0.15	0.05	Dmap ligands re-ordering
24. F3→G1	0.32	-0.83	Dmap ligands re-ordering
25. F4→G2	0.49	-0.38	Ethyl groups re-ordering
26. G1→H1	0.79	0.72	Zn(dmap) <sub>2</sub> desorption
27. G2→H2	0.73	-1.49	Butane desorption

Adsorption energy of Et<sub>2</sub>Zn (reaction 7 and 8) on decomposed Cu(dmap)<sub>2</sub> is calculated relative to configuration B1 with surface fragments of Cudmap + dmap.

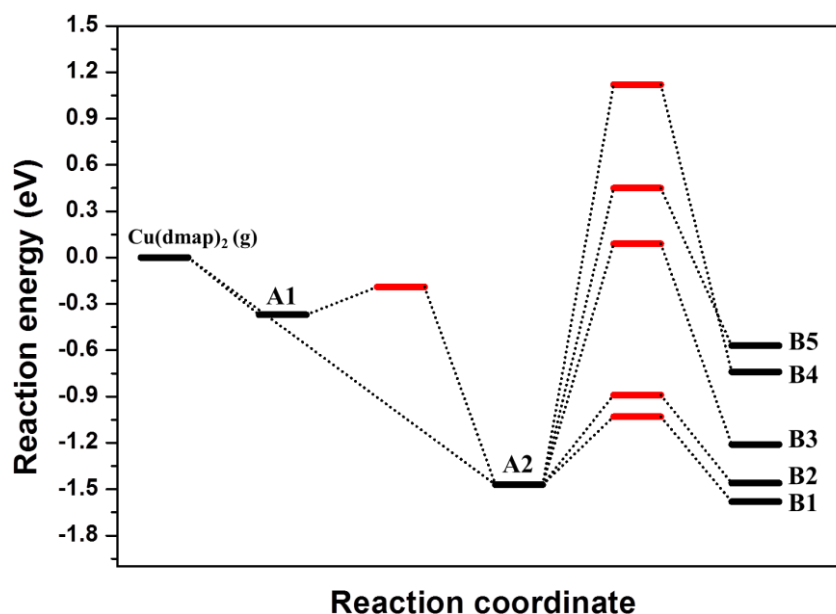


Figure 5.1. First half of the reaction cycle of Cu ALD. Reactant/product states are in black and activation energies are in red. Activation energy greater than 1 eV is not included in the graph.

**A: adsorption of Cu(dmap)<sub>2</sub>.** The physisorbed (A1) and chemisorbed (A2) structures are shown in Figure 5.2. The physisorbed Cu(dmap)<sub>2</sub> molecule is very stable and not spontaneously reactive to Et<sub>2</sub>Zn. Therefore the physisorbed Cu(dmap)<sub>2</sub> molecules should transform into chemisorbed states. Figure 5.1 shows that transformation from the physisorbed (A1) to chemisorbed (A2) structures needs an activation energy ( $E_a$ ) of 0.17 eV, which can be overcome by a typical ALD temperature, e.g. 100 °C.

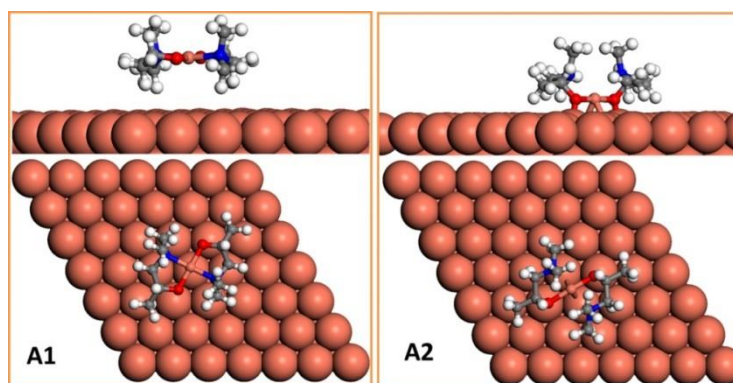


Figure 5.2. Step A: adsorption of  $\text{Cu}(\text{dmap})_2$  on  $\text{Cu}(111)$  surface. A1: physisorption, A2: chemisorption.

**B: decomposition of  $\text{Cu}(\text{dmap})_2$ .** The surface should be saturated with the chemisorbed  $\text{Cu}(\text{dmap})_2$  molecules or fragments to form a monolayer after the  $\text{Cu}(\text{dmap})_2$  pulse during the ALD experiment. We found that  $\text{Et}_2\text{Zn}$  will not react with the chemisorbed  $\text{Cu}(\text{dmap})_2$  molecules on  $\text{Cu}(111)$ . This is because the Cu centre of the molecule is still not accessible, even though the  $\text{Cu}(\text{dmap})_2$  molecule is partially decomposed upon chemisorption. Thus, it is legitimate to assume that the chemisorbed  $\text{Cu}(\text{dmap})_2$  undergoes further decomposition. We considered several possibilities for bond scissions in the  $\text{Cu}(\text{dmap})_2$  molecule: one Cu–O bond (B1), both Cu–O bonds (B2), O–C bond (B3), C–C bond (B4) and C–N bond (B5). We calculated the activation barriers for breaking one ( $\text{A2} \rightarrow \text{B1}$ ) and two ( $\text{A2} \rightarrow \text{B2}$ ) Cu–O bonds to be 0.44 eV and 0.58 eV, respectively, indicating that the reactions are both viable at ALD temperature. The optimized structures for the resulting configuration B1 and B2 are shown in Figure 5.3. In configuration B1, the surface is covered with the dmap and  $\text{Cu}(\text{dmap})$  fragments of the molecule. The distance between the O atom in dmap and the Cu atom in  $\text{Cu}(\text{dmap})$  is 4.45 Å. The O atom in the dmap is located in the hollow site of the  $\text{Cu}(111)$  surface and bonds with three surface Cu atoms. The Cu–N bond is formed (2.10 Å) again in the  $\text{Cu}(\text{dmap})$  because of a reduction of strain in the molecule

## 5. Surface Chemistry of Cu ALD by Transmetalation

---

upon the decomposition. In configuration B2, the distances of the O atoms in the dmap fragments from the adsorbate Cu atom are 3.95 Å and 3.99 Å. Both the O atoms in dmap fragments are located in the hollow site. An N – surface Cu bond is formed (2.31 Å) in one of the dmap ligands, as it is evident from Figure 5.3 that the Cu surface atom under the N atom is pulled up significantly. The reverse reaction to form the  $\text{Cu}(\text{dmap})_2$  molecule from these decomposed fragments is extremely unlikely because the chemisorption of  $\text{Cu}(\text{dmap})_2$  alone needs energy of  $-1.47$  eV.

We now consider decomposition of a dmap ligand from chemisorbed  $\text{Cu}(\text{dmap})_2$  (A2). The calculated activation energies are 1.56 eV for the scission of the O–C bond (A2→B3), 1.92 eV for the scission of C–C bond (A2→B4) and 2.59 eV for the scission of C–N bond (A2→B5). The breaking of the O–C, C–C and C–N bonds are therefore not accessible at a typical ALD reaction temperature of 200 – 300 °C, as in the work done by Lee *et al.* [12] This indicates that the  $\text{Cu}(\text{dmap})_2$  molecules fragment instead through the breaking of one or two Cu–O bond in ALD experiments. This proves that dmap ligands are ‘innocent’ and participate in the reaction as a single unit. In the  $\text{Et}_2\text{Zn}$  pulse, the  $\text{Et}_2\text{Zn}$  molecules may react with the two different fragments of  $\text{Cu}(\text{dmap})_2$ , namely  $\text{Cu}(\text{dmap}) + \text{dmap}$  (B1) and  $\text{dmap} + \text{Cu} + \text{dmap}$  (B2).



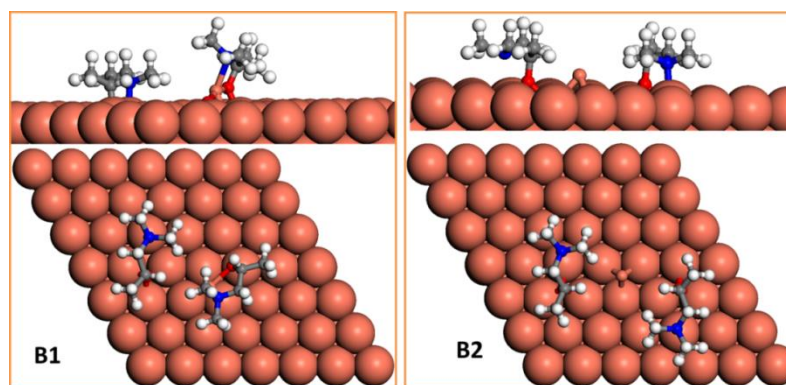


Figure 5.3. Step B: decomposition of  $\text{Cu}(\text{dmap})_2$  on  $\text{Cu}(111)$ . The fragments of decomposed  $\text{Cu}(\text{dmap})_2$  are  $\text{Cu}(\text{dmap}) + \text{dmap}$  (B1) and  $\text{dmap} + \text{Cu} + \text{dmap}$  (B2).

### 5.2.2 Second half reaction: $\text{Et}_2\text{Zn}$ adsorption, butane formation and $\text{Zn}(\text{dmap})_2$ formation

The second half of the Cu ALD transmetalation process is the reaction of  $\text{Et}_2\text{Zn}$  on the surface covered with fragments of  $\text{Cu}(\text{dmap})_2$  to deposit atomic Cu and by-products butane and  $\text{Zn}(\text{dmap})_2$ .

Figure 5.4 shows the reaction energy pathways, which we discuss in detail.

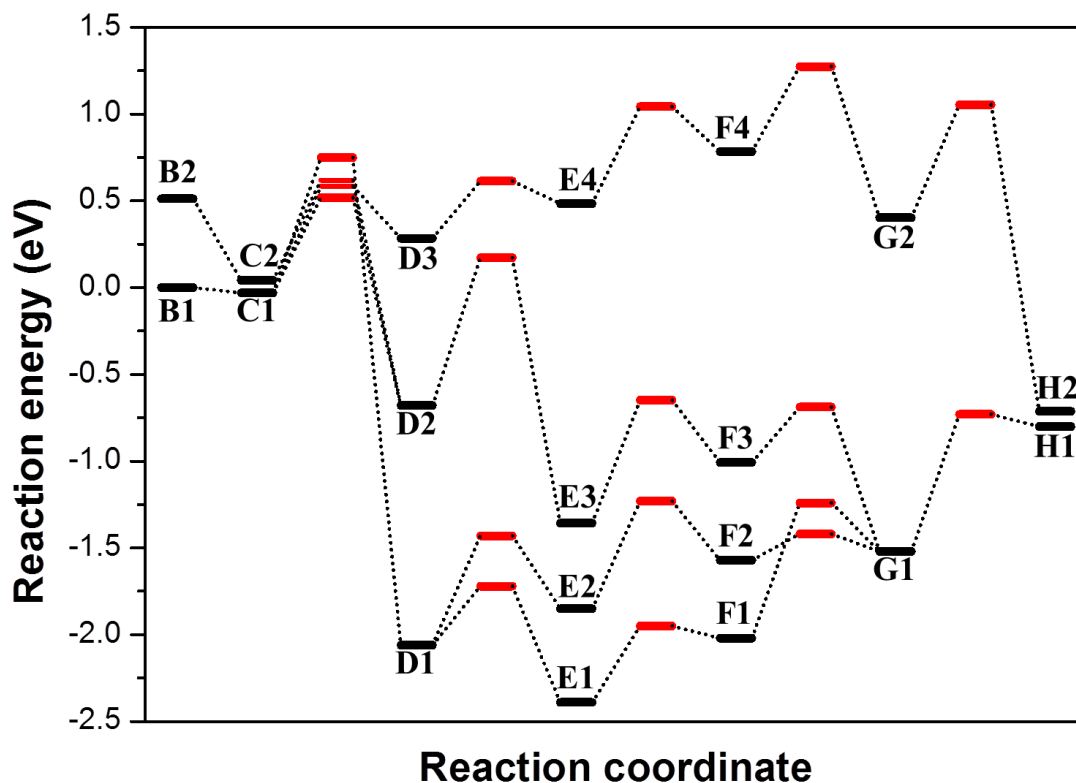


Figure 5.4. Reaction energy diagram for the second half reaction cycle of Cu ALD process. Reactant/product states are in black and activation energies are in red. Activation energy greater than 1 eV is not included in the graph. The configurations labelled with a capital letter and a number are given in the following figures.

**C: adsorption of  $\text{Et}_2\text{Zn}$  on the dmap-covered surface.** Figure 5.5 shows the optimized structures of  $\text{Et}_2\text{Zn}$  adsorption on the configuration B1 and B2, which are labelled C1 and C2, respectively. The adsorption energies of  $\text{Et}_2\text{Zn}$  on configuration B1 and B2 are calculated to be -0.03 eV and 0.01 eV, respectively. These small adsorption energies are apparently the result of significant distortions of both dmap ligands and  $\text{Et}_2\text{Zn}$  molecule on the surface. In the C1 configuration, the  $\text{Et}_2\text{Zn}$  molecule is adsorbed between  $\text{Cu}(\text{dmap})$  and dmap fragments. The Zn atom in the  $\text{Et}_2\text{Zn}$  molecule is situated on a bridge site of  $\text{Cu}(111)$  surface. The ethyl groups are bent upward and the  $\angle\text{C-Zn-C}$  angle is  $134.5^\circ$ . The distance between Zn and the adsorbate Cu atom is 3.11 Å. The Zn – O distances are 4.01 Å and 4.35 Å. In

## 5. Surface Chemistry of Cu ALD by Transmetalation

---

configuration C2, the  $\text{Et}_2\text{Zn}$  molecule is attached on top of the adsorbate Cu atom. The adsorbate Cu atom forms bonds with the Zn atom (Zn–Cu bond length is 2.43 Å) and with the C atom (C–Cu bond length is 2.12 Å) in one of the ethyl groups to form a 3-membered ring. This results in substantial stabilization relative to B2. However, overall, the C1 and C2 structures are very close in energy.

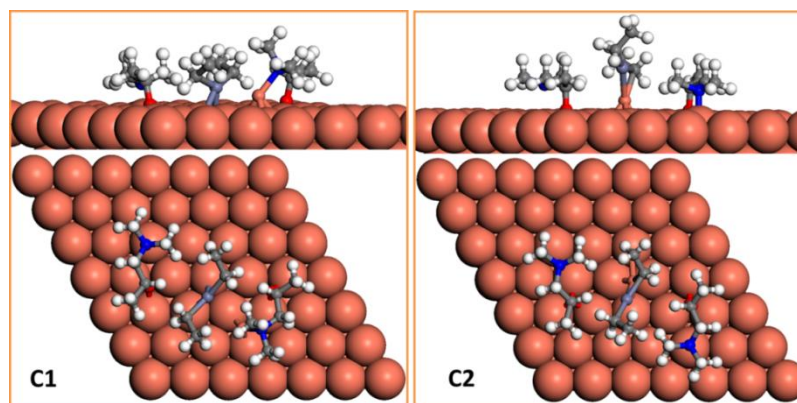


Figure 5.5. Step C: Adsorption of  $\text{Et}_2\text{Zn}$  on the surface with fragments of  $\text{Cu}(\text{dmap})_2$  B1 and B2, respectively.

**D: The ethyl group migration.** As the Zn atom is attached to ethyl groups in configuration C1 and C2, we assume that ethyl groups migrate away from Zn atom in order to give the dmap ligand access to Zn and allow the ethyl groups to form butane. We consider several possibilities for ethyl group migration: (1) direct butane formation from Zn and desorption ( $\text{C1} \rightarrow \text{D1}$ ); (2) one ethyl migration to adsorbate Cu to form CuEt and ZnEt fragments ( $\text{C1} \rightarrow \text{D2}$ ,  $\text{C2} \rightarrow \text{D2}$ ) and (3) migration of both ethyl groups to surface Cu ( $\text{C1} \rightarrow \text{D3}$ ). The final configurations D1, D2 and D3 of ethyl group migrations are shown Figure 5.6. The direct butane formation ( $\text{C1} \rightarrow \text{D1}$ ) is highly exothermic ( $\Delta E = -2.03$  eV, Table 5.1), and needs activation energy of 0.78 eV. Electrons are transferred from desorbing ethyl groups to surface Zn atom. This direct formation of butane is not possible scenario on configuration C2, as evidenced

## 5. Surface Chemistry of Cu ALD by Transmetalation

---

by the calculated activation barrier is 1.32 eV (C2→D1). This is because an extra C – Cu bond was formed in the Et<sub>2</sub>Zn adsorbed on the Cu atom in configuration C2. In the second case, formation of the CuEt and ZnEt fragments attached to the surface (configuration D2) was achieved from both C1 and C2, with the activation energy of 0.55 eV and 0.57 eV, and  $\Delta E$  of -0.7 eV. The configuration D3, with the two ethyl groups migrated to the Cu(111) surface was achieved from configuration C1 with an activation energy of 0.61 eV. We found that achieving D3 from C2 needs activation energy of 1.78 eV, thus making C2→ D3 not possible, probably because this would re-expose the adsorbate Cu atom.

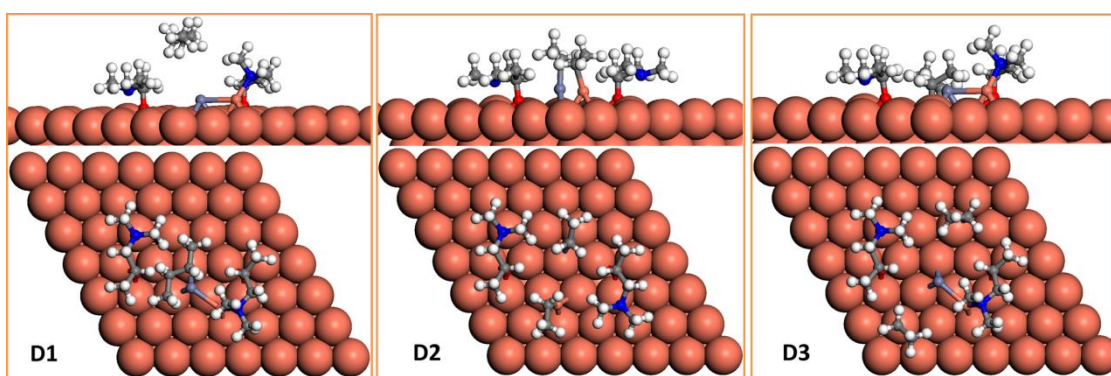


Figure 5.6. Step D: reaction of Et<sub>2</sub>Zn obtained from configuration C1 and C2. Three possibilities are considered: D1 is butane formation; D2 is EtZn + EtCu fragment formation and D3 is fragments of two ethyl groups on Cu(111) surface.

**E: ligand diffusion.** Once the Zn atom becomes accessible for dmap ligands, dmap ligands may diffuse on the surface to form a Zn(dmap)<sub>2</sub> molecule. Figure 5.7 shows the configurations of relevant reaction products obtained from D1, D2 and D3 configurations. The configurations E1 and E2 are obtained from D1 by moving dmap ligands after removing the butane molecule. In configuration E1, a free standing dmap ligand moves toward Zn atom (D1→E1), which needs an activation energy of 0.33 eV

## 5. Surface Chemistry of Cu ALD by Transmetalation

---

and releases energy of  $\Delta E = 0.33$  eV. As can be seen in Figure 5.4, E1 is the most stable surface intermediate that has been found for the  $\text{Et}_2\text{Zn}$  pulse. The activation energy for  $\text{D1} \rightarrow \text{E2}$  is twice greater than that of  $\text{D1} \rightarrow \text{E1}$ . This is because the dmap ligand has to move above the Cu-Zn dimer instead of the smooth Cu(111) surface, which makes the diffusion of dmap more difficult. The butane molecule is formed from two ethyl groups attached to the Cu and Zn in configuration E3, with the activation energy  $E_a$  of 0.85 eV and the reaction energy  $\Delta E$  of -0.68 eV. The Cu and Zn atom distance is 4.47 Å and the distances between O atoms in the dmap ligand and the Zn atom are 4.22 Å and 4.69 Å in configuration E3. We also checked the formation of (dmap)CuEt intermediate product from configuration E3 through moving CuEt fragments to the dmap ligand in D2 configuration, which has  $E_a$  of 0.44 eV and  $\Delta E = 0.16$  eV. We found that butane formation and ethyl group migrations to the surface from the (dmap)CuEt covered surface are not likely because the activation barriers for these two processes are quite high (1.35 and 1.11 eV, respectively, not listed in Table 5.1). Since the reaction energy of forming the intermediate product (dmap)CuEt is endothermic (0.16 eV), the reverse reaction from the intermediate product to form the CuEt and ZnEt in configuration D2 may take place with the reverse activation barrier 0.28 eV. In configuration E4, two dmap ligands diffuse toward the Zn atom to form  $\text{Zn}(\text{dmap})_2$  molecule, which is obtained from D3. The  $\text{D3} \rightarrow \text{E4}$  transition has the activation energy of 0.33 eV. Clearly, through the reaction pathway  $\text{B1} \rightarrow \text{C1} \rightarrow \text{D3} \rightarrow \text{E4}$ , the  $\text{Zn}(\text{dmap})_2$  is formed when the ethyl groups are donated to the surface.

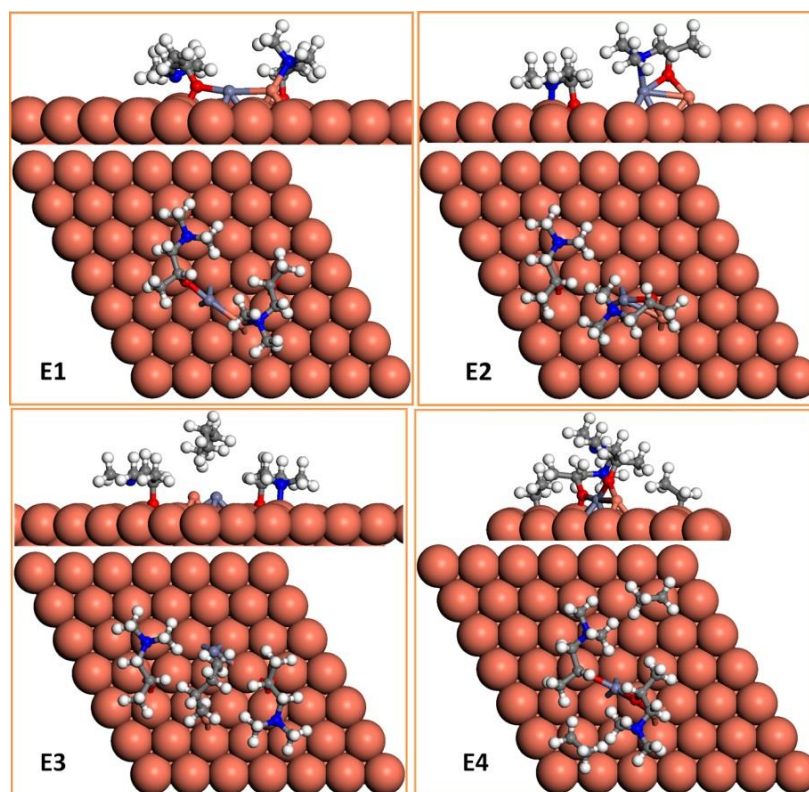


Figure 5.7. step E: ligand diffusion. E1 and E2 are reaction products of D1. E3 and E4 are the reaction products of D2 and D3, respectively.

**F: ligand re-ordering.** After the dmap ligands have diffused towards the Zn atom, they may re-order their atomic positions to form a  $\text{Zn}(\text{dmap})_2$  molecule. Figure 5.8 shows the re-ordered ligands. The  $\text{E1} \rightarrow \text{F1}$  reaction needs activation of 0.44 eV. As we can see from the F1 configuration, the  $\text{Zn}(\text{dmap})_2$  structure is deformed with N–Zn distance 3.8 Å. The reaction  $\text{E2} \rightarrow \text{F2}$  needs  $E_a$  of 0.62 eV. In this case, the long O–Zn distance is 4.2 Å. Thus, in the F2 configuration, the ligands have to move further to form  $\text{Zn}(\text{dmap})_2$  molecule. The O atoms in dmap ligands are attached to the Zn atom in F3 configuration, which is obtained from E3 after removing the butane molecule. This process ( $\text{E3} \rightarrow \text{F3}$ ), that is slightly exothermic with the reaction energy of -0.35 eV, has the activation barrier of 0.71 eV. In F4 configuration, the  $\text{Zn}(\text{dmap})_2$  by-product molecule is formed and desorbed from the surface in the presence of two ethyl

groups on the surface (F4). Obtaining F4 from E4 needs the  $E_a$  of 0.56 eV and  $\Delta E$  of 0.30 eV.

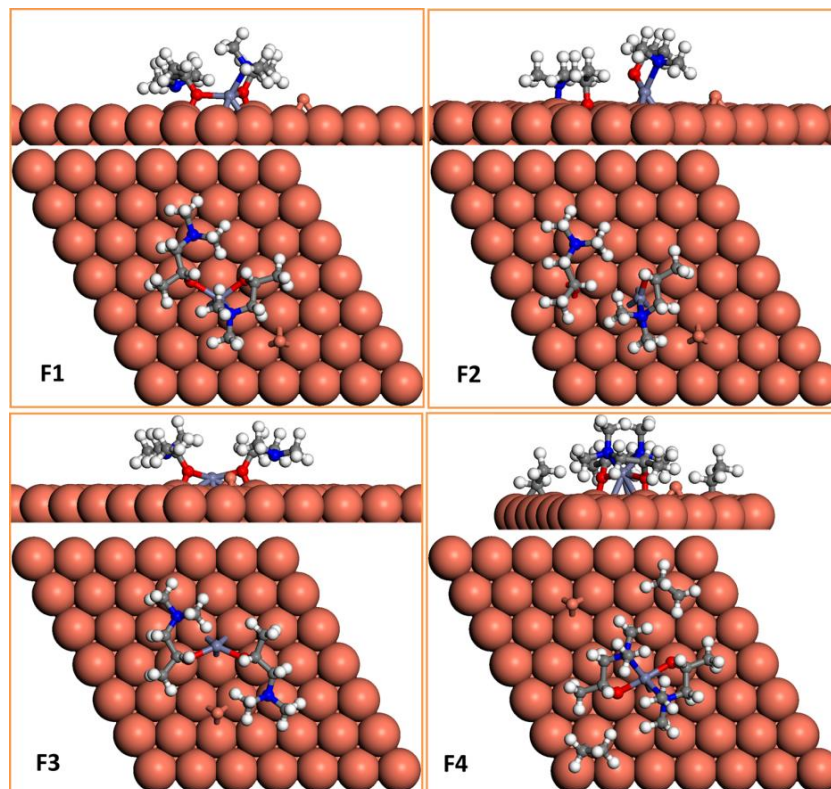


Figure 5.8. Step F: ligand re-ordering. configuration F1 and F2 are reaction products of E1 and E2, respectively.

**G:  $\text{Zn}(\text{dmap})_2/\text{butane}$  formation.** After ligand diffusion and ligand re-ordering steps, a  $\text{Zn}(\text{dmap})_2$  molecule can be formed from these re-ordered ligands. Because the F1, F2 and F3 configurations have the same surface elements and only the location of dmap and  $\text{Zn}(\text{dmap})$  fragments differ slightly, we merge them to a single configuration G1, as shown in Figure 5.9. The activation energy from achieving G1 from F1 (0.78 eV) is approximately twice greater than that of achieving G1 from F3 (0.32 eV). The process  $\text{F2} \rightarrow \text{G1}$  only needs activation energy of 0.15 eV because the Zn atom is already coordinated to the damp ligand in the previous step. The two processes of  $\text{Zn}(\text{dmap})_2$  formation from F1 and F2 are endothermic with the reaction energies of 0.43 eV and 0.05 eV, respectively. In configuration G1,  $\text{Zn}(\text{dmap})_2$  is not fully shaped

## 5. Surface Chemistry of Cu ALD by Transmetalation

---

as one of the Cu–N bond lengths is greater than its gas phase bond length by 1.6 Å. By comparing the Cu(dmap)<sub>2</sub> chemisorbed on Cu(111) with configuration G1, we can find that it has some common features: O–Zn–O atoms form bonds with the surface Cu atoms, and N-containing parts of the ligand are distorted. This indicates that G1 is indeed the chemisorbed Zn(dmap)<sub>2</sub> on Cu(111) surface. Next, this chemisorbed Zn(dmap)<sub>2</sub> molecule should desorb from the surface.

The ethyl groups or the deposited Cu adatom migrate to form a butane molecule in configuration G2, which follows the desorption of the Zn(dmap)<sub>2</sub> molecule in configuration F4. We found that formation of butane from ethyl groups on the smooth surface is not favourable, because it needs activation energy of 1.25 eV. As the deposited Cu adatom can diffuse on the surface with the relatively small energy cost ( $E_a = 0.02$  eV from one hollow site to the neighbouring hollow site), we moved the deposited Cu adatom between the two ethyl groups to form the Cu(Et)<sub>2</sub> intermediate. The activation barrier to form the Cu(Et)<sub>2</sub> in configuration G2 from F4 (after removing the Zn(dmap)<sub>2</sub> molecule and moving the deposited Cu adatom between two ethyl groups) is 0.49 eV. The reaction is slightly exothermic with the reaction energy of –0.38 eV. This indicates that butane formation is only possible on rough surfaces during the ALD process.



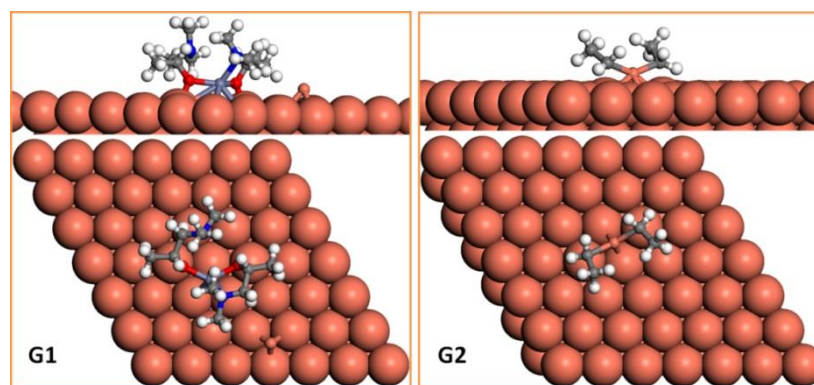


Figure 5.9. step G:  $\text{Zn(dmap)}_2$  formation.

**H:  $\text{Zn(dmap)}_2$ /butane desorption.** In G1 configuration, dmap ligands re-ordered to form  $\text{Zn(dmap)}_2$  and in H1 this molecule desorbs (Figure 5.10). The calculated activation barrier  $E_a$  is 0.79 eV and the reaction energy  $\Delta E$  is 0.72 eV, i.e. the desorption of  $\text{Zn(dmap)}_2$  is endothermic. The Zn–O and Zn–N bond distances are 1.89 Å and 2.30 Å, respectively. The Zn–surface distance is 4.2 Å, which indicates that the molecule is almost not interacting with the surface. The desorbed  $\text{Zn(dmap)}_2$  by-product molecule can be purged away to vacate the surface for the new  $\text{Cu(dmap)}_2$  molecules in the next ALD cycle.

In the H2 configuration, which is obtained from configuration G2, the butane molecule desorbs through the decomposition of the  $\text{Cu(Et)}_2$  molecule, which needs an activation energy of 0.73 eV. The  $\text{G2} \rightarrow \text{H2}$  process is strongly exothermic, consistent with the process  $\text{C1} \rightarrow \text{D1}$ . Once again, reduction of the surface cations to metallic Cu is achieved in this step by donation of electrons from ethyl groups as they combine into butane and desorb. As we described above, the metallic Cu atom may be deposited through two different pathways.

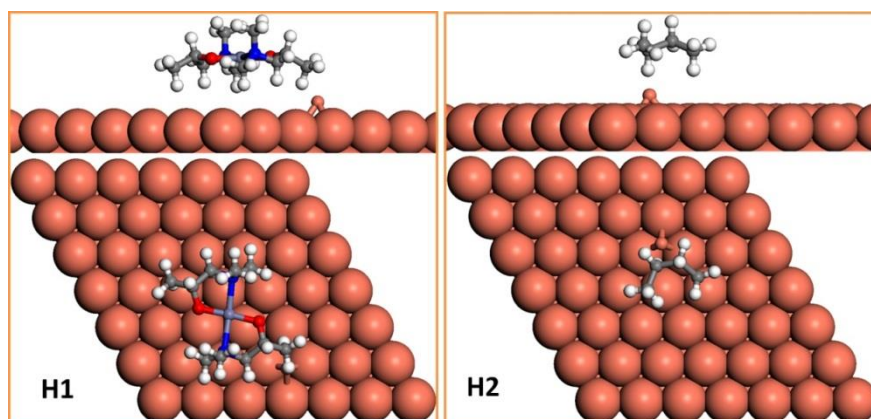


Figure 5.10. Step H:  $\text{Zn(dmap)}_2$  (H1) or butane (H2) desorption.

### 5.3 Discussion

#### 5.3.1 The reaction mechanism of Cu ALD

The results on the first half reaction cycle shows that the  $\text{Cu(dmap)}_2$  pulse just seems to involve dissociative chemisorption with ligands intact. In the original experimental work, the film thickness per cycle for  $\text{Cu(dmap)}_2$  is saturated when the pulse time exceeds 2 s.[12] This relatively long pulse time of  $\text{Cu(dmap)}_2$  allows the full saturation of the surface with the fragments of  $\text{Cu(dmap)}_2$ . During the second pulse, we predict that butane molecule is formed just after adsorption of  $\text{Et}_2\text{Zn}$ , and this reaction is extremely exothermic. In the experimental work,[12] the pulse time for  $\text{Et}_2\text{Zn}$  is 0.5 s and it was found that  $\text{Et}_2\text{Zn}$  undergoes a fast self-terminating replacement reaction with the  $\text{Cu(dmap)}_2$  adsorbed on the surface, which seems to be consistent with our result.

The reaction pathways based on Figure 5.1 and Figure 5.4 are schematically illustrated in Figure 5.11. In the first pathway, the butane formation takes place just after  $\text{Et}_2\text{Zn}$  adsorption. Then the dmap ligands diffuse and re-order to form the  $\text{Zn(dmap)}_2$  molecule, which finally desorbs from the Cu surface. In the second reaction pathway (Figure 5.11b), the ethyl groups migrate away from Zn to the surface. This provides

## 5. Surface Chemistry of Cu ALD by Transmetalation

---

dmap ligands with access to diffuse toward the free Zn atom and to re-order to form the  $\text{Zn}(\text{dmap})_2$  molecule. The formation of butane on the smooth Cu surface is not preferred as it requires rather high activation barrier. The formation of intermediate product  $\text{Cu}(\text{Et})_2$  helps the formation of butane because the activation energy is significantly lowered by the migration of the Cu adatom. It is possible that these two types of reactions take place at the same time, with different reaction rates.

As we can see from Figure 5.4, the reaction energies of most of the ligand diffusion and ligand re-ordering steps leading to  $\text{Zn}(\text{dmap})_2$  are endothermic and the reaction pathways are uphill in these stages. This indicates that the activation barrier for the reverse reactions is smaller than that of forward reactions. Thus the rates of reverse reactions can be higher than those of the forward reactions during the ligand diffusion and re-ordering steps. Nevertheless, desorption of  $\text{Zn}(\text{dmap})_2$  is expected to be irreversible, and this will drive the equilibrium (slowly) towards formation of the product. Residual adsorbed dmap may block sites against adsorption of  $\text{Cu}(\text{dmap})_2$  in the next ALD cycle. This may lead to a slower growth rate during ALD. Lee *et al* reported that the growth rate is  $0.2 \text{ \AA}/\text{cycle}$  with  $\text{Cu}(\text{dmap})_2$  and  $\text{Et}_2\text{Zn}$  in their ALD work.[12] Slow desorption of the Zn by-product may result in incorporation of Zn into the growing metallic film as an impurity. Indeed 10 % Zn is detected in the experiment.[11]

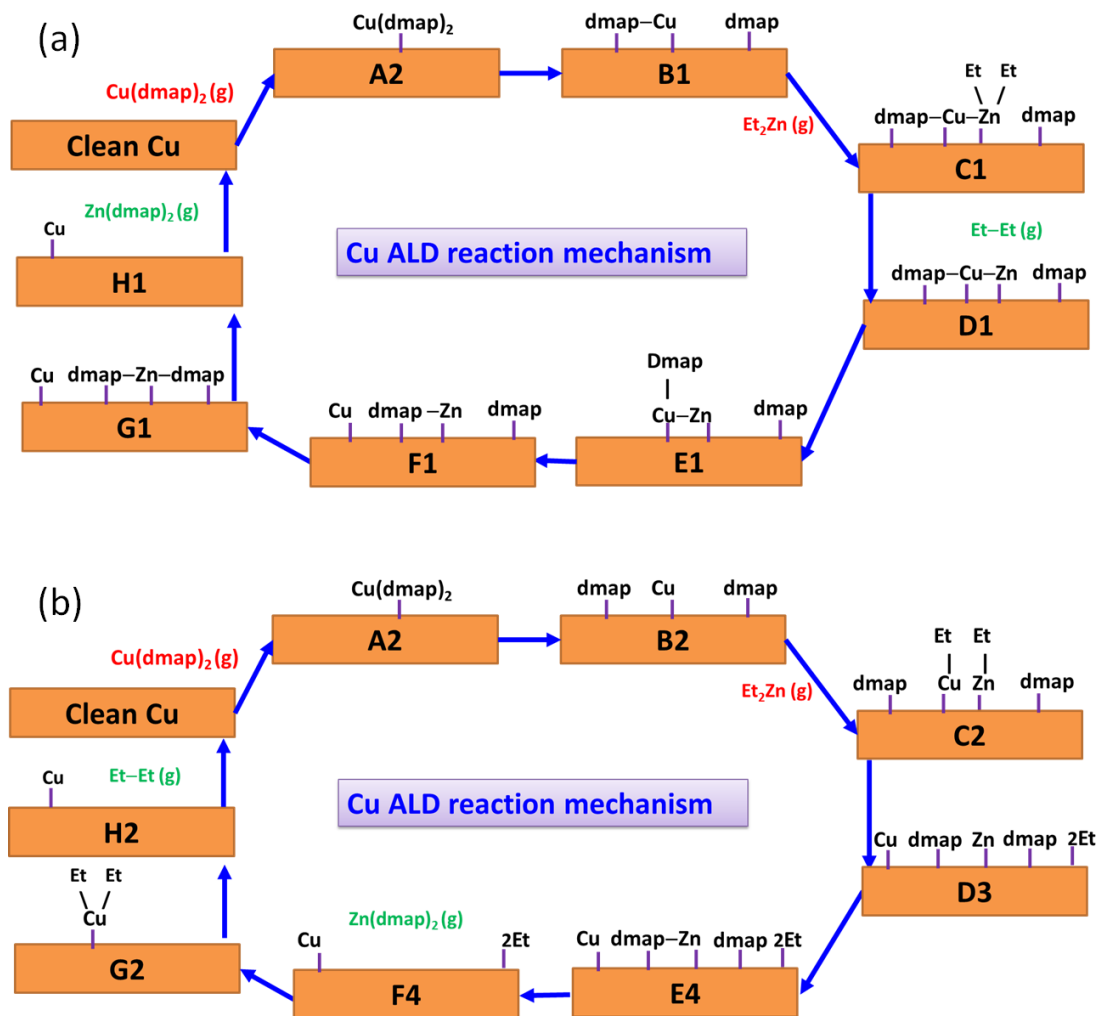


Figure 5.11. The schematic illustration of reaction mechanisms of copper ALD by transmetalation from  $\text{Cu(dmap)}_2$  and  $\text{Et}_2\text{Zn}$ .

## 5.4 Conclusion

Atomic layer deposition (ALD) has been a promising method to deposit conformal and uniform thin film of copper for future microelectronic devices. However, the reaction mechanism and the surface chemistry of copper ALD remain unclear. In this Chapter, we employ density functional theory to study the ALD reaction of copper dimethylamino-2-propoxide [ $\text{Cu(dmap)}_2$ ] and diethylzinc [ $\text{Et}_2\text{Zn}$ ] based on the seminal paper of Lee et al. [Angew. Chemie Int. Ed. **2009**, 48, 4536–4539]. We conclude

## 5. Surface Chemistry of Cu ALD by Transmetallation

---

based on activation energies and reaction energies for a range of surface reactions that there are two different reaction pathways in the  $\text{Et}_2\text{Zn}$  pulse. We found that the chemisorbed  $\text{Cu}(\text{dmap})_2$  decomposes through breaking of one or both Cu–O on Cu(111) after the  $\text{Cu}(\text{dmap})_2$  pulse. The butane formation and the migration of ethyl groups to the surface are two possible routes for the decomposed  $\text{Et}_2\text{Zn}$  after its adsorption on the Cu(111) surface saturated with the decomposed  $\text{Cu}(\text{dmap})_2$ . In the first case, the butane formation/desorption is followed by the diffusion and reordering of dmap ligands around the Zn atom to form the  $\text{Zn}(\text{dmap})_2$  molecule. In the second case, the dmap ligands diffuse and re-order around the Zn atom. The  $\text{Zn}(\text{dmap})_2$  is formed and desorbed in the presence of ethyl groups, which is followed by butane formation and desorption with the assistance of migrating Cu atom.

Because the butane formation and desorption steps are extremely exothermic, the ALD reaction in reaction scheme (5.1) is possible. However, the ligand diffusion and re-ordering steps are endothermic which may result in residual dmap ligands blocking surface sites at the end of the  $\text{Et}_2\text{Zn}$  pulse, and in residual Zn being reduced and incorporated as an impurity. This may lead to very slow growth rate, as was the case in the experimental work.

## 6 The Reduction Of CuO To Metallic Copper<sup>2</sup>

### 6.1 Introduction

ALD processes where only one co-reagent is used after the copper organometallic compound pulse have a low growth rate and require relatively high temperature, which leads to the agglomeration of Cu islands at substrates.[22] A three-step ALD process which uses two co-reagents consecutively was found to enhance the growth rate.[23] These indirect approaches for metal ALD from oxides and nitrides are based on the reduction of the corresponding oxide/nitride,[16] *i. e.* an ALD cycle for depositing the metal oxide or nitride and reduction to the metal with a pulse of reducing agent. Examples of this indirect approach to metal ALD include ALD of Cu<sub>3</sub>N followed by reduction to Cu metal by treatment with H<sub>2</sub> at 160 °C[126] and ALD of CuO followed by reduction to Cu metal with H<sub>2</sub> at 270–320 °C.[16] More recently, Knisley *et al.* reported low temperature deposition of high purity copper film through ALD of copper(II) formate, which is then readily reduced to Cu metal by a hydrazine (N<sub>2</sub>H<sub>4</sub>) pulse at 80 °C.[22] Cu islands and discontinuous thin films on the substrate are observed in these indirect ALD methods after the reduction to metallic Cu. Kalutarage *et al.* compared two-step process and three-step process using the ALD reaction of Cu(dmap)<sub>2</sub> with BH<sub>3</sub>(NHMe<sub>2</sub>) and separately with BH<sub>3</sub>(NHMe<sub>2</sub>) and HCO<sub>2</sub>H.[23] They showed that the two-step process requires a Cu seed layer, and affords a growth rate of about 0.13 Å/cycle within the 130–160 °C ALD window. The three-step process does not need a Cu seed layer for growth, and affords a growth rate of 0.20

---

<sup>2</sup> (Content of this chapter is published in *Physical Chemistry Chemical Physics*. See ref [74]).

## 6. The Reduction Of CuO To Metallic Copper

---

Å/cycle within the 135–165 °C ALD window. Indirect ALD has also been applied to deposit other metals. An atomic layer of NiO is reduced to Ni metal after the ALD process using hydrogen radical at 165 °C.[127] Ir metal is obtained from reducing IrO<sub>2</sub> by applying a H<sub>2</sub> pulse at 120–180 °C after each ALD cycle of IrO<sub>2</sub>. [120]

Ideally, the reduction process that follows ALD should be carefully chosen so as to obtain conformal and uniform thin metal films at low temperature, but it is not clear whether it is possible. Experimentally, metal oxides have been reduced to corresponding metals using different methods. Lee et al. reduced CuO to metallic copper through vacuum annealing at 673 K.[128] Kim et al. reported CuO reduction at atmospheric pressure of H<sub>2</sub> and temperatures of 423–573 K.[129,130] Reduction of NiO with H<sub>2</sub> was studied by Rodriguez and co-workers using in situ time-resolved XRD and NEXAFS/EXAFS at atmospheric pressure of H<sub>2</sub> and temperatures of 523–623 K.[131] In order to improve the process of Cu film growth, it is necessary to understand the reduction mechanisms of metal oxide films and surfaces to the corresponding metals.

In this chapter, we study the reduction of a CuO surface (that would be grown with ALD) to metallic Cu using density functional theory (DFT) with the generalized gradient approximation (GGA) corrected for on-site Coulomb interactions through the Hubbard U correction (GGA + U) and with a screened hybrid density functional (HSE06).[132,133] The CuO(111) surface is the most stable, as measured by surface energy, and hence we consider only this surface for our study (Section 6.2.1). Two possible mechanisms for CuO reduction to metallic Cu are studied: direct formation of oxygen vacancies by removal of neutral oxygen from surface and subsurface as the model of vacuum annealing method in ref. [128] (Section 6.2.2) and the reaction of

H<sub>2</sub> with oxygen on the CuO(111) surface to form water as the model of reduction of CuO with reducing agent H<sub>2</sub> in ref [129] and [130] (Section 6.2.3). Using ab initio atomistic thermodynamics, we relate our computational results with these two different reduction methods, and we get new insight into how the CuO surface is reduced to metallic Cu.

### 6.2 Computational methods

All calculations were performed using DFT implemented in the VASP code,[125] in which the valence electron states are expanded in a plane-wave basis set with an energy cutoff of 400 eV.[85] Exchange and correlation are treated within the generalized gradient approximation (GGA), using the Perdew–Burke–Ernzerhof (PBE) functional.[134] Since conventional DFT functionals are unable to adequately describe the strong correlation effect among the partially filled Cu 3d states in CuO,[135] the Hubbard parameter,  $U$ , is introduced for the Cu 3d electrons to describe the on-site Coulomb interaction, giving the well-known GGA +  $U$  method.[136] The values of  $U = 7$  eV and  $J = 0$  eV for CuO were adopted from ref. [137]. Spin polarized calculations were performed since bulk CuO has an antiferromagnetic ground state. For bulk CuO, an  $8 \times 8 \times 8$  k-point grid within the Monkhorst–Pack scheme in the Brillouin zone was employed. To allow the vacancy formation energy and adsorption energy to be obtained, gas phase H<sub>2</sub>, O<sub>2</sub> and H<sub>2</sub>O molecules were calculated in the CuO(111)-(2 × 1) supercell without CuO. Full geometry relaxation of all surface structures was carried out using the conjugate gradient method for energy minimization until the forces on each ion were less than 0.02 eV Å<sup>-1</sup>.

To study oxygen vacancy formation and H<sub>2</sub> adsorption on CuO(111) surface, a (2 × 1) surface supercell expansion was used and a (2 × 2) surface supercell was also used



## 6. The Reduction Of CuO To Metallic Copper

---

to check the results for oxygen vacancy formation. The slab thickness was six layers (12.4 Å), with a 15 Å vacuum gap. The Brillouin zone was sampled with a  $4 \times 8 \times 1$  k-point grid. For the oxygen vacancy calculations, we validate our results by using the Heyd–Scuseria–Ernzerhof (HSE06) hybrid functional with a screening length of 0.2 Å<sup>-1</sup>, where correlation is described in GGA (PBE) and the exchange is a mixture of 25% exact (HF) exchange and 75% PBE exchange.[132,133] A  $2 \times 4 \times 1$  k-point grid is used for all the HSE06 calculations due to the computational intensity of the hybrid functional.

The formation energy per oxygen vacancy is defined as

$$E_{\text{vac}} = E(\text{CuO}_{1-n\delta}) - E(\text{CuO}_{1-(n-1)\delta}) + \frac{1}{2}E(\text{O}_2) \quad (6.1)$$

where  $E(\text{CuO}_{1-n\delta})$  and  $E(\text{CuO}_{1-(n-1)\delta})$  are the energies of the slabs with  $n$  and  $n - 1$  number of oxygen vacancies, respectively. Here, a positive number is energetic cost.  $\delta$  is the vacancy concentration that results from removing one oxygen atom from the cell. In our ( $2 \times 1$ ) slab,  $\delta = 0.25$  for one oxygen vacancy in a layer.  $E(\text{O}_2)$  is the energy of oxygen molecule in the gas phase and corresponds to the chemical potential of oxygen gas at standard pressure and  $T = 0$  K. While the GGA method overbinds the  $\text{O}_2$  molecule by 0.7 eV per atom relative to experiment,[109] which leads to overstabilisation of an oxygen vacancy, the trends in oxygen vacancy stability are expected to be unaffected by this constant error. The HSE06 functional has been used by Ganduglia-Pirovano *et al.* for studying oxygen vacancies in the  $\text{CeO}_2$  surface, where they found that DFT + U and HSE06 predict the relative stability correctly.[138] Thus, the impact of overstabilisation of oxygen vacancies in our calculations can be assessed by using HSE06.

## 6. The Reduction Of CuO To Metallic Copper

---

For the adsorption of H<sub>2</sub> onto the CuO(111) surface, the adsorption energy  $\Delta E_{\text{ads}}$  is calculated from:

$$\Delta E_{\text{ads}} = E(\text{H}_2@\text{CuO}_{1-n\delta}) - E(\text{CuO}_{1-n\delta}) - E(\text{H}_2) \quad (6.2)$$

where  $E(\text{H}_2@\text{CuO}_{1-n\delta})$  is the energy of CuO(111) surface with  $n$  oxygen vacancies and a H<sub>2</sub> molecule adsorbed.  $E(\text{H}_2)$  is the energy of a hydrogen molecule in the gas phase and thus represents conditions of  $P_{\text{H}_2} = 1$  atm and  $T = 0$  K.

The desorption energy of a water molecule from the partially reduced CuO(111) surface after H<sub>2</sub> adsorption is calculated from:

$$\Delta E_{\text{des}} = E(\text{CuO}_{1-(n-1)\delta}) + E(\text{H}_2\text{O}) - E(\text{H}_2@\text{CuO}_{1-n\delta}) \quad (6.3)$$

where  $E(\text{H}_2\text{O})$  is the energy of a water molecule in the gas phase. If the desorption energy is negative, desorption of the water molecule into the vacuum is favourable. The reduction energy  $\Delta E_{\text{red}}$  of the CuO(111) surface with H<sub>2</sub> is thus defined as the sum of adsorption and desorption energies above:

$$\Delta E_{\text{red}} = \Delta E_{\text{ads}} + \Delta E_{\text{des}} \quad (6.4)$$

In order to investigate the surface stability across a range of experimental conditions, we apply ab initio thermodynamics[68] to the two cases of CuO(111) surface reduction – oxygen vacancy formation and H<sub>2</sub> adsorption on the CuO(111) surface. At temperature  $T$ , and pressure  $P$ , the surface free energy of the CuO(111) surface can be defined

$$\gamma(T, P) = \frac{1}{A} \left[ G - \sum_i N_i \mu_i(T, P) \right] \quad (6.5)$$

where  $G$  is the Gibbs free energy of the solid with the surface area  $A$ .  $\mu_i(T, P)$  is the chemical potential of the  $i$ th species and  $N_i$  is the number of units in the system. In the

## 6. The Reduction Of CuO To Metallic Copper

---

first case, for vacuum annealing of CuO (Section 6.2.2), only two atom types are present and react according to the stoichiometry  $\text{Cu} + \text{O} \rightarrow \text{CuO}$  so that  $\mu_{\text{Cu}} + \mu_{\text{O}} = \mu_{\text{CuO}}$ . Hence Equation (6.5) can be written as a function of one chemical potential:

$$\begin{aligned} \gamma(T, P) &= \frac{1}{A} [E_{\text{slab}} - N_{\text{Cu}}\mu_{\text{Cu}} - N_{\text{O}}\mu_{\text{O}}] \\ &= \frac{1}{A} [E_{\text{slab}} - N_{\text{Cu}}\mu_{\text{CuO}} - N_{\text{vac}}\mu_{\text{O}}] \end{aligned} \quad (6.6)$$

where  $N_{\text{vac}} = N_{\text{Cu}} - N_{\text{O}}$  is the number of oxygen vacancies on the CuO(111) surface, and the plus sign means an oxygen deficiency in the system. The oxygen chemical potential  $\mu_{\text{O}}$  can be related to the oxygen pressure  $P$  and the temperature  $T$  by

$$\mu_{\text{O}}(T, P) = \mu(T, P^0) + \frac{1}{2}kT \ln \frac{P}{P^0} \quad (6.7)$$

To determine the range of the oxygen chemical potential, we set the maximum value of  $\mu_{\text{O}}(T, P)$  to be the total energy of oxygen in the gas phase, i.e.,  $\mu_{\text{O}}(0, P^0) = \frac{1}{2}E(\text{O}_2) = 0$ , which corresponds to the oxygen-rich condition. The minimum of  $\mu_{\text{O}}(T, P)$  can be defined as the condition where bulk CuO transforms to Cu bulk and releases oxygen and this corresponds to the oxygen-poor condition. Thus, the allowed range of  $\mu_{\text{O}}$  is

$$\mu_{\text{CuO}} - \mu_{\text{Cu}} < \mu_{\text{O}} < \frac{1}{2}E(\text{O}_2) \quad (6.8)$$

From this we can obtain the allowed range for the change in  $\mu_{\text{O}}$ , which is

$$h_{\text{CuO}} < \Delta\mu_{\text{O}} < 0 \quad (6.9)$$

where  $h_{\text{CuO}} = E_{\text{CuO}}^{\text{bulk}} - E_{\text{Cu}}^{\text{bulk}} - \frac{1}{2}E(\text{O}_2)$ , denotes the formation energy of bulk CuO, and where,

$$\Delta\mu_O = \mu_O - \frac{1}{2}E(O_2) \quad (6.10)$$

In the second case, we consider the effect of a chemical reducing agent, namely H<sub>2</sub> gas (section 6.2.2). In principle this introduces an additional variable  $\mu_{H_2}$ . However, given that  $H_2 + \frac{1}{2}O_2 \rightarrow H_2O$ , it is experimentally reasonable to set  $\mu_{H_2O} = E(H_2O)$  as constant and restrict our focus to the oxygen poor condition  $\mu_O \leq \mu_{CuO} - \mu_{Cu}$ . Now the single variable  $\mu_{H_2}$  can range between  $\mu_{H_2} = E(H_2)$  and  $\mu_{H_2} = \mu_{H_2O} - \mu_O = E(H_2O) - \mu_{CuO} + \mu_{Cu}$ . Hence,  $\mu_O$  is given by,

$$\mu_O = \mu_{H_2O} - \mu_{H_2} \quad (6.11)$$

and the available range of oxygen chemical potential  $\mu_O$  is taken as follows,

$$\mu_{H_2O} - \mu_{H_2} < \mu_O < \mu_{CuO} - \mu_{Cu} \quad (6.12)$$

This indicates that the minimum value of  $\mu_O$  during the reduction of CuO via oxygen vacancies is the maximum value of  $\mu_O$  during the reduction of CuO surface with H<sub>2</sub> adsorption.

### 6.2.1 CuO surface

To check the applicability and accuracy of the GGA + U approach with the chosen parameters, we first performed calculations to optimize the structural parameters of bulk CuO (space group with C2/c). The calculated lattice parameters are  $a = 4.683 \text{ \AA}$ ,  $b = 3.43 \text{ \AA}$ ,  $c = 5.138 \text{ \AA}$ ,  $\beta = 99.2^\circ$  and the Cu–O distance is  $1.95 \text{ \AA}$ , in good agreement with experimental data.[139] Figure 6.1(a) shows the bulk structure and antiferromagnetic spin ordering in bulk CuO. Figure 6.2 shows the total electronic density of states (DOS) and the DOS projected on Cu and O states in bulk CuO. The GGA + U band gap is about 1.3 eV which is underestimated compared to experiment (1.9 eV)[140] and consistent with an earlier calculation (1.1 eV).[141] The calculated

## 6. The Reduction Of CuO To Metallic Copper

---

magnetic moment per Cu atom is  $0.63 \mu_B$ , which is consistent with experiment ( $0.68 \mu_B$ ). [142] This indicates that the GGA + U approach with chosen U and J is appropriate for describing the ground state of antiferromagnetic bulk CuO.

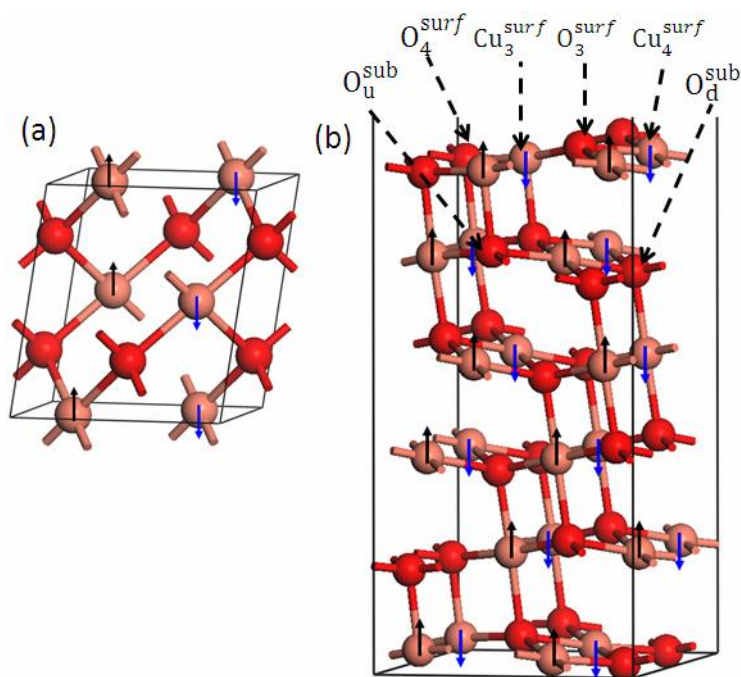


Figure 6.1. Structure and antiferromagnetic spin ordering of (a) CuO bulk. (b) CuO(111) slab. The red and salmon pink balls represent oxygen and copper atoms, respectively and this colour scheme is used throughout the chapter. Arrows in black represent spin up states and arrows in blue represent spin down states. Four coordinated Cu and O atoms on the surface are labelled  $Cu_4^{surf}$  and  $O_4^{surf}$ , while three coordinated Cu and O atoms are labelled  $Cu_3^{surf}$  and  $O_3^{surf}$ , respectively. The subsurface oxygen atoms which coordinated with three Cu atoms on the subsurface and one Cu atom on the surface are labeled  $O_u^{sub}$ ; the subsurface oxygen atoms which coordinated with three Cu atoms on the subsurface and one Cu atom on the subsurface are labeled  $O_d^{sub}$ .

## 6. The Reduction Of CuO To Metallic Copper

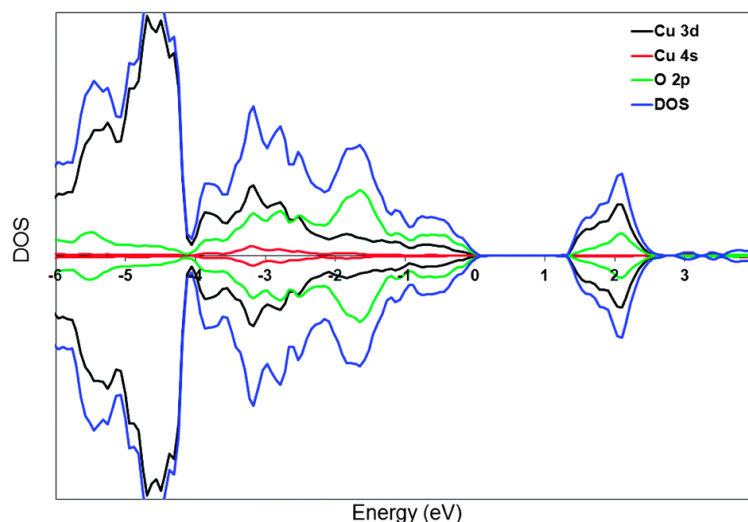


Figure 6.2. Total electronic density of states (DOS) and projection of the DOS onto Cu 3d and 4s and O 2p states of CuO bulk. The top of the valence band is aligned to 0 eV.

To identify the most stable surface of CuO, several different low index surfaces are studied. Surface energies for these surfaces are calculated with the formula  $\gamma_{\text{surf}} = (E_{\text{slab}} - nE_{\text{bulk}})/2A$ , where  $E_{\text{slab}}$  is the energy of stoichiometric CuO,  $E_{\text{bulk}}$  is the CuO bulk energy and  $A$  is the cross-sectional area of the slab. The factor of 2 comes from the two slab surfaces. The computed surface energies are 0.72, 0.91, 1.18, 1.68 and 2.24 J m<sup>-2</sup> for CuO(111), CuO(011), CuO(110), CuO(010) and CuO(100) stoichiometric surfaces, respectively. This indicates that the CuO(111) surface is the most stable compared to other stoichiometric surfaces, which is consistent with the report by Hu et al.[141] The surface energies of nonstoichiometric surfaces including O- and Cu-terminated CuO(110) and CuO(100) are evaluated in that paper as a function of  $\mu_{\text{O}}$ , and it is found that these nonstoichiometric surfaces are only more stable than CuO(111) surface in a very narrow range near the limit of O-rich condition which is difficult to achieve in typical experimental conditions.[141] Thus we choose the stoichiometric CuO(111) surface as a model surface to study the reduction process of the CuO. For the CuO(111) surface calculation, we find that a bulk-like magnetic

## 6. The Reduction Of CuO To Metallic Copper

---

ordering is the most stable, which is depicted by arrows on the Cu atoms of the relaxed structure of the stoichiometric CuO(111) shown in Figure 6.1 (b). The other possibilities of magnetic ordering were studied in detail in the paper by Hu et al.[141]

The CuO(111) surface has two kinds of geometrically different oxygen atoms (Figure 6.1b): those that are coordinated with three Cu atoms on the surface and one Cu atom on the subsurface, denoted  $O_4^{\text{surf}}$ , and those which are only coordinated with three surface Cu atoms, denoted  $O_3^{\text{surf}}$ .  $O_4^{\text{surf}}$  atoms are more exposed on the surface compared to  $O_3^{\text{surf}}$ . The four coordinated Cu atoms, denoted  $Cu_4^{\text{surf}}$ , are coordinated to four oxygen atoms within the plane of the surface. Three-fold Cu atoms, denoted  $Cu_3^{\text{surf}}$ , are coordinated with  $O_3^{\text{surf}}$  and  $O_4^{\text{surf}}$  atoms on the surface and one  $O_3^{\text{surf}}$  atom of the subsurface. All the oxygen atoms in the subsurface are four coordinated, bonding with the three Cu atom in the plane, and with either one surface (upwards) or sub-subsurface Cu atom (downwards) and we denote these atoms  $O_u^{\text{sub}}$  and  $O_d^{\text{sub}}$  respectively. The distinction between  $O_3^{\text{surf}}$ ,  $O_4^{\text{surf}}$ ,  $O_u^{\text{sub}}$  and  $O_d^{\text{sub}}$  ions is important, as they behave very differently during the reduction of the CuO(111) surface.

### 6.2.2 Oxygen vacancies on CuO(111) surface

Removing neutral oxygen atoms so as to create oxygen vacancies is the simplest way to investigate how CuO can be reduced to metallic copper. The magnitude of the oxygen vacancy formation energy plays a crucial role in this process: if the formation energy of oxygen vacancies is too high then desorption of oxygen into vacuum will not be favourable. To this end, we consider different coverages ( $\theta$ ) of surface, subsurface and a mixture of surface–subsurface oxygen vacancies on a  $(2 \times 1)$  surface supercell of the CuO(111) surface. This gives insight into the energetics of formation

## 6. The Reduction Of CuO To Metallic Copper

---

of metallic copper during the reduction process. In the following subsections, we discuss each coverage in turn – ranging from  $\theta = \frac{1}{4}$  oxygen vacancies (removal of one oxygen per cell) to  $\theta = 1$  oxygen vacancies at the surface (removal of four oxygen per cell).

### 6.2.2.1 $\theta = \frac{1}{4}$ oxygen vacancy

Since there are two types of oxygen atoms in the surface–subsurface of CuO(111), we consider two types of oxygen vacancy each for surface and subsurface, namely,  $V_{O_3^{\text{surf}}}$  and  $V_{O_4^{\text{surf}}}$  on the surface by removing three-fold  $O_3^{\text{surf}}$  and four-fold  $O_4^{\text{surf}}$  coordinated surface oxygen atoms, and  $V_{O_u^{\text{sub}}}$  and  $V_{O_d^{\text{sub}}}$  on the subsurface by removing up-bonded  $O_u^{\text{sub}}$  and down-bonded  $O_d^{\text{sub}}$  oxygen atoms (see Figure 6.1b). The oxygen vacancy formation energies are calculated using equation (6.1), and are listed from left to right in Table 6.1 according to the energetic preference. We can see that both DFT + U and HSE06 predict that the structure with subsurface  $V_{O_u^{\text{sub}}}$  vacancy is energetically more favourable than the structure with surface  $V_{O_3^{\text{surf}}}$  vacancy by 0.34 (GGA +U) and 0.48 eV (HSE06). The preference for subsurface oxygen vacancy over the surface oxygen vacancy was also found for CeO<sub>2</sub>(111).[138] The second most stable structure is the structure with  $V_{O_3^{\text{surf}}}$  vacancy and has computed formation energy of 3.02 eV by GGA + U and 2.77 eV by HSE06. This is not surprising because  $O_3^{\text{surf}}$  is under-coordinated. This is energetically more favourable than the structure with  $V_{O_4^{\text{surf}}}$  vacancy, which has a formation energy of 3.52 eV by GGA + U and 3.27 eV by HSE06. While GGA + U produces the same formation energies of 3.52 eV for  $V_{O_4^{\text{surf}}}$  and  $V_{O_d^{\text{sub}}}$  vacancies, HSE06 predicts that  $V_{O_d^{\text{sub}}}$  has a slightly smaller formation energy than  $V_{O_4^{\text{surf}}}$ . Surprisingly then, removal of subsurface  $V_{O_u^{\text{sub}}}$  is most



## 6. The Reduction Of CuO To Metallic Copper

---

favoured whereas removal of subsurface  $V_{O_d^{\text{sub}}}$  is least favoured at  $\Theta = 1/4$ . This may be due to the limited relaxation of sub-surface Cu below  $V_{O_d^{\text{sub}}}$  in contrast to the substantial relaxation observed for Cu above  $V_{O_u^{\text{sub}}}$ . The magnitude of the vacancy formation energy indicates that the stoichiometric CuO(111) surface is quite stable under conditions of high  $O_2$  pressure, where  $\mu_{O_2} = E(O_2)$ . Nevertheless, a comparison of the computed energies with those of well-known reducible metal oxide surfaces such as CeO<sub>2</sub>(111)[143] and TiO<sub>2</sub>(110),[144] indicates that the CuO(111) surface can be classed as reducible.

Table 6.1. Oxygen vacancy formation energies  $E_{\text{vac}}$  in eV for CuO(111) surface with a surface and subsurface oxygen vacancy ( $\theta = \frac{1}{4}$ ) calculated using GGA + U and HSE06. The energetic preference decreases from left to right.

Method	$V_{O_u^{\text{sub}}}$	$V_{O_3^{\text{surf}}}$	$V_{O_d^{\text{sub}}}$	$V_{O_4^{\text{surf}}}$
GGA + U	2.68	3.02	3.52	3.52
HSE06	2.29	2.77	3.09	3.27

To check size effects in the surface supercell, we also calculated  $E_{\text{vac}}$  in a  $(2 \times 2)$  supercell expansion using GGA + U. The calculated  $E_{\text{vac}}$  is 2.91 eV for  $V_{O_3^{\text{surf}}}$  and 3.16 eV for  $V_{O_4^{\text{surf}}}$  on the  $(2 \times 2)$ -CuO(111) surface with  $\theta = \frac{1}{4}$  oxygen vacancy. A  $(2 \times 2)$ -CuO(111) surface with a  $\theta = \frac{1}{4}$  oxygen vacancy concentration has  $E_{\text{vac}}$  of 2.58 eV for the structure with two  $V_{O_3^{\text{surf}}}$  and 2.91 eV for the structure with two  $V_{O_4^{\text{surf}}}$ . The relative stability of  $V_{O_u^{\text{sub}}} > V_{O_3^{\text{surf}}} > V_{O_d^{\text{sub}}} > V_{O_4^{\text{surf}}}$  at  $\theta = \frac{1}{4}$  oxygen vacancies in  $(2 \times 1)$  supercell remains as the cell size increases. Thus we use the  $(2 \times 1)$  supercell expansion of CuO(111) for the further calculations.

## 6. The Reduction Of CuO To Metallic Copper

We also performed test calculations to investigate the effect of  $U$  for the Cu 3d states on the energetic preferences of the oxygen vacancies. We found that the energetic preference of the different oxygen vacancies at  $\Theta = 1/4$  in Table 6.1 remains irrespective of the value of  $U$  ( $U = 0, 3, 5.2, 7$  and  $9$  eV). From these test calculations, we conclude that using  $U = 7$  eV in our calculations not only yields an electronic structure reasonably consistent with experiment, but that the energetic properties are also consistently described.

Figure 6.3 shows the relaxed structures of CuO(111) with the  $O_3^{\text{surf}}$ ,  $O_4^{\text{surf}}$ ,  $O_u^{\text{sub}}$  and  $O_d^{\text{sub}}$  vacancy along with the stoichiometric CuO(111) surface. The corresponding changes in Bader charge for Cu are shown relative to the stoichiometric surface; changes in the charges on the O atoms are negligible. A surface  $\text{Cu}^{2+}$  cation in stoichiometric CuO(111) has a computed Bader charge of 9.90 electrons. The  $\text{Cu}^+$  cation in  $\text{Cu}_2\text{O}$  bulk has computed Bader charge of 10.46 electrons, and hence a change in the charge of 0.5–0.6 electron is indicative of reduction from  $\text{Cu}^{2+}$  to  $\text{Cu}^+$ .

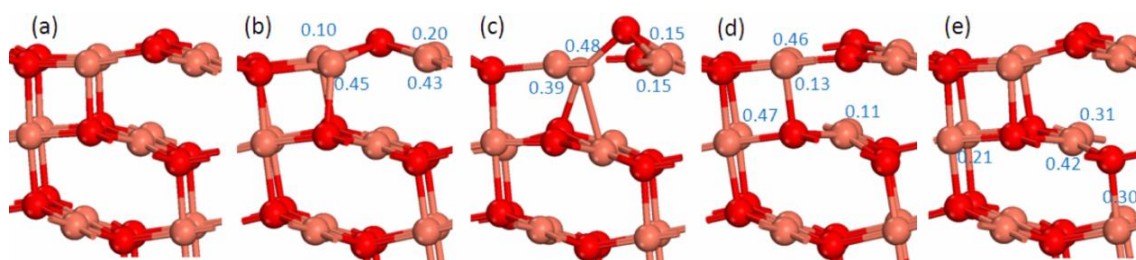


Figure 6.3. Optimized structures of  $(2 \times 1)$ -CuO(111) surface with an oxygen vacancy on the surface and subsurface at  $\Theta = 1/4$ . (a) Stoichiometric CuO(111) (b)  $V_{O_3^{\text{surf}}}$  (c)  $V_{O_4^{\text{surf}}}$  (d)  $V_{O_u^{\text{sub}}}$  (e)  $V_{O_d^{\text{sub}}}$ . Changes in Bader charge (e-) relative to (a) are shown for Cu atoms.

From the relaxed structure of  $V_{O_u^{\text{sub}}}$  (Figure 6.3d), it is noteworthy that one of the surface  $O_3^{\text{surf}}$  atoms is significantly shifted downward. The surface  $\text{Cu}_3^{\text{surf}}$  and subsurface  $\text{Cu}_4^{\text{surf}}$  bordering the vacancy gain 0.46 and 0.47 electrons, respectively,

## 6. The Reduction Of CuO To Metallic Copper

---

which can be assigned as  $\text{Cu}^+$ . After relaxing the CuO(111) surface with  $V_{\text{O}_3^{\text{surf}}}$ , the remaining  $\text{O}_3^{\text{surf}}$  atom moves toward the vacancy site and migrates outwards, making bonds to  $\text{Cu}_4^{\text{surf}}$  atoms which also migrate toward the  $\text{O}_3^{\text{surf}}$  atom (Figure 6.3b). The bond length  $\text{Cu}_4^{\text{surf}}-\text{O}_3^{\text{surf}}$ , which was 2.73 Å before reduction, shortens by 0.7 Å. One  $\text{Cu}_3^{\text{surf}}$  and one  $\text{Cu}_4^{\text{surf}}$  atom on the surface each gains about 0.4 electrons after removal of the oxygen, indicating that in terms of formal oxidation states, these  $\text{Cu}^{2+}$  are reduced to approximately  $\text{Cu}^+$  in the presence of the  $\text{O}_3^{\text{surf}}$  vacancy. The surface structure with  $V_{\text{O}_4^{\text{surf}}}$  is more distorted compared to the one with  $V_{\text{O}_3^{\text{surf}}}$  (Figure 6.3c). One  $\text{O}_3^{\text{surf}}$  atom is substantially shifted upward and the distance between the other  $\text{O}_3^{\text{surf}}$  and  $\text{Cu}_4^{\text{surf}}$  atoms becomes shorter. Two  $\text{Cu}_4^{\text{surf}}$  atoms move toward  $\text{O}_3^{\text{surf}}$  atoms, and the distance between  $\text{Cu}_4^{\text{surf}}$  and  $\text{O}_3^{\text{surf}}$  is shortened slightly from 1.86 Å to 1.82 Å. Two  $\text{Cu}_3^{\text{surf}}$  atoms gain 0.39 and 0.48 electrons, which we again assign as reduced  $\text{Cu}^+$ . One of the  $\text{O}_u^{\text{sub}}$  atoms moves toward the vacancy site in the relaxed structure with  $V_{\text{O}_d^{\text{sub}}}$  (Figure 6.3e). While one subsurface  $\text{Cu}_3^{\text{surf}}$  atom gains 0.42 electrons, one subsurface Cu and one sub-subsurface Cu atom each gains 0.3 electron. The difference between the calculated Bader charge of these reduced Cu atoms after vacancy formation on the CuO(111) surface and a  $\text{Cu}^+$  ion in bulk  $\text{Cu}_2\text{O}$  is between 0.05 to 0.15 electrons, so that the assignment of these ions as  $\text{Cu}^+$  is reasonable. The computed spin magnetization on the reduced Cu ions is 0, consistent with formation of a  $\text{Cu}^+$  ion with a closed 3d shell.

### 6.2.2.2 $\theta = \frac{1}{2}$ oxygen vacancy

Upon removal of half of the oxygen atoms in surface–subsurface or the same number from both surface and subsurface, a number of different vacancy pairs can be

## 6. The Reduction Of CuO To Metallic Copper

---

formed in the  $(2 \times 1)$ . We can remove two  $O_3^{\text{surf}}/O_u^{\text{sub}}$  or two  $O_4^{\text{surf}}/O_d^{\text{sub}}$  atoms, or remove one  $O_3^{\text{surf}}$  and one  $O_4^{\text{surf}}$  from surface–subsurface. We can also remove one  $O_3^{\text{surf}}$  or  $O_4^{\text{surf}}$  atom from the surface and one  $O_u^{\text{sub}}$  or  $O_d^{\text{sub}}$  from subsurface. The vacancy formation energies of the vacancy pairs are computed relative to the surface with one oxygen vacancy present, and are listed in Table 6.2. The structure with  $V_{O_u^{\text{sub}}} + V_{O_d^{\text{sub}}}$ , which has the formation energy  $E_{\text{vac}}$  of 1.74 eV relative to  $V_{O_u^{\text{sub}}}$  and 0.89 relative to  $V_{O_d^{\text{sub}}}$ , is energetically most favourable compared to the other structures. The second most stable structure with a vacancy pair is the structure with  $V_{O_3^{\text{surf}}} + V_{O_4^{\text{surf}}}$ . The  $V_{O_3^{\text{surf}}} + V_{O_4^{\text{surf}}}$  vacancy pair can be obtained either by removing an  $O_3^{\text{surf}}$  atom from the structure with  $V_{O_4^{\text{surf}}}$  ( $E_{\text{vac}} = 1.77$  eV) or by removing an  $O_4^{\text{surf}}$  atom from the structure with  $V_{O_3^{\text{surf}}}$  ( $E_{\text{vac}} = 1.27$  eV). Figure 6.4(a) and (b) shows these two most stable structures with an oxygen vacancy pair, along with the Cu Bader charges relative to the perfect CuO(111) surface and the energies ( $\Delta E$ ) relative to the most stable structure. Other combinations of surface and subsurface oxygen vacancy pairs are not as energetically favourable. The less stable structures and their formation energies are displayed in Figure 6.5(a–h) and Table 6.3.

Table 6.2 Oxygen vacancy formation energies for  $\Theta=1/2$  relative to the existing oxygen vacancies  $\Theta=1/4$  for CuO(111) surface calculated using GGA + U.

Reduction path	$E_{\text{vac}}$ (eV)
(1) $V_{O_3^{\text{surf}}} \rightarrow 2V_{O_3^{\text{surf}}}$	3.43
(2) $V_{O_3^{\text{surf}}} \rightarrow V_{O_3^{\text{surf}}} + V_{O_4^{\text{surf}}}$	1.77
(3) $V_{O_4^{\text{surf}}} \rightarrow 2V_{O_4^{\text{surf}}}$	3.01
(4) $V_{O_4^{\text{surf}}} \rightarrow V_{O_3^{\text{surf}}} + V_{O_4^{\text{surf}}}$	1.27
(5) $V_{O_u^{\text{sub}}} \rightarrow 2V_{O_u^{\text{sub}}}$	2.43
(6) $V_{O_u^{\text{sub}}} \rightarrow V_{O_u^{\text{sub}}} + V_{O_d^{\text{sub}}}$	1.74
(7) $V_{O_d^{\text{sub}}} \rightarrow 2V_{O_d^{\text{sub}}}$	2.88

## 6. The Reduction Of CuO To Metallic Copper

(8) $V_{O_d^{sub}} \rightarrow V_{O_u^{sub}} + V_{O_d^{sub}}$	0.89
(9) $V_{O_3^{surf}} \rightarrow V_{O_3^{surf}} + V_{O_d^{sub}}$	3.38
(10) $V_{O_3^{surf}} \rightarrow V_{O_3^{surf}} + V_{O_u^{sub}}$	2.66
(11) $V_{O_4^{surf}} \rightarrow V_{O_4^{surf}} + V_{O_u^{sub}}$	2.42
(12) $V_{O_4^{surf}} \rightarrow V_{O_4^{surf}} + V_{O_d^{sub}}$	2.97

Table 6.3. Oxygen vacancy formation energies for less stable structures relative to the most stable structures for  $\Theta=1/2$ ,  $\Theta=3/4$  and  $\Theta=1$  on CuO(111) surface calculated using GGA + U.

structure	$\Delta E$ (eV)
$\Theta=1/2$	
$2V_{O_3^{surf}}$	2.03
$2V_{O_4^{surf}}$	2.11
$2V_{O_u^{sub}}$	0.69
$2V_{O_d^{sub}}$	1.98
$V_{O_3^{surf}} + V_{O_u^{sub}}$	1.26
$V_{O_4^{surf}} + V_{O_d^{sub}}$	2.07
$V_{O_4^{surf}} + V_{O_u^{sub}}$	1.51
$V_{O_3^{surf}} + V_{O_d^{sub}}$	1.98
$\Theta=3/4$	
$2V_{O_3^{surf}} + V_{O_4^{surf}}$	1.09
$V_{O_3^{surf}} + 2V_{O_4^{surf}}$	0.70
$V_{O_3^{surf}} + V_{O_4^{surf}} + V_{O_u^{sub}}$	0.39
$\Theta=1$	
$2V_{O_3^{surf}} + 2V_{O_4^{surf}}$	1.86

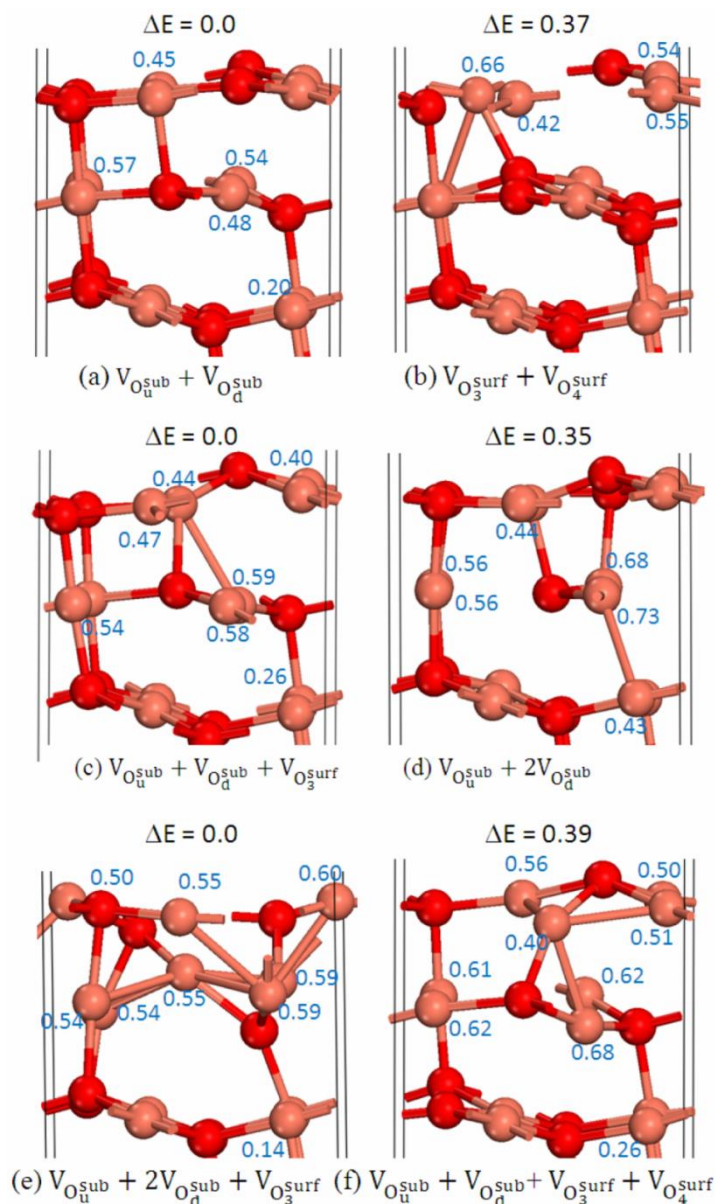


Figure 6.4. Optimized structures of  $(2 \times 1)$ -CuO(111) surface with different oxygen vacancy coverage. Changes in Bader charge ( $e^-$ ) relative to (a) in Fig. 3 are shown for Cu atoms. (a) and (b) for  $\Theta = \frac{1}{2}$ , (c) and (d) for  $\Theta = \frac{3}{4}$ , (e) and (f) for  $\Theta = 1$ . The energies ( $\Delta E$ ) relative to the most stable structure of each coverage are given on top of each subfigure in eV.

From the Bader charges shown in Figure 6.4 (a), it can be seen that three subsurface Cu atoms and one surface Cu atom in the  $V_{O_u}^{\text{sub}} + V_{O_d}^{\text{sub}}$  each gains 0.4–0.6 electrons. Figure 6.4(b) shows that four surface Cu atoms in the  $V_{O_3}^{\text{surf}} + V_{O_4}^{\text{surf}}$  structure gain 0.4–0.7 electrons, which are close to the calculated value of the

## 6. The Reduction Of CuO To Metallic Copper

Bader charge on  $\text{Cu}^+$  in  $\text{Cu}_2\text{O}$  bulk. The distances between the remaining O and reduced Cu atoms in the surface and subsurface are 1.84–1.89 Å, which are close to the calculated Cu–O distance of 1.85 Å in  $\text{Cu}_2\text{O}$  bulk. This shows that four  $\text{Cu}^{2+}$  ions at and near the surface are formally reduced overall to four  $\text{Cu}^+$  ions by the presence of a vacancy pair. Furthermore, we can conclude that the reduction process  $4\text{Cu}^{2+} \rightarrow 4\text{Cu}^+$  is more favourable than the competing reduction process whereby the existing  $\text{Cu}^+$  species from the single vacancy are further reduced to  $\text{Cu}^0$ .

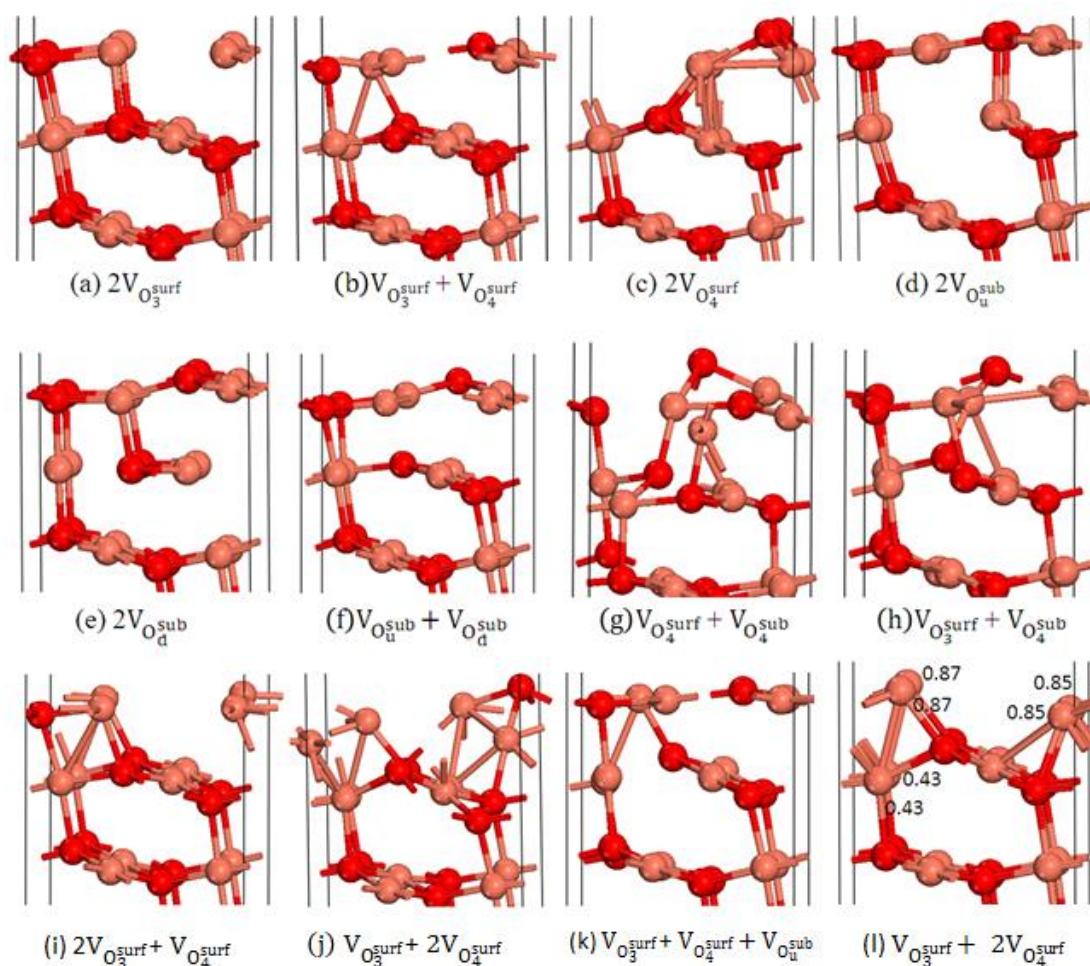


Figure 6.5. Optimized structures of less stable structures with  $\Theta=1/2$ ,  $\Theta=3/4$  and  $\Theta=1$ .

**6.2.2.3  $\Theta = \frac{3}{4}$  and  $\Theta = 1$  oxygen vacancy**

Two types of triple oxygen vacancy ( $\Theta = \frac{3}{4}$ ) can be obtained by removing two  $O_3^{\text{surf}}/O_{\text{u}}^{\text{sub}}$  and one  $O_4^{\text{surf}}/O_{\text{d}}^{\text{sub}}$  atoms or two  $O_4^{\text{surf}}/O_{\text{d}}^{\text{sub}}$  and one  $O_3^{\text{surf}}/O_{\text{u}}^{\text{sub}}$  atoms from the surface–subsurface. The mixed surface–subsurface oxygen vacancies at  $\Theta = \frac{3}{4}$  concentration are also taken into account. The most stable vacancy structure at  $\Theta = \frac{3}{4}$  is the structure with  $V_{O_{\text{u}}^{\text{sub}}} + V_{O_{\text{d}}^{\text{sub}}} + V_{O_3^{\text{surf}}}$ , as shown in Figure 6.4(c). The vacancy formation energy relative to  $V_{O_{\text{u}}^{\text{sub}}} + V_{O_{\text{d}}^{\text{sub}}}$  is 2.60 eV. From the relative Bader charges shown in Figure 6.4(c), it can be seen that three  $\text{Cu}^{2+}$  ions in the subsurface and three surface  $\text{Cu}^{2+}$  gain around 0.5–0.6 electrons, indicating that these ions are reduced to six  $\text{Cu}^+$ . The second most stable oxygen vacancy configuration at  $\Theta = \frac{3}{4}$  is the structure with  $V_{O_{\text{u}}^{\text{sub}}} + 2V_{O_{\text{d}}^{\text{sub}}}$ , which is less stable than the  $V_{O_{\text{u}}^{\text{sub}}} + V_{O_{\text{d}}^{\text{sub}}} + V_{O_3^{\text{surf}}}$  structure by 0.35 eV. (See Figure 6.4(d)). Four  $\text{Cu}^{2+}$  ions in the subsurface layer around the vacancies gain 0.6–0.7 electrons and extend their Cu–O bond lengths to 1.84–1.93 Å. Two other  $\text{Cu}^{2+}$  ions are reduced by 0.4 electrons, so that overall  $6\text{Cu}^{2+}$  are reduced to  $\text{Cu}^+$ .

It can be seen that, as is the case at  $\Theta = \frac{1}{4}$  and  $\Theta = \frac{1}{2}$  coverages, the reduction process  $\text{Cu}^{2+} \rightarrow \text{Cu}^+$  continues to be preferred over the the reduction of existing  $\text{Cu}^+$  to metallic  $\text{Cu}^0$ . We also see that layer by layer reduction of the CuO(111) surface is not favoured during the vacuum annealing since the structure with a mixture of surface and subsurface vacancies is more favourable than a configuration with  $\Theta = \frac{3}{4}$  vacancies in a single layer. Energetically less favourable oxygen vacancy configurations at  $\Theta = \frac{3}{4}$  have also been studied (see Figure 6.5(i–k)).



## 6. The Reduction Of CuO To Metallic Copper

---

Upon further removal of the oxygen atoms from the surface or subsurface, a coverage of oxygen vacancies equivalent to a full layer ( $\theta = 1$ ) is reached. The mixture of surface–subsurface vacancies can be obtained by removing three from the subsurface and one from the surface, or removing two from each of the surface and the subsurface. Figure 6.4(e) and (f) shows the first and second most energetically preferred configurations at the vacancy concentration  $\theta = 1$ . The most stable structure has  $V_{O_u^{\text{sub}}} + 2V_{O_d^{\text{sub}}} + V_{O_3^{\text{surf}}}$ . The vacancy formation energy relative to  $V_{O_u^{\text{sub}}} + V_{O_d^{\text{sub}}} + V_{O_3^{\text{surf}}}$  is 1.61 eV. All eight  $\text{Cu}^{2+}$  ions per cell in the surface and subsurface are reduced to the  $\text{Cu}^+$  as evidenced by the gain in net Bader charge of 0.5 to 0.6 electrons. The second most stable structure is the combination of two of the most favourable oxygen vacancies at  $\theta = \frac{1}{2}$  e.g.  $V_{O_u^{\text{sub}}} + V_{O_d^{\text{sub}}} + V_{O_3^{\text{surf}}} + V_{O_4^{\text{surf}}}$ . In this case, all the  $\text{Cu}^{2+}$  ions have gained around 0.5–0.7 electrons, indicating again that all the  $\text{Cu}^{2+}$  ions are now reduced to  $\text{Cu}^+$  ions. Although the complete reduction of the surface layer  $\text{Cu}^{2+}$  to metallic  $\text{Cu}^0$  is possible, the calculation shows that the  $2V_{O_3^{\text{surf}}} + 2V_{O_4^{\text{surf}}}$  vacancy is not energetically favourable (see Figure 6.51).

We conclude that the oxygen vacancy mechanism is not sufficient to describe how  $\text{CuO}(111)$  is reduced to metallic Cu, because the reduction process of  $\text{Cu}^{2+} \rightarrow \text{Cu}^+$  is energetically preferred over the reduction of  $\text{Cu}^+$  to metallic  $\text{Cu}^0$ . We therefore suppose that  $\text{Cu}^0$  can only be formed when the diffusion of oxygen to the surface is kinetically limited, or when the entire sample has transformed into  $\text{Cu}_2\text{O}$ .

Summarising the above, the subsurface oxygen vacancy  $V_{O_u^{\text{sub}}}$  is found to be energetically more favoured than three coordinated oxygen vacancy  $V_{O_3^{\text{surf}}}$  at  $\theta = \frac{1}{4}$ . The subsurface oxygen vacancy pair  $V_{O_u^{\text{sub}}} + V_{O_d^{\text{sub}}}$  is found to be the most stable

## 6. The Reduction Of CuO To Metallic Copper

---

structure at  $\theta = \frac{1}{2}$ . Mixture of surface and subsurface oxygen vacancies are energetically preferred over the structures with a fully reduced monolayer at  $\theta = \frac{3}{4}$  and  $\theta = 1$ . Our analysis of step-wise oxygen vacancy formation can explain how the CuO(111) surface is reduced. The energetics of oxygen vacancy formation are such that at the temperatures in the experiments of ref [128], oxygen vacancy formation will take place and our results show that in all oxygen vacancy coverages,  $\text{Cu}^{2+} \rightarrow \text{Cu}^+$  is energetically preferred over  $\text{Cu}^+ \rightarrow \text{Cu}^0$ , and therefore  $\text{Cu}_2\text{O}$  is an intermediate state prior to being fully reduced to metallic  $\text{Cu}^0$ .

### 6.2.2.4 *Ab initio atomistic thermodynamics of oxygen vacancies on CuO(111) surface*

In order to estimate the temperature for the oxygen vacancy formation on the CuO(111) surface, ab initio atomistic thermodynamics is used to calculate the surface free energy  $\gamma$ . Using equation (6.6) and (6.7), we calculate the surface free energy  $\gamma(T,P)$  of the CuO(111) surface for different oxygen vacancy coverages as a function of the O atomic chemical potential (Figure 6.6). The dependence of the oxygen chemical potential is translated into a temperature scale at an oxygen pressure of  $P = 10^{-8}$  Torr (which would be a typical vacuum pressure in experimental work) using the standard thermodynamic tables.<sup>36</sup> From Figure 6.6 we can see that the surface free energy  $\gamma$  increases significantly with an increase of oxygen vacancy concentration and that the stoichiometric surface is energetically favourable even under oxygen-poor conditions. This means that the reduction process is not spontaneous and that stronger reducing conditions than vacuum annealing are needed. Notice that the  $\Theta = \frac{1}{2}$  oxygen vacancy structure  $V_{\text{O}_{\text{u}}^{\text{sub}}} + V_{\text{O}_{\text{d}}^{\text{sub}}}$  is relatively low in energy and becomes more stable than  $V_{\text{O}_{\text{u}}^{\text{sub}}}$  under oxygen-poor condition. This implies

## 6. The Reduction Of CuO To Metallic Copper

that subsurface  $\text{Cu}_2\text{O}$  is an intermediate state during the reduction process, and  $\text{CuO}$  may reduce to  $\text{Cu}_2\text{O}$  before it is directly reduced to metallic  $\text{Cu}$ .

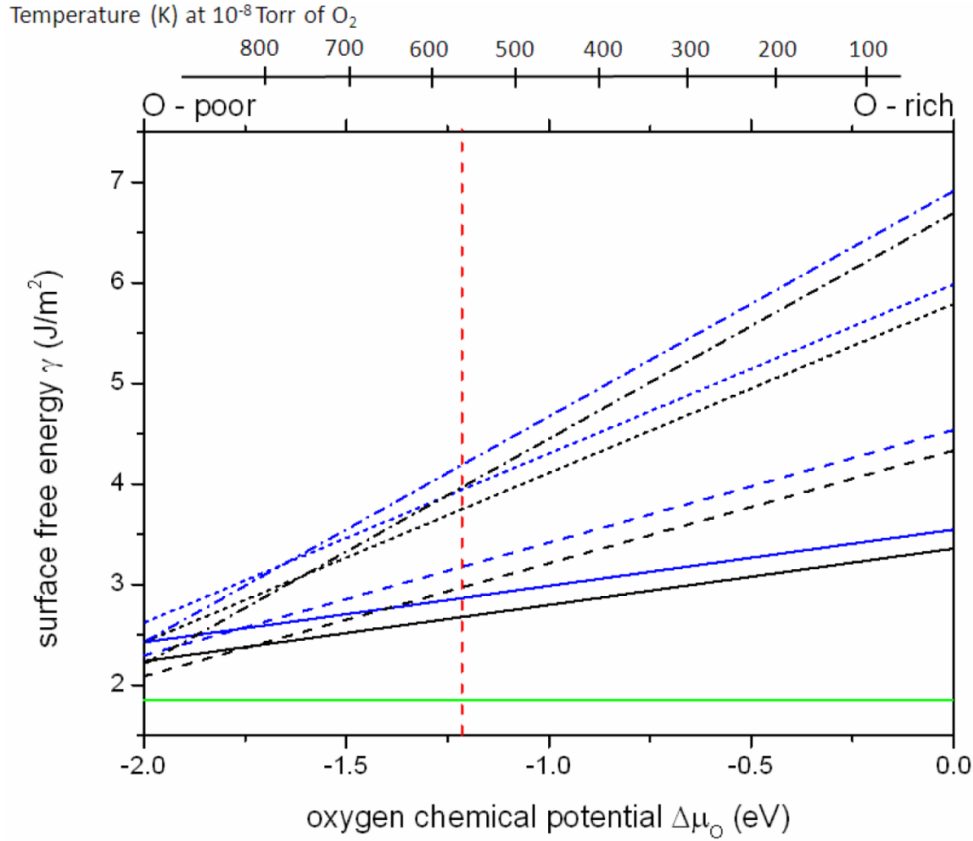


Figure 6.6. surface free energy  $\gamma(T, P = 10^{-8} \text{ Torr})$  of  $\text{CuO}(111)$  surfaces with different oxygen vacancy coverage as a function of oxygen chemical potential relative to  $\frac{1}{2}E(\text{O}_2)$ . Solid lines are for  $\theta = \frac{1}{4}$  oxygen vacancy coverage; black line:  $V_{\text{O}_{\text{u}}^{\text{sub}}}$ , blue line:  $V_{\text{O}_{3}^{\text{surf}}}$ . Dash lines are for  $\theta = \frac{1}{2}$  oxygen vacancy, black:  $V_{\text{O}_{\text{u}}^{\text{sub}}} + V_{\text{O}_{\text{d}}^{\text{sub}}}$ , blue:  $V_{\text{O}_{3}^{\text{surf}}} + V_{\text{O}_{4}^{\text{surf}}}$ . Short dashed lines are for  $\theta = \frac{3}{4}$  oxygen vacancy; black:  $V_{\text{O}_{\text{u}}^{\text{sub}}} + V_{\text{O}_{\text{d}}^{\text{sub}}} + V_{\text{O}_{3}^{\text{surf}}}$  and blue:  $V_{\text{O}_{\text{u}}^{\text{sub}}} + 2V_{\text{O}_{\text{d}}^{\text{sub}}}$ . Dash dot lines are for  $\theta = 1$  oxygen vacancy; black:  $V_{\text{O}_{\text{u}}^{\text{sub}}} + 2V_{\text{O}_{\text{d}}^{\text{sub}}} + V_{\text{O}_{3}^{\text{surf}}}$  and blue:  $V_{\text{O}_{\text{u}}^{\text{sub}}} + V_{\text{O}_{\text{d}}^{\text{sub}}} + V_{\text{O}_{3}^{\text{surf}}} + V_{\text{O}_{4}^{\text{surf}}}$ . Green dash line is for stoichiometric  $\text{CuO}(111)$  surface. Vertical red dashed line shows the chemical potential of oxygen in bulk  $\text{Cu}_2\text{O}$ .

Thus we also calculated the formation energy of  $\text{Cu}_2\text{O}$  using the definition  $h_{\text{Cu}_2\text{O}} = \mu_{\text{Cu}_2\text{O}} - 2\mu_{\text{Cu}} - \mu_{\text{O}}$ , where  $\mu_{\text{Cu}_2\text{O}}$  is the energy of bulk  $\text{Cu}_2\text{O}$ . The

## 6. The Reduction Of CuO To Metallic Copper

---

calculation gives  $h_{\text{Cu}_2\text{O}} = -1.24$  eV, which is very close to the previous calculation.[145] From the calculated formation energy of bulk  $\text{Cu}_2\text{O}$ , we derive a temperature of about 540 K ( $P = 10^{-8}$  Torr) for the conversion of CuO into  $\text{Cu}_2\text{O}$  (shown with vertical dashed line in Figure 6.6). Lee et al. reported the reduction of CuO to  $\text{Cu}_2\text{O}$  at 473 K and reduction of CuO to metallic Cu at 673 K through vacuum annealing at a pressure of  $10^{-8}$  Torr.[128] Our calculated result is thus consistent with the experimentally measured conditions under which CuO is reduced to  $\text{Cu}_2\text{O}$ . An error bar for the temperature in the range of 100–200 K is due to the translation of an uncertainty of the vacancy formation energy of a few tenths of an eV from the DFT calculations.[146]

### 6.2.3 $\text{H}_2$ adsorption on CuO(111) surfaces

Reduction of transition metal oxides with  $\text{H}_2$  has been used to grow thin metallic films. In this section, we study the reaction of  $\text{H}_2$  with the CuO(111) surface as a model of the initial stages in  $\text{H}_2$  reduction of CuO. Since accommodating four  $\text{H}_2$  molecules per  $(2 \times 1)$  cell simultaneously at the surface is not favourable, we focus on the more reasonable route of sequential adsorption of  $\text{H}_2$  on the CuO(111) surface, until a full layer of surface oxygen is removed. We assume that  $\text{H}_2$  cannot react directly with subsurface oxygen, although O atoms can presumably diffuse to the surface and create subsurface vacancies (Section 6.2.2).

#### 6.2.3.1 *Sequential adsorption of $\text{H}_2$ on CuO(111) surface*

For the first  $\text{H}_2$  molecule, there are two different adsorption sites,  $\text{O}_4^{\text{surf}}$  and  $\text{O}_3^{\text{surf}}$ . The calculated adsorption energy  $\Delta E_{\text{ads}}$  of  $\text{H}_2$  on  $\text{O}_4^{\text{surf}}$  is 0.02 eV, which indicates that there is no reaction of  $\text{H}_2$  on the  $\text{O}_4^{\text{surf}}$  site. However, the adsorption of  $\text{H}_2$  on the  $\text{O}_3^{\text{surf}}$  site is quite exothermic with a gain of  $\Delta E_{\text{ads}} = -0.82$  eV at  $T = 0$  K. Consistent

## 6. The Reduction Of CuO To Metallic Copper

---

with our oxygen vacancy calculation, this is because  $O_3^{\text{surf}}$  is more reactive than  $O_4^{\text{surf}}$  (Section 6.2.2). The relaxed atomic structure of  $H_2$  on the  $O_3^{\text{surf}}$  site is shown in Figure 6.7(a). Oxygen  $O_3^{\text{surf}}$  is pulled out of the surface upon reaction with  $H_2$  to form a water molecule. The distance between this oxygen atom and H is about 1.0 Å and the angle H–O–H is 107.5°, typical of the water molecule. The distance between the O atom in the water molecule and the nearest Cu is 1.99 Å, which is notably longer than the Cu–O distance in the CuO(111) surface layer. The desorption energy of the formed water molecule from the surface is  $\Delta E_{\text{des}} = 0.78$  eV. If the desorption energy is positive, additional thermal energy is needed to break the bond between O in  $H_2O$  and the surface Cu atom. Thus, the dissociative adsorption of a  $H_2$  molecule on the  $O_3^{\text{surf}}$  site on CuO(111) leads to spontaneous formation of a water molecule and partial reduction of the CuO(111) surface. However desorption of water from the surface is not spontaneous at  $T = 0$  K, and elevated temperature is needed to desorb water. Bader charge analysis of  $H_2$  adsorption on the  $O_3^{\text{surf}}$  site shows that one  $Cu_3^{\text{surf}}$  and one  $Cu_4^{\text{surf}}$  atom on the surface gain 0.4 and 0.2 electrons, respectively, indicating that  $H_2$  adsorption on the CuO(111) surface can reduce two  $Cu^{2+}$  ions to  $Cu^+$ , which is consistent with the reduction process observed in Section. 4.1 for oxygen vacancy formation.

## 6. The Reduction Of CuO To Metallic Copper

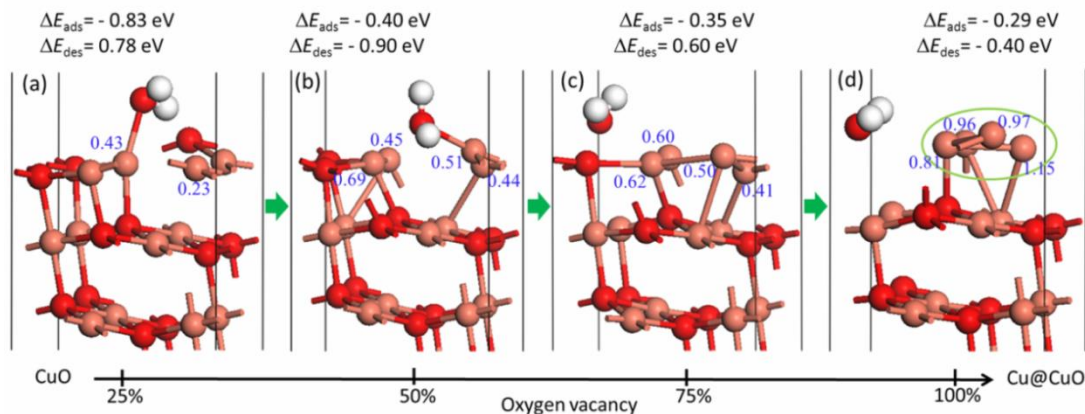


Figure 6.7. Structure of the CuO(111) surface after successive adsorption of each H<sub>2</sub> molecule and formation of water. The adsorption energy of H<sub>2</sub> on the surface ( $\Delta E_{\text{ads}}$ ) and desorption energy of water from the surface ( $\Delta E_{\text{des}}$ ) are shown on the top of each subfigure. The arrows in green represent the removal of formed water molecule and introducing another H<sub>2</sub> on the partially reduced surface. The arrow in the bottom indicates the trend of reduction. Changes in Bader charge (e<sup>-</sup>) relative to Figure 6.3 are shown for Cu atoms in the top layer.

The next H<sub>2</sub> adsorption on the partially reduced CuO(111) surface with  $\Theta = \frac{1}{4}$  oxygen vacancy takes place after removing the formed H<sub>2</sub>O molecule. The calculated adsorption energy  $\Delta E_{\text{ads}}$  of this H<sub>2</sub> molecule on the remaining O<sub>3</sub><sup>surf</sup> is  $-0.40 \text{ eV}$  (Figure 6.7(b)). The angle H–O–H is  $106.6^\circ$  and the H–O distance is  $0.98 \text{ \AA}$ . The distance between O in water and the nearest surface Cu is  $2.00 \text{ \AA}$ . This indicates that another water molecule formed spontaneously on the partially reduced surface. The change in Bader charge on surface Cu is shown in Figure 6.7(b). Two Cu<sub>4</sub><sup>surf</sup> atoms gain 0.7 and 0.4 electrons and the other two Cu<sub>3</sub><sup>surf</sup> atoms gain 0.5 and 0.4 electrons after the second H<sub>2</sub> is introduced to the surface, indicating further reduction of Cu. The Cu–O distance is shortened from  $1.95 \text{ \AA}$  to  $1.84 \text{ \AA}$  for each of Cu<sub>3</sub><sup>surf</sup> and Cu<sub>4</sub><sup>surf</sup> atoms. This implies that all the Cu<sup>2+</sup> are reduced to Cu<sup>+</sup>. During this step we can conclude that the Cu<sup>2+</sup> → Cu<sup>+</sup> process is spontaneous in the presence of reducing agent H<sub>2</sub>. In this

## 6. The Reduction Of CuO To Metallic Copper

---

case, the desorption energy  $\Delta E_{\text{des}}$  is negative, and no thermal effect is needed to remove the water molecule from the surface.

The  $\text{O}_4^{\text{surf}}$  atoms on the stoichiometric CuO(111) surface are initially not reactive to the  $\text{H}_2$  molecule. However, the third  $\text{H}_2$  molecule reacts with an  $\text{O}_4^{\text{surf}}$  atom at the surface when they are two  $V_{\text{O}_{\text{surf}}}$  because it is shifted upward and  $\text{Cu}-\text{O}_3^{\text{surf}}$  bond is weakened (Figure 6.7(c)). This indicates that the reactivity of the CuO(111) surface increases with the presence of oxygen vacancies. A water molecule is formed with an adsorption energy of  $\Delta E_{\text{ads}} = -0.35$  eV, which is weaker compared to adsorption on  $\text{O}_3^{\text{surf}}$  because  $\text{O}_4^{\text{surf}}$  has a higher coordination number and is less favourable to remove. The desorption of the water molecule is not favoured in this case (the desorption energy is positive). The distance between the O in  $\text{H}_2\text{O}$  molecule and the Cu atom is 3.09 Å. The H–O distances in  $\text{H}_2\text{O}$  are 0.98 and 0.99 Å, and the H–O–H angle is 109.6°. The  $\text{Cu}_4^{\text{surf}}$  atoms gain 0.6 electrons, while other  $\text{Cu}_3^{\text{surf}}$  atoms gain 0.4 and 0.5 electrons, respectively. The distance between the  $\text{Cu}_4^{\text{surf}}$  that gains 0.6 electron and  $\text{O}_3^{\text{surf}}$  is 2.61 Å, which is very close to bulk Cu–Cu distance. The Cu–O distance on the surface is about 1.84 to 1.90 Å. From the above Bader charge and the structure analysis, we conclude that metallic copper species start to be formed at this coverage of  $\Theta = 3/4$  oxygen vacancies in a single layer, and other  $\text{Cu}^{2+}$  ions are reduced to  $\text{Cu}^+$ , so that  $\text{Cu}^0$  and  $\text{Cu}^+$  co-exist on this surface.

Finally, the interaction of  $\text{H}_2$  with the last surface oxygen atom  $\text{O}_4^{\text{surf}}$  which is shifted upward by the adsorption of previous  $\text{H}_2$ , gives formation of a water molecule with an adsorption energy of  $-0.29$  eV (Figure 6.7(d)) It is of note that the  $\text{H}_2$  adsorption energies  $\Delta E_{\text{ads}}$  on the CuO(111) surface with different oxygen vacancies are all negative, which shows that the reduction of the surface is energetically

favoured. The Cu–Cu distance on the surface is in the range of 2.4 to 2.8 Å, compared to 2.55 Å in bulk Cu metal. The change in the Bader charge on Cu surface atoms in Figure 6.7(d) indicates that full reduction of the surface  $\text{Cu}^{2+}$  ions to metallic  $\text{Cu}^0$  takes place, as seen for  $\Theta = 1$  vacancies in the surface layer (Figure 6.5). From the Bader charges shown in Figure 6.7, we can conclude that indirect reduction of  $\text{CuO} \rightarrow \text{Cu}_2\text{O} \rightarrow \text{Cu}$  is again dominant over direct reduction  $\text{CuO} \rightarrow \text{Cu}$ , which is consistent with our oxygen vacancy calculations and the experimental results.<sup>17</sup>

### 6.2.4 Ab initio atomistic thermodynamics of $\text{H}_2$ adsorption on

#### **CuO(111) surface**

To understand the structural stability and effect of temperature during the reduction of the CuO(111) surface with  $\text{H}_2$ , we again apply ab initio thermodynamics using equation (6.6) and (6.7). Figure 6.8 shows the surface free energy  $\gamma$  of CuO(111) surfaces with the different percentage of oxygen vacancies for each sequential adsorption of  $\text{H}_2$  as a function of oxygen chemical potential  $\mu_{\text{O}}$  at 1 bar of  $\text{O}_2$  pressure. By drawing a vertical line through the point where the horizontal black dashed line (stoichiometric CuO(111) surface) and the red line ( $\Theta = 1/2$  vacancies) cross, we know that  $\text{Cu}^{2+}$  ions on the CuO(111) surface start reducing to  $\text{Cu}^+$  at circa 360 K. This process continues until the temperature goes up to 780 K where the green line ( $\Theta = 1$  reduced CuO(111) surface) crosses the red line. Therefore a  $\text{Cu}_2\text{O}$  to metallic copper transition occurs on the surface at this point, and metallic Cu islands form on CuO, as highlighted in Figure 6.7(d). Rodriguez et al. observed the reduction of CuO to  $\text{Cu}_2\text{O}$  with low  $\text{H}_2$  flow at atmospheric  $\text{H}_2$  pressure and elevated temperature 423–673 K using in situ time-resolved XRD technique,<sup>16</sup> which is consistent with Figure 6.8.



## 6. The Reduction Of CuO To Metallic Copper

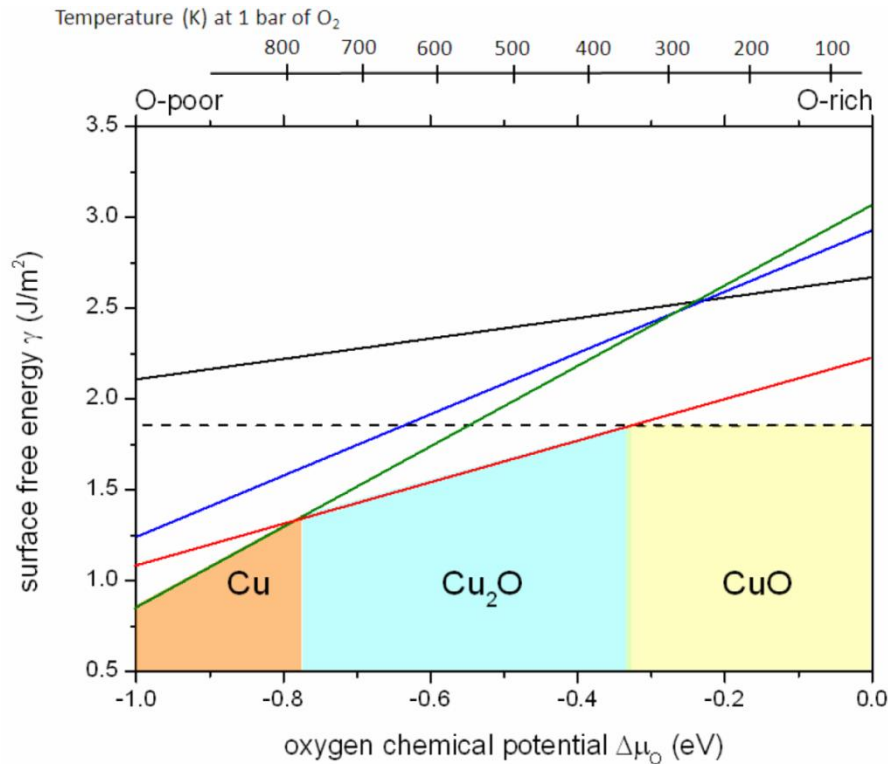


Figure 6.8. Surface free energy  $\gamma$  of CuO(111) surfaces with different oxygen vacancies in the presence of  $H_2$  as the function of oxygen chemical potential  $\Delta\mu_O$ . Black:  $\Theta = 1/4$ , red:  $\Theta = 1/2$ , blue:  $\Theta = 3/4$ , green:  $\Theta = 1$ . Black dashed line: stoichiometric CuO(111) surface.

By juxtaposing Figure 6.6 with Figure 6.8 which are both obtained from ab initio atomistic thermodynamics studies, one should notice that Figure 6.8 corresponds to the continuation of the left-hand-side of Figure 6.6 because the O-poor condition in reduction of the surface with oxygen vacancy is the O-rich condition for the reduction of the surface with  $H_2$  adsorption. It can be seen that the lines with the same percentage of oxygen vacancies are parallel in these two figures. Thus we can compare these two figures and can come to the conclusion that reduction of the CuO(111) surface to metallic Cu is energetically difficult to achieve without a reducing agent. The horizontal line in Figure 6.6, which corresponds to the stoichiometric CuO(111) surface, lies under all the other lines, even at the oxygen-poor condition. However in Figure 6.8, this line is crossed by the red line ( $\Theta = 1/2$  O vacancies) at  $\Delta\mu_O = -0.33$

## 6. The Reduction Of CuO To Metallic Copper

eV and by the green line ( $\Theta = 1$  O vacancies) at  $\Delta\mu_{\text{O}} = -0.77$  eV. This indicates that the CuO(111) surface can be reduced by H<sub>2</sub> to Cu<sub>2</sub>O and finally to metallic Cu. It should also be noticed that the extreme left-hand-side of Figure 6.8 corresponds to the reduction energies of CuO(111) with H<sub>2</sub> that are calculated using equation (6.4) and are in line with the data in Figure 6.7.

Figure 6.6 spans the range of the reduction of the bulk phase CuO because the Cu and the CuO bulk energies are used to obtain the lower and higher limit of oxygen chemical potential  $\mu_{\text{O}}$ . The range of oxygen chemical potential  $\mu_{\text{O}}$  in Figure 6.8 is derived from the condition where the CuO(111) surface is reduced with H<sub>2</sub>. We have found surface structures that correspond to the mixtures of oxidation states expected under the same conditions in the bulk, namely, Cu<sup>2+</sup> and Cu<sup>+</sup> at  $\Theta = 1/4$  vacancy coverages and Cu<sup>+</sup> and Cu<sup>0</sup> at  $\Theta = 3/4$ . However, as shown in Figure 6.6 and Figure 6.8, these mixtures are not as stable as exclusively Cu<sup>2+</sup> or Cu<sup>+</sup> or a Cu<sup>0</sup>.

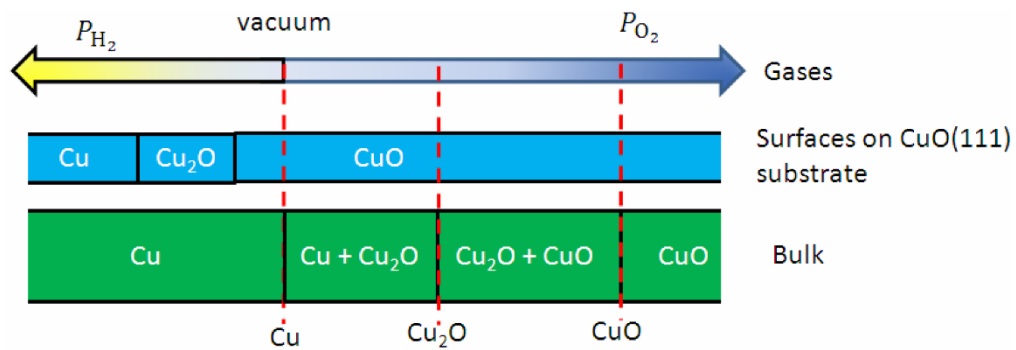


Figure 6.9. Schematic phase diagram of CuO(111) reduction to metallic Cu under different oxygen and H<sub>2</sub> pressures. Green and blue colours represent bulk and surface, respectively.

Combining the ideas of Figure 6.6 and Figure 6.8, we obtain a schematic phase diagram for the reduction of CuO(111) surface to metallic Cu with and without H<sub>2</sub> reducing agent, as shown in Figure 6.9. The vertical dashed red lines approximately

show the formation energies of the bulk  $\text{Cu}_2\text{O}$  and  $\text{CuO}$  by which the  $\text{H}_2$  pressures are obtained. Figure 6.9 shows that different processes are needed for bulk and surface reduction, i.e. reducing the  $\text{O}_2$  pressure is adequate for bulk reduction, but applying  $\text{H}_2$  is needed for surface reduction. From Figure 6.9, we can see that the bulk  $\text{CuO}$  is reduced to the mixture of  $\text{CuO}$  and  $\text{Cu}_2\text{O}$  as the oxygen pressure decreases, then to the mixture of  $\text{Cu}_2\text{O}$  and  $\text{Cu}^0$  near vacuum conditions. The surface  $\text{CuO}$  needs a stronger reduction condition compared to the reduction of bulk  $\text{CuO}$ . The surface  $\text{CuO}$  transforms to  $\text{Cu}_2\text{O}$  with the application of  $\text{H}_2$  and eventually to metallic  $\text{Cu}$  with increased  $\text{H}_2$  pressure. This implies that the surface oxides protect the underlying bulk from reduction during vacuum annealing. Applying the reducing agent  $\text{H}_2$  can significantly facilitate the reduction of  $\text{CuO}$ .

A future step would be to study how subsurface oxygen can diffuse to the surface and re-oxidise it, in competition with reducing by  $\text{H}_2$ , thus generating deeper subsurface oxygen vacancies (section 6.2.2).

### 6.3 Conclusion

In conclusion, we studied two mechanisms for the reduction of  $\text{CuO}(111)$  surface, namely oxygen vacancies from vacuum annealing and  $\text{H}_2$  adsorption. Oxygen vacancy calculations reveal that removal of a subsurface  $\text{O}_\text{u}^\text{sub}$  atom is energetically more favourable than removal of under-coordinated  $\text{O}_3^\text{surf}$  at  $\theta = \frac{1}{4}$ . The subsurface oxygen vacancy pair  $V_{\text{O}_\text{u}^\text{sub}} + V_{\text{O}_\text{d}^\text{sub}}$  is found to be the most stable structure at  $\theta = \frac{1}{2}$ . The mixture of surface–subsurface vacancies is found to be more favourable than a single layer oxygen vacancies at  $\theta = \frac{3}{4}$  and  $\theta = 1$ . The reduction process  $\text{Cu}^{2+} \rightarrow \text{Cu}^{1+}$  is found to be more favoured than the process  $\text{Cu}^{1+} \rightarrow \text{Cu}^0$  at all the vacancy

## 6. The Reduction Of CuO To Metallic Copper

---

concentrations, indicating that vacuum annealing is not sufficient to reduce oxide to metal during indirect ALD. The calculation of sequential adsorption of  $H_2$  on the CuO(111) surface shows that  $H_2$  adsorption initially takes place on the  $O_3^{\text{surf}}$  site, giving a water molecule and the partially reduced surface. Subsequent adsorption of  $H_2$  fully reduces the surface and gives water molecules. Comparing the results from ab initio atomistic thermodynamics for the two mechanisms, we conclude that CuO bulk is protected from reduction during vacuum annealing by the CuO surface and that  $H_2$  is required in order to reduce that surface. Thus, different processes are needed for bulk and surface reduction, i.e. reducing the  $O_2$  pressure is adequate for bulk reduction, but applying  $H_2$  is needed for surface reduction. For indirect ALD processes, these results show that the strength of reducing agent is important to obtain fully reduced metal thin films.

## 7 Conclusions

### 7.1 Summary

Overall, this thesis is dedicated to understand by means of density functional calculations the surface chemistry and reaction mechanisms of depositing copper through the atomic layer deposition technique.

The surface energy of  $\text{SiO}_2$  and the  $\text{Cu}/\text{SiO}_2$  interface energy are dependent on the surface composition of  $\text{SiO}_2$ , e.g. number of reactive oxygen atoms, and hydroxyl groups. Thus we used *ab initio* atomistic thermodynamics to relate the level of interface oxygen at the  $\text{Cu}/\text{SiO}_2$  interface as the function of oxygen chemical potential. From this the interface phase diagram as a function of oxygen pressure and temperature is obtained, which allows us to understand the effect of pressure and temperature on thin film deposition process. It is found that the interfacial oxide  $\text{Cu}_2\text{O}$  phases prefer high oxygen pressure and low temperature while the silicide phases are stable at low oxygen pressure and high temperature for  $\text{Cu}/\text{SiO}_2$  interface, which is in good agreement with experimental observations.

Although the ALD mechanisms of oxide materials have been investigated well in literature, ALD processes of Cu and other metals are not well understood. In chapter 4, we studied the adsorption of two common precursors,  $\text{Cu}(\text{dmap})_2$  and  $\text{Cu}(\text{acac})_2$  molecules, on different sites on Cu surfaces using DFT with various levels of treatment of vdW forces. It is found that the vdW forces are crucial to describe the precursor – substrate interaction. The adsorption energies and geometries are found to be sensitive toward the method of including vdW interaction in DFT. In both cases,

## 7. Conclusions

---

the precursors undergo partial decomposition and the adsorbate Cu atoms are partially reduced.

For  $\text{Cu}(\text{dmap})_2$  adsorption, we found that the pure PBE and the vdW-DF2 methods yield  $\text{Cu}(\text{dmap})_2$  chemisorbed selectively at one Cu(111) surface site, while the PBE-D3 method yields chemisorbed structures on Cu(111) at all adsorption sites. The vdW-optB88 functional predicts a chemisorbed structure for three out of four adsorption sites and physisorption for one site, with a relatively large energy for physisorption. For the rough surfaces, all the methods with and without additional vdW forces predict that the molecule chemisorbs on the Cu(332) step and Cu(643) kink. The breaking of Cu–N or Cu–O bonds as  $\text{Cu}(\text{dmap})_2$  chemisorbs shows that metal–ligand bonds are broken cleanly during the early stage of Cu ALD, making the molecule reactive to the co-reagent in Cu ALD reactions without unwanted impurities of C, H, O or N. Charge redistribution occurred between the O–Cu–O unit of the molecule and the Cu surface.

For  $\text{Cu}(\text{acac})_2$  adsorption, PBE predicts a chemisorbed structure on the diagonal site and physisorbed structures on hollow and top sites. The vdW-optB88 method gives chemisorbed structure in all three adsorption sites on the Cu(111) surface. In the diagonal site, the  $\text{Cu}(\text{acac})_2$  molecule is attached to the surface through the carbon – surface bond. This would lead to the deposition of CuO or  $\text{Cu}_2\text{O}$  rather than Cu metal. Thus, the formation of the carbon in ligand to surface when the Cu precursor adsorbs on the surface is detrimental to the Cu ALD, as it leads to the decomposition of the ligands.

In conclusion, studying the adsorption of precursor molecules on the surface can provide useful information to understand the surface chemistry during ALD. From the precursor adsorption studies, we can draw the following conclusions for precursors.

## 7. Conclusions

---

1. The Cu atom and the atoms coordinated directly to the Cu in precursor should form bonds to the surface. The formation of bonds between other ligand atoms (except the atoms coordinated to the Cu) and the surface may lead to impurity.

2. Clean cleavage of the ligand–metal bond is one of the requirements for selecting precursors for ALD of metals. Scission of bonds within the ligands may result in undesired surface reaction.

Based on the detailed studies of the precursor adsorption on the surface, we further study the reaction of this chemisorbed precursor with the reducing agent  $\text{Et}_2\text{Zn}$ , based on the seminal work done by Lee et al. [Angew. Chemie Int. Ed. **2009**, 48, 4536–4539]. We propose two different reaction pathways based on activation energies and reaction energies for a range of surface reactions. We find that the chemisorbed  $\text{Cu}(\text{dmap})_2$  decomposes through breaking one or both Cu–O on Cu(111) after the first ALD pulse. Butane formation and the migration of ethyl groups to the surface are two possible routes for the decomposed  $\text{Et}_2\text{Zn}$  after its adsorption on the Cu(111) surface saturated with the decomposed  $\text{Cu}(\text{dmap})_2$ . In the first case, the butane formation/desorption is followed by the diffusion and reordering of dmap ligands around the Zn atom to form the  $\text{Zn}(\text{dmap})_2$  molecule. In the second case, the dmap ligands diffuse and re-order around Zn atom. The  $\text{Zn}(\text{dmap})_2$  is then formed and desorbs in the presence of ethyl groups, which is followed by butane formation and desorption with the assistance of a migrating Cu atom. The butane formation and desorption steps are extremely exothermic, which means that the originally proposed ALD process is possible. However, the diffusion and re-ordering steps are endothermic which make the reaction rates of reverse reactions higher than the

## 7. Conclusions

---

forward reactions. This may lead to very slow growth rate, as was the case in the experimental work.

As the direct ALD method to deposit copper faces many challenge, indirect ALD which uses more than two steps emerged as more promising because of its ability to enhance the growth rate and lower the ALD temperature. In order to understand the reduction steps of indirect ALD, we studied two mechanisms for the reduction of the CuO(111) surface, namely oxygen vacancies from vacuum annealing and H<sub>2</sub> adsorption in chapter 6. The reduction process  $\text{Cu}^{2+} \rightarrow \text{Cu}^{1+}$  is found to be more favoured than the process  $\text{Cu}^{1+} \rightarrow \text{Cu}^0$  at all the vacancy concentrations, indicating that vacuum annealing is not sufficient to reduce oxide to metal during indirect ALD. The calculation of sequential adsorption of H<sub>2</sub> on the CuO(111) surface shows that H<sub>2</sub> adsorption initially takes place on the three-coordinated O atom, giving a water molecule and the partially reduced surface. Subsequent adsorption of H<sub>2</sub> fully reduces the surface and gives water molecules. Comparing the results from ab initio atomistic thermodynamics for the two mechanisms, we conclude that CuO bulk is protected from reduction during vacuum annealing by the CuO surface and that H<sub>2</sub> is required in order to reduce that surface. Thus, different processes are needed for bulk and surface reduction, i.e. reducing the O<sub>2</sub> pressure is adequate for bulk reduction, but applying H<sub>2</sub> is needed for surface reduction. For indirect ALD processes, these results show that the role of reducing agent is important to obtain fully reduced metal thin films.

### 7.2 Future work and outlook

In our future work, we would describe the nucleation of copper on various substrates to understand if it is possible to achieve uniform and continuous 2 nm copper thin film with atomic layer deposition. The main difficulties in this task is how



to describe a mesoscopic stress between copper and substrate based on ab initio method.

In chapter 5, we omitted the effect of corrections to the vdW interactions on the activation energies and reaction energies. It is clear from chapter 4 that vdW interaction has an important role on correctly describing the precursor adsorption. However, it is not clear how vdW interactions impact on the reaction mechanism. We expect that the overall reaction mechanism that we proposed in chapter 5 would not change with the inclusion of vdW interaction. Thus, we will in the future check this by studying energetics across the reaction mechanism of Cu ALD in chapter 5 with the vdW-inclusive DFT method.

Through this thesis, we made progress to understanding the atomistic origin of Cu ALD process. However, the surface chemistry and the reaction mechanisms of ALD of other transition metals are not understood yet. We can expand the methods in this thesis to study the ALD of other metals.

## Bibliography

- [1] Ritala M and Niinisto J 2009 Chapter 4 Atomic Layer Deposition *Chemical Vapour Deposition: Precursors* (The Royal Society of Chemistry) pp 158–206
- [2] George S M 2010 Atomic layer deposition: An overview *Chem. Rev.* **110** 111–31
- [3] Pinna N and Knez M 2012 *Atomic Layer Deposition of Nanostructured Materials* (Wiley-VCH)
- [4] Hwang C S and Yoo C Y 2014 *Atomic Layer Deposition for Semiconductors* (New York: Springer)

## 0. Bibliography

---

- [5] Kim H, Lee H-B-R and Maeng W J 2009 Applications of atomic layer deposition to nanofabrication and emerging nanodevices *Thin Solid Films* **517** 2563–80
- [6] Miikkulainen V, Leskelä M, Ritala M and Puurunen R L 2013 Crystallinity of inorganic films grown by atomic layer deposition: Overview and general trends *J. Appl. Phys.* **113** 021301
- [7] Osada T and Godwin M 1999 International Technology Roadmap for Semiconductors
- [8] Rosenberg R, Edelstein D C, Hu C K and Rodbell K P 2000 Copper metallization for high performance silicon technology *Annu. Rev. Mater. Sci.* **30** 229–62
- [9] Shacham-Diamand Y, Inberg A, Sverdlov Y, Bogush V, Croitoru N, Moscovich H and Freeman A 2003 Electroless processes for micro- and nanoelectronics *Electrochimica Acta* vol 48 pp 2987–96
- [10] Krisyuk V, Aloui L, Prud'homme N, Sysoev S, Senocq F, Samélor D and Vahlas C 2011 CVD of Pure Copper Films from Amidinate Precursor *Electrochem. Solid-State Lett.* **14** D26–9
- [11] Vidjayacoumar B, Emslie D J H, Clendenning S B, Blackwell J M, Britten J F and Rheingold A 2010 Investigation of AlMe<sub>3</sub>, BEt<sub>3</sub>, and ZnEt<sub>2</sub> as Co-Reagents for Low-Temperature Copper Metal ALD/Pulsed-CVD *Chem. Mater.* **22** 4844–53
- [12] Lee H B, Hwang K J, Nam J W, Lee U S, Kim J T, Koo S-M, Baunemann A, Fischer A R and Sung M M 2009 Low-Temperature Atomic Layer Deposition of Copper Metal Thin Films: Self-Limiting Surface Reaction of Copper Dimethylamino-2-propoxide with Diethylzinc *Angew. Chemie Int. Ed.* **48** 4536–9
- [13] Lampe-Önnerud C, Jansson U, Hårsta A and Carlsson J-O 1992 Chemical vapour deposition of copper on Si(111) and SiO<sub>2</sub> substrates *J. Cryst. Growth* **121** 223–34
- [14] Mårtensson P and Carlsson J-O 1997 Atomic Layer Epitaxy of Copper on Tantalum *Chem. Vap. Depos.* **3** 45–50
- [15] Törndahl T, Ottosson M and Carlsson J-O 2004 Growth of copper metal by atomic layer deposition using copper(I) chloride, water and hydrogen as precursors *Thin Solid Films* **458** 129–36
- [16] Utriainen M, Kröger-Laukkanen M, Johansson L-S and Niinistö L 2000 Studies of metallic thin film growth in an atomic layer epitaxy reactor using M(acac)<sub>2</sub> (M=Ni, Cu, Pt) precursors *Appl. Surf. Sci.* **157** 151–8

## 0. Bibliography

---

- [17] Lim B S, Rahtu A and Gordon R G 2003 Atomic layer deposition of transition metals *Nat. Mater.* **2** 749–54
- [18] Jezewski C, Lanford W A, Wiegand C J, Singh J P, Wang P-I, Senkevich J J and Lu T-M 2005 Inductively Coupled Hydrogen Plasma-Assisted Cu ALD on Metallic and Dielectric Surfaces *J. Electrochem. Soc.* **152** C60–4
- [19] Niskanen A, Rahtu A, Sajavaara T, Arstila K, Ritala M and Leskelä M 2005 Radical-Enhanced Atomic Layer Deposition of Metallic Copper Thin Films *J. Electrochem. Soc.* **152** G25–8
- [20] Li Z, Rahtu A and Gordon R G 2006 Atomic Layer Deposition of Ultrathin Copper Metal Films from a Liquid Copper(I) Amidinate Precursor *J. Electrochem. Soc.* **153** C787–94
- [21] Vidjayacoumar B, Emslie D J H, Blackwell J M, Clendenning S B and Britten J F 2010 Solution Reactions of a Bis(pyrrolylaldiminate)copper(II) Complex with Peralkyl Zinc, Aluminum, and Boron Reagents: Investigation of the Pathways Responsible for Copper Metal Deposition *Chem. Mater.* **22** 4854–66
- [22] Knisley T J, Ariyasena T C, Sajavaara T, Saly M J and Winter C H 2011 Low Temperature Growth of High Purity, Low Resistivity Copper Films by Atomic Layer Deposition *Chem. Mater.* **23** 4417–9
- [23] Kalutarage L C, Clendenning S B and Winter C H 2014 Low-Temperature Atomic Layer Deposition of Copper Films Using Borane Dimethylamine as the Reducing Co-reagent *Chem. Mater.* **26** 3731–8
- [24] Hagen D J, Connolly J, Nagle R, Povey I M, Rushworth S, Carolan P, Ma P and Pemble M E 2013 Plasma enhanced atomic layer deposition of copper: A comparison of precursors *Surf. Coatings Technol.* **230** 3–12
- [25] Hagen D J, Povey I, Rushworth S, Wrench J S, Keeney L, Schmidt M, Petkov N, Barry S T, Coyle J P and Pemble M E 2014 Atomic Layer Deposition of Cu Using a Carbene-Stabilized Cu (I) Silylamide *J. Mater. Chem. C* 9205–14
- [26] Wu L and Eisenbraun E 2008 Effects of Hydrogen Plasma Treatments on the Atomic Layer Deposition of Copper *Electrochem. Solid-State Lett.* **11** H107–10
- [27] Dai M, Kwon J, Halls M D, Gordon R G and Chabal Y J 2010 Surface and Interface Processes during Atomic Layer Deposition of Copper on Silicon Oxide *Langmuir* **26** 3911–7
- [28] Moon D-Y, Han D-S, Shin S-Y, Park J-W, Kim B M and Kim J H 2011 Effects of the substrate temperature on the Cu seed layer formed using atomic layer deposition *Thin Solid Films* **519** 3636–40
- [29] Coyle J P, Dey G, Sirianni E R, Kemell M L, Yap G P A, Ritala M, Leskelä M, Elliott S D and Barry S T 2013 Deposition of Copper by Plasma-Enhanced

## 0. Bibliography

---

- Atomic Layer Deposition Using a Novel N-Heterocyclic Carbene Precursor  
*Chem. Mater.* **25** 1132–8
- [30] Christensen S T, Feng H, Libera J L, Guo N, Miller J T, Stair P C and Elam J W 2010 Supported Ru–Pt Bimetallic Nanoparticle Catalysts Prepared by Atomic Layer Deposition *Nano Lett.* **10** 3047–51
- [31] Tan T L, Wang L-L, Johnson D D and Bai K 2012 A comprehensive search for stable Pt-Pd nanoalloy configurations and their use as tunable catalysts. *Nano Lett.* **12** 4875–80
- [32] Lu J, Low K-B, Lei Y, Libera J A, Nicholls A, Stair P C and Elam J W 2014 Toward atomically-precise synthesis of supported bimetallic nanoparticles using atomic layer deposition *Nat Commun* **5**
- [33] Kariniemi M, Niinistö J, Hatanpää T, Kemell M, Sajavaara T, Ritala M and Leskelä M 2011 Plasma-Enhanced Atomic Layer Deposition of Silver Thin Films *Chem. Mater.* **23** 2901–7
- [34] Kwon J, Saly M, Halls M D, Kanjolia R K and Chabal Y J 2012 Substrate Selectivity of (tBu-Allyl)Co(CO)<sub>3</sub> during Thermal Atomic Layer Deposition of Cobalt *Chem. Mater.* **24** 1025–30
- [35] Mackus A J M, Garcia-Alonso D, Knoops H C M, Bol A A and Kessels W M M 2013 Room-Temperature Atomic Layer Deposition of Platinum *Chem. Mater.* **25** 1769–74
- [36] Hanbucken J A V and G D T S and M 1984 Nucleation and growth of thin films *Reports Prog. Phys.* **47** 399
- [37] Elliott S D and Greer J C 2004 Simulating the atomic layer deposition of alumina from first principles *J. Mater. Chem.* **14** 3246–50
- [38] Mukhopadhyay A B, Musgrave C B and Fdez Sanz J 2008 Atomic layer deposition of hafnium oxide from hafnium chloride and water. *J. Am. Chem. Soc.* **130** 11996–2006
- [39] Tanskanen J T and Bent S F 2013 Insights into the Surface Chemistry of Tin Oxide Atomic Layer Deposition from Quantum Chemical Calculations *J. Phys. Chem. C* **117** 19056–62
- [40] Shirazi M and Elliott S D 2013 Multiple Proton Diffusion and Film Densification in Atomic Layer Deposition Modeled by Density Functional Theory *Chem. Mater.* **25** 878–89
- [41] Martin R M 2004 *Electronic Structure: Basic Theory and Practical Methods* (Cambridge University Press)
- [42] Wills J, Alouani M and Andersson P 2010 Density Functional Theory and the Kohn–Sham Equation *Full-Potential Electronic Structure Method* (Springer)

## 0. Bibliography

---

- [43] Hohenberg P and Kohn W 1964 Inhomogeneous Electron Gas *Phys. Rev.* **136** B864–71
- [44] Kohn W and Sham L J 1965 Self-Consistent Equations Including Exchange and Correlation Effects *Phys. Rev.* **140** 1133 – &
- [45] Von Barth U and Hedin L 1972 A local exchange-correlation potential for the spin polarized case. *J. Phys. C Solid State Phys.* **5** 1629
- [46] Perdew J P, Burke K and Ernzerhof M 1996 Generalized Gradient Approximation Made Simple *Phys. Rev. Lett.* **77** 3865–8
- [47] Anisimov V I, Aryasetiawan F and Lichtenstein A I 1997 First-principles calculations of the electronic structure and spectra of strongly correlated systems: the LDA + U method *J. Phys. Condens. Matter* **9** 767
- [48] Kittel C 1986 *Introduction to Solid State Physics* (New York: John Wiley & Sons, Inc.)
- [49] Perdew J P, Burke K and Ernzerhof M 1997 Erratum: Generalized Gradient Approximation Made Simple *Phys. Rev. Lett.* **78** 1396
- [50] Tkatchenko A, Romaner L, Hofmann O T, Zojer E, Ambrosch-Draxl C and Scheffler M 2011 Van der Waals Interactions Between Organic Adsorbates and at Organic/Inorganic Interfaces *MRS Bull.* **35** 435–42
- [51] Grimme S 2006 Semiempirical GGA-type density functional constructed with a long-range dispersion correction *J. Comput. Chem.* **27** 1787–99
- [52] Grimme S 2011 Density functional theory with London dispersion corrections *Wiley Interdiscip. Rev. Mol. Sci.* **1** 211–28
- [53] Grimme S, Antony J, Ehrlich S and Krieg H 2010 A consistent and accurate ab initio parametrization of density functional dispersion correction (DFT-D) for the 94 elements H-Pu *J. Chem. Phys.* **132** 154104–19
- [54] Jurečka P, Černý J, Hobza P and Salahub D R 2007 Density functional theory augmented with an empirical dispersion term. Interaction energies and geometries of 80 noncovalent complexes compared with ab initio quantum mechanics calculations *J. Comput. Chem.* **28** 555–69
- [55] Dion M, Rydberg H, Schroder E, Langreth D C and Lundqvist B I 2004 van der Waals density functional for general geometries *Phys. Rev. Lett.* **92** 246401
- [56] Klimeš J, Bowler D R and Michaelides A 2010 Chemical accuracy for the van der Waals density functional. *J. physics. Condens. matter* **22** 022201
- [57] Klimeš J, Bowler D R and Michaelides A 2011 Van der Waals density functionals applied to solids *Phys. Rev. B* **83** 195131

## 0. Bibliography

---

- [58] Richard F. W. Bader 1994 *Atoms in Molecules A Quantum Theory* (Oxford University Press)
- [59] Henkelman G, Arnaldsson A and Jónsson H 2006 A fast and robust algorithm for Bader decomposition of charge density *Comput. Mater. Sci.* **36** 354–60
- [60] Sanville E, Kenny S D, Smith R and Henkelman G 2007 Improved grid-based algorithm for Bader charge allocation *J. Comput. Chem.* **28** 899–908
- [61] Reuter K and Scheffler M 2003 Composition and structure of the RuO<sub>2</sub>(110) surface in an O<sub>2</sub> and CO environment: Implications for the catalytic formation of CO<sub>2</sub> *Phys. Rev. B* **68** 045407
- [62] Rogal J, Reuter K and Scheffler M 2007 CO oxidation at Pd(100): A first-principles constrained thermodynamics study *Phys. Rev. B - Condens. Matter Mater. Phys.* **75** 1–11
- [63] Soon A, Todorova M, Delley B and Stampfl C 2006 Oxygen adsorption and stability of surface oxides on Cu(111): A first-principles investigation *Phys. Rev. B - Condens. Matter Mater. Phys.* **73** 1–12
- [64] Stull D R and Prophet H 1971 *JANAF Thermochemical Tables* (Washington, DC: (US National Bureau of Standards)
- [65] Akolkar R N and Barkey D P 2014 *Copper Electrodeposition for Nanofabrication of Electronics Devices* ed K Kondo, R N Akolkar, D P Barkey and M Yokoi (New York, NY: Springer New York)
- [66] Willis B G and Lang D V. 2004 Oxidation mechanism of ionic transport of copper in SiO<sub>2</sub> dielectrics *Thin Solid Films* **467** 284–93
- [67] Reuter K and Scheffler M 2004 Oxide formation at the surface of late 4d transition metals: Insights from first-principles atomistic thermodynamics *Appl. Phys. A Mater. Sci. Process.* **78** 793–8
- [68] Reuter K and Scheffler M 2001 Composition, structure, and stability of RuO<sub>2</sub>(110) as a function of oxygen pressure *Phys. Rev. B* **65** 35406
- [69] Rogal J, Reuter K and Scheffler M 2004 Thermodynamic stability of PdO surfaces *Phys. Rev. B* **69** 075421
- [70] Li W-X, Stampfl C and Scheffler M 2003 Insights into the function of silver as an oxidation catalyst by ab initio, atomistic thermodynamics 15
- [71] Elliott S D and Greer J C 2011 Structural and energetic origin of defects at the interface between germanium and a high-k dielectric from first principles *Appl. Phys. Lett.* **98** 082904

## 0. Bibliography

---

- [72] Zhu H and Ramprasad R 2011 Effective work function of metals interfaced with dielectrics: A first-principles study of the Pt-HfO<sub>2</sub> interface *Phys. Rev. B - Condens. Matter Mater. Phys.* **83** 1–4
- [73] Zhu H, Tang C and Ramprasad R 2010 Phase equilibria at Si-HfO<sub>2</sub> and Pt-HfO<sub>2</sub> interfaces from first principles thermodynamics *Phys. Rev. B - Condens. Matter Mater. Phys.* **82** 1–10
- [74] Maimaiti Y, Nolan M and Elliott S D 2014 Reduction mechanisms of the CuO(111) surface through surface oxygen vacancy formation and hydrogen adsorption. *Phys. Chem. Chem. Phys.* **16** 3036–46
- [75] Nagao K, Neaton J B and Ashcroft N W 2003 First-principles study of adhesion at Cu/SiO<sub>2</sub> interfaces *Phys. Rev. B* **68** 125403
- [76] Shan T-R, Devine B D, Phillpot S R and Sinnott S B 2011 Molecular dynamics study of the adhesion of Cu/SiO<sub>2</sub> interfaces using a variable-charge interatomic potential *Phys. Rev. B* **83** 115327
- [77] De Los Santos Valladares L, Salinas D H, Dominguez a. B, Najarro D A, Khondaker S I, Mitrelias T, Barnes C H W, Aguiar J A and Majima Y 2012 Crystallization and electrical resistivity of Cu<sub>2</sub>O and CuO obtained by thermal oxidation of Cu thin films on SiO<sub>2</sub>/Si substrates *Thin Solid Films* **520** 6368–74
- [78] Benouattas N, Mosser A, Raiser D, Faerber J and Bouabellou A 2000 Behaviour of copper atoms in annealed Cu/SiO<sub>x</sub>/Si systems *Appl. Surf. Sci.* **153** 79–84
- [79] Dey G and Elliott S D 2012 Mechanism for the Atomic Layer Deposition of Copper Using Diethylzinc as the Reducing Agent: A Density Functional Theory Study Using Gas-Phase Molecules as a Model *J. Phys. Chem. A* **116** 8893–901
- [80] Ma Q, Guo H, Gordon R G and Zaera F 2011 Surface Chemistry of Copper(I) Acetamidates in Connection with Atomic Layer Deposition (ALD) Processes *Chem. Mater.* **23** 3325–34
- [81] Zaera F 2008 The surface chemistry of thin film atomic layer deposition (ALD) processes for electronic device manufacturing *J. Mater. Chem.* **18** 3521–6
- [82] Kim T, Yao Y, Coyle J P, Barry S T and Zaera F 2013 Thermal Chemistry of Cu(I)-Iminopyrrolidinate and Cu(I)-Guanidinate Atomic Layer Deposition (ALD) Precursors on Ni(110) Single-Crystal Surfaces *Chem. Mater.* **25** 3630–9
- [83] Elliott S D 2012 Atomic-scale simulation of ALD chemistry *Semicond. Sci. Technol.* **27** 074008
- [84] Yanagisawa S, Lee K and Morikawa Y 2008 First-principles theoretical study of Alq<sub>3</sub>Al interfaces: origin of the interfacial dipole. *J. Chem. Phys.* **128** 244704

## 0. Bibliography

---

- [85] Kresse G and Furthmüller J 1996 Efficiency of ab-initio total energy calculations for metals and semiconductors using a plane-wave basis set *Comput. Mater. Sci.* **6** 15–50
- [86] Blochl P E 1994 Projector augmented-wave method *Phys. Rev. B* **50** 17953–79
- [87] Ahlrichs R, Bär M, Häser M, Horn H and Kölmel C 1989 Electronic structure calculations on workstation computers: The program system turbomole *Chem. Phys. Lett.* **162** 165–9
- [88] Eichkorn K, Treutler O, Öhm H, Häser M and Ahlrichs R 1995 Auxiliary basis sets to approximate Coulomb potentials *Chem. Phys. Lett.* **240** 283–90
- [89] Eichkorn K, Weigend F, Treutler O and Ahlrichs R 1997 Auxiliary basis sets for main row atoms and transition metals and their use to approximate Coulomb potentials *Theor. Chem. Acc.* **97** 119–24
- [90] Weigend F and Ahlrichs R 2005 Balanced basis sets of split valence, triple zeta valence and quadruple zeta valence quality for H to Rn: Design and assessment of accuracy *Phys. Chem. Chem. Phys.* **7** 3297–305
- [91] Henkelman G, Uberuaga B P and Jonsson H 2000 A climbing image nudged elastic band method for finding saddle points and minimum energy paths *J. Chem. Phys.* **113** 9901–4
- [92] Henkelman G and Jónsson H 2000 Improved tangent estimate in the nudged elastic band method for finding minimum energy paths and saddle points *J. Chem. Phys.* **113** 9978
- [93] Liu W, Tkatchenko A and Scheffler M 2014 Modeling Adsorption and Reactions of Organic Molecules at Metal Surfaces *Acc. Chem. Res.* **47** 3369–77
- [94] Liu W, Ruiz V G, Zhang G-X, Santra B, Ren X, Scheffler M and Tkatchenko A 2013 Structure and energetics of benzene adsorbed on transition-metal surfaces: density-functional theory with van der Waals interactions including collective substrate response *New J. Phys.* **15** 53046
- [95] Yildirim H, Greber T and Kara A 2013 Trends in Adsorption Characteristics of Benzene on Transition Metal Surfaces: Role of Surface Chemistry and van der Waals Interactions *J. Phys. Chem. C* **117** 20572–83
- [96] Toyoda K, Nakano Y, Hamada I, Lee K, Yanagisawa S and Morikawa Y 2009 First-principles study of benzene on noble metal surfaces: Adsorption states and vacuum level shifts *Surf. Sci.* **603** 2912–22
- [97] Liu W, Carrasco J, Santra B, Michaelides A, Scheffler M and Tkatchenko A 2012 Benzene adsorbed on metals: Concerted effect of covalency and van der Waals bonding *Phys. Rev. B - Condens. Matter Mater. Phys.* **86** 1–6



## 0. Bibliography

---

- [98] Carrasco J, Liu W, Michaelides A and Tkatchenko A 2014 Insight into the description of van der Waals forces for benzene adsorption on transition metal (111) surfaces *J. Chem. Phys.* **140** 084704
- [99] Rosa M, Corni S and Di Felice R 2014 van der Waals effects at molecule-metal interfaces *Phys. Rev. B* **90** 125448
- [100] Tonigold K and Groß A 2010 Adsorption of small aromatic molecules on the (111) surfaces of noble metals: A density functional theory study with semiempirical corrections for dispersion effects *J. Chem. Phys.* **132**
- [101] Baran J D and Larsson J A 2013 Theoretical insights into adsorption of cobalt phthalocyanine on Ag(111): A combination of chemical and van der waals bonding *J. Phys. Chem. C* **117** 23887–98
- [102] Baran J D and Larsson J A 2012 Structure and energetics of shuttlecock-shaped tin-phthalocyanine on Ag(111): A density functional study employing dispersion correction *J. Phys. Chem. C* **116** 9487–97
- [103] Grimme S, Ehrlich S and Goerigk L 2011 Effect of the damping function in dispersion corrected density functional theory *J. Comput. Chem.* **32** 1456–65
- [104] Ziambaras E, Kleis J, Schröder E and Hyldgaard P 2007 Potassium intercalation in graphite: A van der Waals density-functional study *Phys. Rev. B* **76** 155425
- [105] Hamada I 2010 A van der Waals density functional study of ice Ih. *J. Chem. Phys.* **133** 214503
- [106] Puzder A, Dion M and Langreth D C 2006 Binding energies in benzene dimers: Nonlocal density functional calculations. *J. Chem. Phys.* **124** 164105
- [107] Tkatchenko A and Scheffler M 2009 Accurate Molecular Van Der Waals Interactions from Ground-State Electron Density and Free-Atom Reference Data *Phys. Rev. Lett.* **102** 73005
- [108] Ruiz V G, Liu W, Zojer E, Scheffler M and Tkatchenko A 2012 Density-Functional Theory with Screened van der Waals Interactions for the Modeling of Hybrid Inorganic-Organic Systems *Phys. Rev. Lett.* **108** 146103
- [109] Lide D 2004 CRC Handbook of chemistry and physics: a ready-reference book of chemical and physical data. Ed. 82 (2001-2002) 2610
- [110] Vanpoucke D E P and Brocks G 2008 Formation of Pt-induced Ge atomic nanowires on Pt/Ge(001): A density functional theory study *Phys. Rev. B* **77** 241308
- [111] Tersoff J and Hamann D R 1985 Theory of the scanning tunneling microscope *Phys. Rev. B* **31** 805–13

- [112] Becker R, Devi A, Weiß J, Weckenmann U, Winter M, Kiener C, Becker H W and Fischer R A 2003 A Study on the Metal Organic CVD of Pure Copper Films from Low Cost Copper(II) Dialkylamino-2-propoxides: Tuning the Thermal Properties of the Precursor by Small Variations of the Ligand *Chem. Vap. Depos.* **9** 149–56
- [113] Franke J-H and Kosov D S 2013 Adsorption of lactic acid on chiral Pt surfaces—a density functional theory study. *J. Chem. Phys.* **138** 084705
- [114] Vollmer S, Birkner A, Lukas S, Witte G and Wöll C 2000 Nanopatterning of copper (111) vicinal surfaces by oxygen-induced mesoscopic faceting *Appl. Phys. Lett.* **76** 2686–8
- [115] Baber A E, Gellman A J, Sholl D S and Sykes E C H 2008 The Real Structure of Naturally Chiral Cu{643} *J. Phys. Chem. C* **112** 11086–9
- [116] Mercurio G, McNellis E R, Martin I, Hagen S, Leyssner F, Soubatch S, Meyer J, Wolf M, Tegeder P, Tautz F S and Reuter K 2010 Structure and Energetics of Azobenzene on Ag(111): Benchmarking Semiempirical Dispersion Correction Approaches *Phys. Rev. Lett.* **104** 036102
- [117] Knapas K and Ritala M 2011 In situ Reaction Mechanism Studies on Atomic Layer Deposition of Ir and IrO<sub>2</sub> from Ir(acac)<sub>3</sub> *Chem. Mater.* **23** 2766–71
- [118] Papandrew A B, Chisholm C R I, Elgammal R A, Özer M M and Zecevic S K 2011 Advanced Electrodes for Solid Acid Fuel Cells by Platinum Deposition on CsH<sub>2</sub>PO<sub>4</sub> *Chem. Mater.* **23** 1659–67
- [119] Hämäläinen J, Munnik F, Ritala M and Leskelä M 2008 Atomic Layer Deposition of Platinum Oxide and Metallic Platinum Thin Films from Pt(acac)<sub>2</sub> and Ozone *Chem. Mater.* **20** 6840–6
- [120] Hämäläinen J, Puukilainen E, Kemell M, Costelle L, Ritala M and Leskelä M 2009 Atomic Layer Deposition of Iridium Thin Films by Consecutive Oxidation and Reduction Steps *Chem. Mater.* **21** 4868–72
- [121] Wu L and Eisenbraun E 2007 Hydrogen plasma-enhanced atomic layer deposition of copper thin films *J. Vac. Sci. Technol. B* **25** 2581–5
- [122] Alnes M E, Monakhov E, Fjellvåg H and Nilsen O 2012 Atomic Layer Deposition of Copper Oxide using Copper(II) Acetylacetonate and Ozone *Chem. Vap. Depos.* **18** 173–8
- [123] Nolan M and Elliott S D 2009 Competing Mechanisms in Atomic Layer Deposition of Er<sub>2</sub>O<sub>3</sub> versus La<sub>2</sub>O<sub>3</sub> from Cyclopentadienyl Precursors *Chem. Mater.* **22** 117–29
- [124] Phung Q M, Pourtois G, Swerts J, Pierloot K and Delabie A 2015 Atomic Layer Deposition of Ruthenium on Ruthenium Surfaces: A Theoretical Study *J. Phys. Chem. C* **119** 6592–603

- [125] Kresse G and Hafner J 1994 Ab initio molecular-dynamics simulation of the liquid-metal-amorphous-semiconductor transition in germanium *Phys Rev B Condens Matter* **49** 14251–69
- [126] Li Z and Gordon R G 2006 Thin, Continuous, and Conformal Copper Films by Reduction of Atomic Layer Deposited Copper Nitride *Chem. Vap. Depos.* **12** 435–41
- [127] Chae J, Park H-S and Kang S 2002 Atomic Layer Deposition of Nickel by the Reduction of Preformed Nickel Oxide *Electrochem. Solid-State Lett.* **5** C64–6
- [128] Lee S Y, Mettlach N, Nguyen N, Sun Y M and White J M 2003 Copper oxide reduction through vacuum annealing *Appl. Surf. Sci.* **206** 102–9
- [129] Rodriguez J A, Kim J Y, Hanson J C, Pérez M and Frenkel A I 2003 Reduction of CuO in H<sub>2</sub>: In situ time-resolved XRD studies *Catal. Letters* **85** 247–54
- [130] Kim J Y, Rodriguez J A, Hanson J C, Frenkel A I and Lee P L 2003 Reduction of CuO and Cu<sub>2</sub>O with H<sub>2</sub>: H embedding and kinetic effects in the formation of suboxides *J. Am. Chem. Soc.* **125** 10684–92
- [131] Rodriguez J A, Hanson J C, Frenkel A I, Kim J Y and Pérez M 2002 Experimental and Theoretical Studies on the Reaction of H<sub>2</sub> with NiO: Role of O Vacancies and Mechanism for Oxide Reduction *J. Am. Chem. Soc.* **124** 346–54
- [132] Heyd J, Scuseria G E and Ernzerhof M 2003 Hybrid functionals based on a screened Coulomb potential *J. Chem. Phys.* **118** 8207–15
- [133] Heyd J and Scuseria G E 2004 Efficient hybrid density functional calculations in solids: Assessment of the Heyd--Scuseria--Ernzerhof screened Coulomb hybrid functional *J. Chem. Phys.* **121** 1187–92
- [134] Perdew J P, Burke K and Ernzerhof M 1997 Generalized Gradient Approximation Made Simple [Phys. Rev. Lett. 77, 3865 (1996)] *Phys. Rev. Lett.* **78** 1396
- [135] Wang L, Maxisch T and Ceder G 2006 Oxidation energies of transition metal oxides within the GGA+U framework *Phys. Rev. B* **73** 195107
- [136] Dudarev S L, Botton G A, Savrasov S Y, Humphreys C J and Sutton A P 1998 Electron-energy-loss spectra and the structural stability of nickel oxide: An LSDA+U study *Phys. Rev. B* **57** 1505–9
- [137] Nolan M and Elliott S D 2006 The p-type conduction mechanism in Cu<sub>2</sub>O: a first principles study *Phys. Chem. Chem. Phys.* **8** 5350–8
- [138] Ganduglia-Pirovano M V, Da Silva J L F and Sauer J 2009 Density-Functional Calculations of the Structure of Near-Surface Oxygen Vacancies and Electron Localization on CeO<sub>2</sub>(111) *Phys. Rev. Lett.* **102** 26101

## 0. Bibliography

---

- [139] Asbrink S and Norrby L J 1970 A refinement of the crystal structure of copper(II) oxide with a discussion of some exceptional e.s.d.'s *Acta Crystallogr. Sect. B* **26** 8–15
- [140] Marabelli F, Parravicini G B and Salghetti-Drioli F 1995 Optical gap of CuO *Phys Rev B Condens Matter* **52** 1433–6
- [141] Hu J, Li D, Lu J G and Wu R 2010 Effects on Electronic Properties of Molecule Adsorption on CuO Surfaces and Nanowires *J. Phys. Chem. C* **114** 17120–6
- [142] Yang B X, Thurston T R, Tranquada J M and Shirane G 1989 Magnetic neutron scattering study of single-crystal cupric oxide *Phys. Rev. B* **39** 4343–9
- [143] Ganduglia-Pirovano M V, Hofmann A and Sauer J 2007 Oxygen vacancies in transition metal and rare earth oxides: Current state of understanding and remaining challenges *Surf. Sci. Rep.* **62** 219–70
- [144] Morgan B and Watson G 2010 Intrinsic n-type defect formation in TiO<sub>2</sub>: a comparison of rutile and anatase from GGA+U calculations *J. Phys. Chem. C* 2321–8
- [145] Li C, Wang F, Li S F, Sun Q and Jia Y 2010 Stability and electronic properties of the O-terminated Cu<sub>2</sub>O(111) surfaces: First-principles investigation *Phys. Lett. Sect. A Gen. At. Solid State Phys.* **374** 2994–8
- [146] Kowalski P M, Meyer B and Marx D 2009 Composition, structure, and stability of the rutile TiO<sub>2</sub>(110) surface: Oxygen depletion, hydroxylation, hydrogen migration, and water adsorption *Phys. Rev. B* **79** 115410
- [147] Maimaiti Y and Elliott S D 2015 Precursor Adsorption on Copper Surfaces as the First Step during the Deposition of Copper: A Density Functional Study with van der Waals Correction *J. Phys. Chem. C* **119** 9375–85